Dpto. de Física Teórica y del Cosmos & CAFPE
Universidad de Granada

Direct Dark Matter Searches with Noble Liquid Detectors:
The ArDM Experiment

Memoria presentada por

María del Carmen Carmona Benítez.

Director:

Dr. **Antonio Bueno Villar.**

- Mayo de 2009 -

Editor: Editorial de la Universidad de Granada
Autor: María del Carmen Carmona Benítez
D.L.: GR. 2654-2009
ISBN: 978-84-692-4183-7

D. Antonio Bueno Villar, Profesor Titular de Universidad,

CERTIFICA: que la presente memoria, DIRECT DARK MATTER SEARCHES WITH NOBLE LIQUID DETECTORS: THE ARDM EXPERIMENT, ha sido realizada por Dña. María del Carmen Carmona Benítez bajo su dirección en el Dpto. de Física Teórica y del Cosmos, así como que ésta ha disfrutado de estancias en el extranjero por un periodo superior a tres meses en el CERN (Suiza).

Granada, 15 de Mayo de 2009

Fdo: Antonio Bueno Villar

Agradecimientos

Llegado el momento de concluir este trabajo, se hace difícil expresar en tan sólo unos cuantos párrafos el reconocimiento a todos aquéllos que de una u otra forma me han ayudado a recorrer este camino a lo largo de estos años, alentándome y brindándome su apoyo. No obstante, manifiesto mi agradecimiento a todas estas personas.

En primer lugar, a mi tutor, Antonio Bueno, sin cuya cordial acogida y magistral orientación esta tesis hubiese sido irrealizable. En estos años me ha demostrado ser, por encima incluso de sus grandes cualidades profesionales, una gran persona y un amigo. Le agradezco la confianza depositada en mí, el entusiasmo transmitido, todo el tiempo que me ha dedicado, su paciencia y sus aportaciones en mi formación personal y profesional.

Al departamento de Física Teórica y del Cosmos de la Universidad de Granada, por haber acogido este trabajo. A Francisco del Águila, director de este departamento, por su información, consejos y buena disposición.

A mis compañeros del grupo de investigación por todos los momentos vividos y compartidos. A Sergio Navas, por su disponibilidad, sus recomendaciones y aportaciones en las discursiones sostenidas sobre física. A Ángel Ruiz, por su colaboración en la parte de la electrónica y por las horas compartidas en el laboratorio, tanto en Granada como en el CERN. A Antonio Melgarejo, mi primer compañero de despacho y con el que he trabajado en algunas ocasiones, y a Diego García y Luis Navarro, también compañeros de encierro y de cafés, por sus palabras de aliento. A Julio Lozano, por haberme prestado su ayuda cuando la he necesitado.

A los miembros de la colaboración del experimento ArDM, con quienes he trabajado. Al profesor André Rubbia, por permitirme realizar una fructífera estancia en el CERN y al resto de miembros de su grupo que de alguna manera me han apoyado durante mi estancia allí. En especial, a Marco Laffranchi, con quién trabajé de forma más estrecha y quien me inició en el mundo del "*hardware*", y a Lilian Kaufmann y Polina Otiougova por el inestimable tiempo compartido.

A los familiares y amigos, que me animaron en estos años de trabajo.

A mis padres, por todo lo que me han dado a lo largo de mi vida, por la educación, los consejos y el cariño que de ellos siempre he recibido. A mis hermanos por su apoyo incondicional.

Y de forma especial, agradezco a Jorge de Blas, a quien dedico esta tesis, por estar siempre a mi lado, en los momentos buenos y malos que se han presentado a lo largo de la realización de este trabajo.

A todos, cercanos o lejanos, mis más sincero agradecimiento.

Contents

Introduction

At present, in round numbers, our universe consists of 5% baryons, 23% dark matter, and 72% dark energy. It is indeed embarrassing that 95% of the universe is unaccounted for: even the dark matter is of quite uncertain nature, and the dark energy is a complete mystery.

Figure 1: Composite image of the Bullet Cluster, showing the inferred dark matter distribution as blue and the measured hot gas distributions in red.

The evidence for the existence of dark matter is overwhelming, mainly due to its gravitational effects (see figure 1). Nowadays there are many experiments attempting to discover exactly what its nature is. All direct search detectors aim to observing nuclear recoils produced by dark matter particles scattering off target nuclei. There are a few different methods that can be used to detect nuclear recoils, including collecting ionisation, scintillation or thermal energy deposition data. Detectors combining at least two of these techniques have the best potential to detect the unknown particles, since they have enhanced background rejection capabilities, thus providing the best limits. The nuclear recoils that must be observed are in the range $1 - 100$ keV. Therefore, massive detectors with low energy threshold and high background discrimination capabilities are vital. In this framework, liquified noble gas detectors are promising devices for direct dark matter

searches.

The work presented in this Ph.D. Thesis discusses the potential and versatility of a massive detector using noble gases as target to make outstanding contributions in direct searches for dark matter. We will concentrate on the performance of the Argon Dark Matter (ArDM) experiment as well as the study of potential background sources.

The Thesis is organized as follows: In Chapter 1 we introduce what it is currently known about dark matter, focusing in direct search experiments. We pay particular attention to liquid argon TPCs.

In Chapter 2 we present the ArDM experiment: its principle of operation and all the components which make up the light and charge readout systems. A description of a detailed Mote Carlo simulation of the experimental setup is given. In addition, we show the good agreement of this simulation with respect to experimental measurements carried out in a first surface operation of the ArDM prototype [1].

Chapter 3 reviews the slow control system of the ArDM experiment. We describe in detail each component of the system: temperature, level and pressure gauges, their calibration and precision obtained in experimental tests.

Chapter 4 fully concentrates on the physics performance of the ArDM detector. We study the rejection capability against potential background sources, in particular the internal ^{39}Ar contamination and neutron backgrounds.

Chapter 5 concentrates on evaluating the physics potential of a different experimental setup. In this case, we explore the physics performance of a modular detector operated in conjuction with an active veto target, made of water doped with gadolinium. Special attention is given to the identification and precise measurement of the background produced by neutrons (see reference [2] for details).

The last Chapter is devoted to show that this kind of massive detector, based in liquified noble gases, has an enormous potential too in experiments aiming to discover yet unobserved reactions in neutrino physics. In particular we study the possible observation of coherent neutrino-nucleus elastic scattering at a low-energy beta beam [3]. We end up this document summarizing the main results of this Ph.D. work.

Introducción

En la actualidad, nuestro universo está constituido aproximadamente por un 5 % de bariones, un 23 % de materia oscura y un 72 % de energía oscura. Es muy embarazoso que el 95 % del universo no se conozca: de hecho la naturaleza de la materia oscura es bastante incierta, y la energía oscura es un completo misterio.

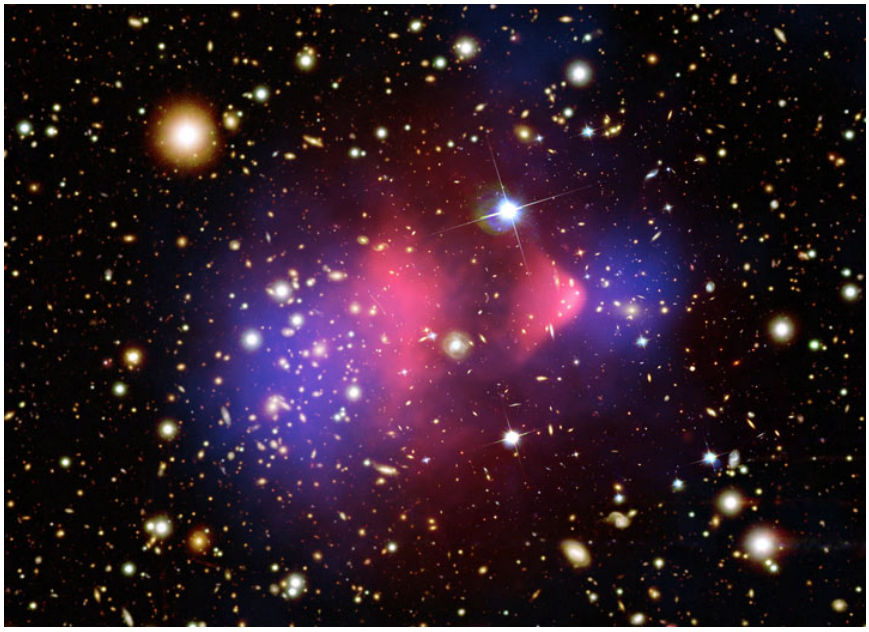

Figura 2: Imagen compuesta del cúmulo galáctico conocido como Bullet, mostrando la distribución de materia oscura inferida en azul y la distribución de gas caliente en rojo.

La evidencia de la existencia de materia oscura es abrumadora, principalmente debido a sus efectos gravitatorios (ver figura 2). Hoy en día hay muchos experimentos intentando descubrir cúal es exactamente su naturaleza. Todos los detectores para su búsqueda directa apuntan a observar retrocesos nucleares producidos por las colisiones elásticas de partículas de materia oscura con núcleos blanco de materia ordinaria. Hay distintos métodos que se pueden utilizar para detectar retrocesos nucleares. Estos incluyen: colección de ionización, centelleo o datos de deposición de energía térmica. Los detectores que combinan al menos dos de estas técnicas tienen el mejor potencial para detectar las partículas desconocidas, ya que han optimizado sus capacidades para rechazar los fondos, proporcionando por consiguiente los mejores límites. Los retrocesos nucleares

que se deben observar están en el rango de energías de $1 - 100$ keV. Por lo tanto, es vital la utilización de detectores masivos con bajos umbrales de detección de energía y gran capacidad de discriminación de fondos. En este marco, los detectores de gases nobles licuados son dispositivos prometedores para búsquedas de materia oscura.

El trabajo que se presenta en esta Tesis trata el potencial y versatilidad de detectores masivos, que utilizan gases nobles como medio sensible, para hacer contribuciones destacadas en búsquedas directas de materia oscura. Nos concentraremos en las prestaciones del experimento ArDM así como en el estudio de las posibles fuentes de fondos.

La Tesis está organizada del siguiente modo: En el Capítulo 1 presentamos lo que se conoce actualmente sobre materia oscura, centrándonos en los experimentos de búsqueda directa. Pondremos especial atención a las Cámaras de Proyección Temporal de Argón Líquido (LAr TPCs, por sus siglas en inglés).

En el Capítulo 2 presentamos el experimento ArDM: su principio de operación, y todos los componentes que conforman los sistemas de lectura de carga y luz. Se ofrece una descripción de la detallada simulación Monte Carlo del conjunto del experimento. Además, se muestra el buen acuerdo que hay entre la simulación y las medidas experimentales realizadas en la primera operación en superficie del prototipo del detector ArDM [1].

En el Capítulo 3 se revisa el sistema de control de las condiciones de operación del experimento ArDM. Describimos en detalle cada componente del sistema: sensores de temperatura, nivel y presión, su calibración y la precisión obtenida en los tests experimentales.

El Capítulo 4 se concentra completamente en las prestaciones físicas del detector ArDM. Estudiamos la capacidad de rechazo frente a posibles fuentes de fondos. En particular estudiamos la contaminación debida al isótopo intrínseco ^{39}Ar y fondos de neutrones.

El Capítulo 5 se concentra en evaluar la física que ofrece un dispositivo experimental distinto. En concreto, se exploran las prestaciones de un detector modular que funciona al mismo tiempo que un blanco que actúa como veto activo, compuesto de agua dopada con gadolinio. Prestamos especial atención a la identificación y medida precisa del fondo generado por neutrones (ver también la referencia [2] para más detalles).

El último Capítulo de esta Tesis está dedicado a mostrar que este tipo de detector masivo, basado en gases nobles licuados, tiene también un inmenso potencial en experimentos que intentan medir reacciones no detectadas hasta ahora en física de neutrinos. En particular, estudiamos la posibilidad de observar la colisión elástica coherente neutrino-nucleón con un haz proveniente de emisores beta a baja energía [3]. Este documento termina con el resumen de los resultados principales de este trabajo de doctorado.

Chapter 1

Status of Dark Matter searches

In the past decade, breakthroughs in cosmology have transformed our understanding of the universe. A wide variety of observations have unambiguously shown the existence of an unknown form of matter that has been called *dark matter*. Despite this progress, the identity of dark matter remains a mystery. Current constraints on dark matter properties show that the bulk of it cannot be any of the known particles. Its existence is at present one of the pieces of evidence that the current theory of fundamental particles and forces, summarized in the standard model (SM) of particle physics, is incomplete. Advances in our field have led to predictions of new physics beyond the standard model, and most of the proposed extensions of this model predict a particle that could be a candidate to explain the dark matter content of the universe. At the same time, because dark matter is a dominant form of matter in the universe, an understanding of its properties is essential to determine how galaxies formed and how the universe evolved. Dark matter therefore plays a central role in both particle physics and cosmology, and the discovery of its nature is among the most important goals in science today.

Experimental searches for candidates have been conducted and are ongoing. These efforts can be divided into two broad classes: "direct detection" [4], in which the dark matter particles are observed in a detector via elastic scattering off the nucleus of ordinary matter; and "indirect detection" [5], which looks for the products of dark matter annihilations. In this chapter, we focus our attention in direct searches of dark matter particles. Direct dark matter search experiments look for an excess of signals in an underground, low background environment. Very different detectors have been built for this purpose, having in common the capability to measure small energy depositions (∼1-100 keV). From all of the proposed media, liquefied noble gases are a very promising alternative, as the possibility to measure charge and light simultaneously allows an enhanced signal to background discrimination. Moreover, they have some other advantages, as the relative high temperature at which they work compared to that of bolometers, or the cost, which make feasible to go to much higher masses than for other kind of detectors.

In what follows, we will give a brief introduction of what we currently know about dark matter and describe the main characteristics of liquid noble detectors (specially liquid argon TPCs) used in direct search experiments.

1.1 Dark Matter

The current standard model of cosmology tells us that the universe consists of 5% ordinary baryonic matter, roughly 23% dark matter and about 72% dark energy, with a tiny abundance of relic

neutrinos. Thanks to its gravitational effects, the evidence for the existence of dark matter is overwhelming, and comes from a wide variety of astrophysical measurements:

1. **Cluster of galaxies**. The first evidence for the existence of dark matter in the universe was found by Zwicky in 1933. He noticed that by applying to the Coma Cluster the virial theorem, which relates the average kinetic energy of a system to its average total potential energy, the predicted mass was much bigger than the observed one.

2. **Rotational curves of galaxies**. In the 1970's Ford and Rubin first discovered that rotation curves of galaxies are flat. The centripetal velocity of objects (stars or gas) orbiting the centers of galaxies, rather than decreasing as a function of the distance from the galactic centers, remain constant out to very large radii. Indeed, more than 95% of the mass of the galaxies consists of dark matter. This is illustrated in figure 1.1, where the velocity profile of galaxy M33 is displayed as a function of radial distance from galactic center. The baryonic matter which accounts for the gas and disk cannot alone explain the galactic rotation curve. However, adding a dark matter halo allows a good fit to data.

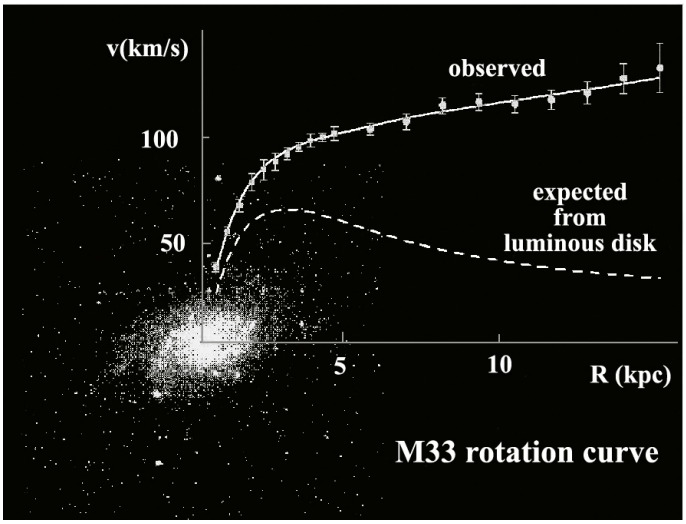

Figure 1.1: Rotation curve of the galaxy M33. The total rotation curve correspond to the upper line with measured values. The expected effect of the luminous disk, whose velocity decreases as $1/\sqrt{R}$, is displayed separately to show that it does not explain by itself the galactic rotation curve.

3. **Gravitational lensing**. Einstein's theory of general relativity predicts that mass bends, or "lenses" light. This effect can be used to gravitationally ascertain the existence of mass even when it emits no light. If a massive body is between an observer and the object he is observing, it will bend the light producing multiple images of the observed body. Through the geometrical distortion it is possible to obtain the mass distribution of the massive object. The importance of this measurement relies on the fact that it is independent of the dynamics and predicts similar mass distributions. There is another technique based on the same effect, known as weak lensing, that instead of single observations considers vast galactic surveys to look for small distortions through statistical analyses.

4. **Hot gas in clusters**. Another piece of gravitational evidence for dark matter is the hot gas in clusters, for example in the Coma Cluster. The X-ray image of this cluster indicates the presence of hot gas. Its existence can only be explained by a large dark matter component that provides the potential well to hold on the gas.

5. **WMAP Data**. Measurements of the microwave background radiation performed by the WMAP satellite combined with the distance measurements from the Type Ia supernovae (SN) and the Baryon Acoustic Oscillation (BAO) in the distribution of galaxies [6] show that only a small fraction of the matter content of the universe is of baryonic origin ($\Omega_B = 0.0456 \pm 0.0015$), while the rest is made of a totally unknown new form of matter ($\Omega_{DM} = 0.228 \pm 0.013$). The rest of the energy content of the universe is accounted for advocating a very smooth form of energy called dark energy ($\Omega_\Lambda = 0.726 \pm 0.015$)[1].

6. **Bullet Cluster**. Optical and X-ray images of the bullet cluster (1E0657-558) [7, 8], obtained by the Chandra telescope. In this cluster the collision of two galaxies, that happened 150 million years ago, can be observed. By means of gravitational lensing, a map of the matter in the collision region can be obtained, and it is possible to see clearly that while the hot gases that interacted during the collision remained close to the center, there is a massive component that did not interact and is away from the center.

There are two obvious possible explanations to all these facts: either the measured amount of mass is much bigger than the observable one, or the dynamics used to compute masses is wrong. Since the decade of 1980 a new kind of theories called MOND (Modified Newtonian Dynamics) have attempted to explain all the observed phenomena through a modification of Newton's second law of dynamics for small accelerations [9]. However, up to this moment none of these theories have succeeded to explain the whole set of phenomena.

So far dark matter has only been observed through its gravitational effects. Hence we know nothing about its nature and fundamental properties. A convincing case seems to exist for non-baryonic dark matter. Elementary particles, often arising from yet undiscovered but well motivated physics, dominate the field [10]. The dark matter density in the neighborhood of our solar system is expected to be $\rho_{DM} \sim 0.3$ GeV·cm^{-3}, although this varies in some halo models. We will discuss now some of the candidate particles.

Standard model neutrinos are known to be massive. A lower limit on their mass square difference stems from the observation of neutrino oscillations in atmospheric neutrino data [11]:

$$\Delta m^2_{23} \sim 3 \times 10^{-3}\, eV^2 \tag{1.1}$$

which when combined with solar neutrino oscillation data implies that the most massive neutrino must have a mass ≥ 0.05 eV. The contribution of neutrinos to the universe follows the relation:

$$\Omega_\nu h^2 = \sum_{i=1}^{3} \frac{g_i m_i}{90\, eV} \tag{1.2}$$

where $g_i = 1$ for Majorana neutrinos and $g_i = 2$ for Dirac neutrinos, which suggests a minimum contribution to the universe composition (for a Majorana neutrino) of $\Omega^2_{\nu h} \geq 0.0006$. So standard model neutrinos are dark matter. However, they are hot. An excess amount of relativistic particles during the epoch of galaxy formation would wash out small scale structure, preventing agreement with the matter density distribution observed today. A combination of galaxy clustering

[1] $\Omega_x = \rho_x/\rho_c$, where ρ_x is the density of x and ρ_c is the critical density for a flat universe.

measurements, CMB and observations of Lyman-α forest gives an upper limit on light neutrino combination of [12]:

$$\Omega_\nu h^2 < 0.0076 \,(\text{at } 95\%\text{C.L.}) \tag{1.3}$$

This limit applies to all forms of hot dark matter. Our main interest therefore focuses on cold dark matter candidates only, since they must form the dominant matter component.

The nature of these particles is not precisely known. However, candidates for cold dark matter must satisfy the following conditions:

- Interact very weakly, or not at all, with electromagnetic radiation (so they are called *dark*).
- Have a cosmologically interesting (preferably dominant) relic density.
- Be stable on time scales comparable with the age of the universe (otherwise they would have decayed).

A strongly favored candidate for cold dark matter is the WIMP (Weak Interacting Massive Particle), with a mass m_χ roughly between 10 GeV and a few TeV, and with interaction cross section of the order of the weak scale. Their present relic density can be calculated reliably if the WIMPs were in thermal equilibrium with the other standard model particles in the early stages (< 1 ns) following the Big Bang. In this case their density would become exponentially (Boltzmann) suppressed at $T < m_\chi$. When the expansion rate of the universe, H, exceeds the particle annihilation/creation rate, the WIMPs drop out of thermal equilibrium, and the number density (for a comoving volume) becomes frozen. Their present relic density is then approximately given by [4]:

$$\Omega_\chi h^2 \simeq \frac{T_0^3}{M_{Pl}^3 \langle \sigma_a v \rangle} \simeq \frac{0.1\,\text{pb} \cdot c}{\langle \sigma_a v \rangle} \tag{1.4}$$

Here T_0 is the current CMB temperature, M_{Pl} is the Planck mass, c is the speed of light, σ_a is the total annihilation cross section of a pair of WIMPs into SM particles, v is the relative velocity between the two WIMPs in their cms system, and $\langle ... \rangle$ denotes thermal averaging. Freeze out happens at temperature $T \simeq m_\chi/20$ almost independent of the properties of the WIMP. This means that WIMPs are already non relativistic when they decouple. A cosmologically interesting density arises from an annihilation cross section of the order of the electroweak scale interaction. This last coincidence, which is not tuned, but comes directly from reliable calculations, represents one of the main motivations for believing that WIMPs could provide the dominant contribution to the matter in the universe. It is also important to note that smaller annihilation cross sections correspond to larger relic densities. WIMPs with stronger interactions remain in equilibrium for longer and hence decouple when the universe is colder, and so they are suppressed by a smaller Boltzmann factor.

1.2 WIMP direct detection rate

As already mentioned, we focus our attention in direct searches of dark matter candidates. Direct detection of WIMPs will require large detector mass, low energy thresholds, efficient nuclear recoil detection and long counting times. All the experiments for direct searches of dark matter are based on the detection of nuclear recoils arising from collisions between WIMPs and target nuclei (for example, argon in the case of the ArDM experiment, see chapter 2). The differential spectrum of such recoils is expected to be featureless and smoothly decreasing, with the typical form:

$$\frac{dR}{dE_R} = \frac{R_0}{E_0 r} e^{-E_R/E_0 r} \tag{1.5}$$

where E_R is the recoil energy, E_0 is the most probable incident kinetic energy of a dark matter particle of mass M_D, r is a kinematic factor $r = 4M_D M_T/(M_D + M_T)^2$, for a target nuclei of mass M_T, R is the event rate per unit of mass and R_0 is the total event rate. Since galactic velocities are of the order 10^{-3}c, values of M_D in the 10−1000 GeV range would give typical recoil energies in the range 1−100 keV.

If we denote the generic low energy elastic cross-section as [13]:

$$\sigma_0 \propto \left(\frac{g_D^2 g_N^2}{M_E^4}\right)\mu^2 \tag{1.6}$$

where g_D, g_N are the dimensionless coupling strengths to WIMP and nucleus, respectively, of a heavy exchanged particle of mass M_E, and $\mu^2 = M_D M_T r/4$, one can write:

$$\frac{R_0}{r} \equiv 126\left(\frac{\sigma_0}{1\text{ pb}}\right)\left(\frac{1\text{ GeV c}^{-2}}{\mu}\right)^2\left(\frac{\rho_D}{0.4\text{ GeV c}^{-2}\text{ cm}^{-3}}\right)\left(\frac{v_0}{230\text{ km s}^{-1}}\right)\text{events/kg/day} \propto \left(\frac{g_D^2 g_N^2}{M_E^4}\right)\mu^2 \tag{1.7}$$

which allows to relate the observed rate with the WIMP mass and the interaction cross-section.

The aim for all the experiments is to progressively reduce or reject background events to allow a spectrum of rare nuclear recoil events to be observed. Hence, underground operation is required to eliminate nuclear recoils from neutrons produced by cosmic ray muons.

When an experiment has set an upper limit to the differential rate at any particular value of E_R, the right hand of equation (1.5) allows a corresponding limit on R_0, the dark matter signal, to be calculated for each assumed value of particle mass. Since the galactic dark matter density and flux are approximately known, the limit on R_0 can be converted to a limit on the particle interaction cross section.

In practice, equation 1.5 is considerably more complicated owing to the following corrections:

1. The detector is located on the Earth in orbit around the Sun, with the solar system moving through the galaxy.

2. The detection efficiency for nuclear recoils will in general be different from that for the background electron recoils. Thus the "true recoil energy" will differ from the observed one by that relative factor.

3. The target may consist of more than one element, with separate limits resulting from each.

4. There are instrumental resolution and threshold effects, for example when photomultipliers are used to observe events yielding small numbers of photoelectrons.

5. The limits set will, in general, be different for spin-dependent and spin-independent interactions, the latter being, in addition, coherently enhanced in amplitude at low energies by the number of interaction target nuclei.

6. There is a form factor correction < 1 which is due to the finite size of the nucleus and dependent principally on nuclear radius and recoil energy. This also differs for spin-dependent and spin-independent interactions.

To take into account all these effects, equation 1.5 can be rewritten as:

$$\left.\frac{dR}{dE_R}\right|_{observed} = R_0 \cdot S(E_R) \cdot F^2(E_R) \cdot I \tag{1.8}$$

where the main ingredients have been factorized in order to decouple the $S(E_R)$ term, counting for the kinematic of the process and the detector response, from the other factors involving the physics of the interactions. Equation 1.8 has a crucial role in the direct detection experiments since it connects the experimental data (represented by the left-hand side) with the theoretically predicted spectrum, opportunely corrected to counts for the detector properties. In more details, the right-hand side factors are:

- **The spectral function** $S(E_R)$. This term contains the basic behaviour of the expected recoil spectrum modified to count for the previous corrections, from 1 to 4, enumerated above. It depends on the properties of the halo model considered for the dark matter. For practical purposes, it can be written as [13]:

$$S(E_R) = \frac{k_0}{k_1}\frac{1}{E_0 r}\left(c_1 e^{-c_2 E_R/E_0 r} - e^{-v_{esc}^2/V_0^2}\right)$$

  where k_0, k_1 are constants, v_{esc} is the local galactic escape velocity, $v_0 = 230$ km s^{-1} and c_1, c_2 are fitting constants, of order unity. There is, however, one important fact not included in this equation. The Earth velocity changes as $v_E \approx 244 + 15\sin(2\pi y)$ km s^{-1}, where y is the elapsed time from (approximately) March 2nd in years. This modulation of $\sim 6\%$ in velocity gives rise to a modulation of $\sim 3\%$ in rate. So an experiment measuring at different seasons should measure different rates. Based on this effect the experiment DAMA claimed the observation of dark matter in their setup [14]. Together with the new LIBRA data the evidence of dark matter particles in the galactic halo amounts to a cumulative confident level of 8.2 σ. However, other direct-search experiments, probing similar regions of the parameter space, have found negative results [15, 16, 17, 18, 19].

- R_0 **is the total recoil rate for unit of mass** supposing a stationary detector with respect to the galactic centre and assuming an infinite escaping velocity. It strongly depends on the WIMP-nucleus cross section and on the WIMP distribution.

- **The nuclear form factor** $F^2(E_R)$ counting for the finite size of the nucleus. When the momentum transfer q $= \sqrt{2M_T E_R}$ is such that the wavelength h/q is no longer comparable to the nuclear radius, the effective cross section begins to fall with increasing q, even for the spin dependent case, which effectively involves only a single nucleon. This is usually represented by a form factor F, which is a function of q and the "nuclear radius" $r_n = a_n A^{1/3} + b_n$. For most of the cases, it is sufficient to use the approximation $F^2 = e^{-\alpha(qr_n)^2}$, with $\alpha = 1/3$. We note that this quantity is 1 for the zero momentum transfer case.

- **The interaction function** I, used to differ the spin-independent from the spin-dependent interactions. For interactions independent on spin and the same for neutrons and protons, there will be A scattering amplitudes, that for low momentum transfer would add coherently. The rate would be given by that of 1 nucleon times the coherent interaction factor $I_C = A^2$. For the case of spin-dependent interactions, the amplitude changes sign with spin direction, so only unpaired nucleons contribute. Thus only nucleons with an odd number of protons and/or neutrons can feel this kind of interaction. In this case the interaction factor is given by $I_s = C^2\lambda^2 J(J+1)$, where C is a factor related to the quark spin content of the nucleon and λ is related with the spin and angular momentum of the unpaired nucleon. More complicated forms of these factors can be found in different reports [20]. It is important to note that in order to be comparable, results from different experiments must be expressed in terms of nucleon cross section.

1.3 Liquid noble gases as detector media for dark matter searches

Dark matter searches have been one of the fields in experimental particle physics in which more effort has been put in the last years. Very different kinds of detectors have been proposed, having in common the possibility to detect events in a range of energy from ∼100 keV down to less than 1 keV. The proposed WIMP detectors use a variety of techniques to discriminate signal from background. The three most common experimental techniques that have been exploited for detection of this energy and background suppression are ionization, scintillation and phonon emission. Table 1.1 shows some of the different techniques and target materials used, together with some of the experiments that have used them.

Type	Discrimination technique	Target Material	Experiments
Solid Scintillator	pulse shape discrimination	NaI, CaF_2	LIBRA/DAMA, ANAIS, NaIAD, NaI32
Cryogenic	phonon/charge/light	Ge, Al_2O_3	CDMS, EDELWEISS, CRESST, ROSEBUD, IGEX-DM
Liquid noble gas	light, charge, pulse shape discrimination	LAr, LXe, LNe	ArDM, WARP, XENON, ZEPLIN, CLEAN
Bubble Chamber	super heated bubbles, droplets	CF_3I, C_4F_{10}	COUPP, PICASSO
Gas detector	ionization track resolved	CS_2	DRIFT

Table 1.1: Most common experimental techniques used for dark matter searches [21].

Among all these experimental techniques, liquid noble gases seem to be one of the most promising ones. Table 1.2 shows the most important properties of liquid noble gases. Between their relevant advantages, we can point out [22]:

- These liquids are dense and homogeneous. This allows to construct large detector masses. This is crucial to explore lower cross section values. For example, we note that $\sigma \sim 10^{-46}\text{cm}^2$ produces event rates of the order of 1 event/100kg/year.
- Ionization produces very good resolution in the position of events when the detector is operated as a TPC (Time Projection Chamber), which allows the possibility of fiducial volume cuts.
- Liquefied noble gases do not attach electrons, and electron mobilities are high for the heavier noble gases, which allows long drift distances (>1m), due to, as well, their easy purification.
- Noble gases are inert, not flammable, and very good dielectrics.
- They are bright scintillators, with light yields comparable to that of NaI (∼40 photons/keV).
- Discrimination between nuclear and electron recoils are readily achieved thanks to pulse shape discrimination (not for xenon) and differences in the ionization to scintillation ratio.

The choice of natural argon for a ton-scale target instead of other noble gases, as xenon, which is the target for several running experiments, can be motivated by the following arguments:

	Z(A)	Boiling Point at 1 atm (K)	Liquid density at $T_b(g/cc)$	Ionization (e^-/keV)	Scintillation (photons/keV)	Scintillation wavelength(nm)	Triplet Molecule lifetime (μs)
He	2(4)	4.2	0.13	39	22	80	13×10^6
Ne	10(20)	27.1	1.21	46	30	78	15
Ar	18(40)	87.3	1.40	42	40	128	1.6
Kr	36(84)	119.8	2.41	49	25	150	0.09
Xe	54(131)	165.0	3.06	64	46	175	0.03

Table 1.2: Liquid noble gases properties [23].

- The detection energy threshold depends on the achievable performance of the light and ionization detection systems. The event rate in argon is less sensitive to the threshold on the recoil energy than for xenon because of the form factors. For a threshold of $\simeq 30\,\mathrm{keVr}^2$, the rates per mass on xenon and argon are similar (see figure 1.2). With such a threshold, a WIMP-nucleon cross-section of 10^{-44} cm^2 yields about one event per day per tonne.

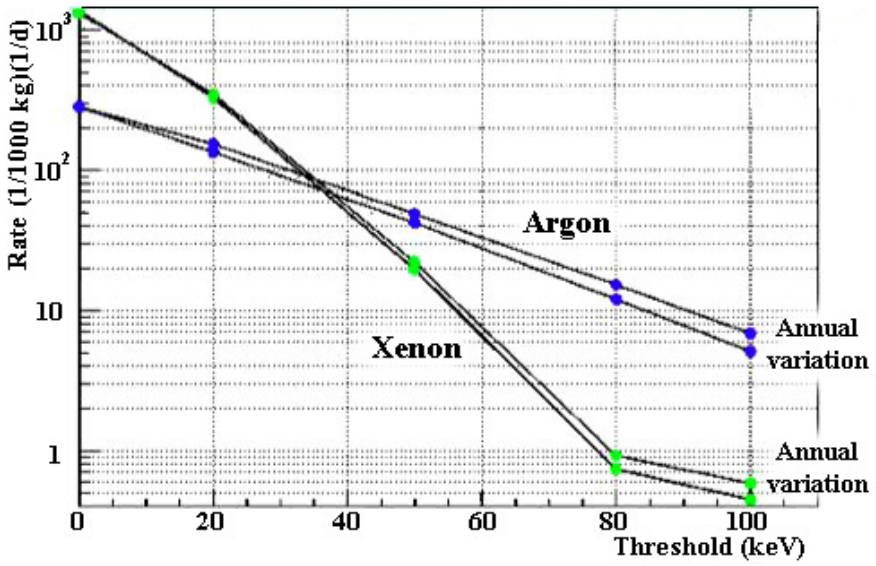

Figure 1.2: Event rate per day per tonne in argon and xenon targets. They have been computed for a WIMP mass of 100 GeV and a cross section of 10^{-6} pb. Annual variations for both targets are visible as well.

- The decay time of the slow component of the scintillation light is 1.6 μs in clean liquid argon (LAr), which is much longer that that of the prompt emission (∼few ns), allowing the use of

[2]keVr means keV of true recoil energy of the nucleus

pulse shape discrimination, while in liquid xenon both times are similar (of the order of few to tens of ns) and this technique does not provide a good rejection power.

- Argon is much cheaper than other noble gases, and there is a sizable experience in the handling of massive LAr detectors (see for example the ICARUS program [24]). A ton-scale argon detector is readily conceivable, safe and economically affordable.

- The scientific relevance of obtaining data on argon and xenon is given by the fact that recoil spectra in xenon and argon are different due to kinematics, providing an important cross check in the case of a positive signal.

Hence, liquefied noble gases and explicitly liquid argon, can meet the requirements of a dark matter search experiment providing both scalability and an efficient background rejection power.

1.4 The liquid argon TPC

Although nowadays there are experiments that still work with bubble chambers, their use has been superseded by electronic detectors in recent times. The attempt to merge the superb imaging capabilities of traditional bubble chambers and the advantages of electronic read-out in a single detector led C. Rubbia to propose the LAr time projection chamber (TPC) in 1977 [25]. The detector is essentially a cryostat filled with a liquefied noble gas with a high electric field. The principle of a LAr TPC is simple: a charged particle traversing a liquid argon volume will generate free electrons (e^-), argon ions (Ar^+) and excited atoms (Ar^*). If an electric field is applied the electrons will drift towards the lowest potential where they can be read by an appropriate device.

This is technically easy due to the high breakdown voltage of liquid argon (see table 1.3), which allows to set high voltages with electric fields typically of the order of ∼kV/cm. One can set as well arrays of tight electrodes, which make electric fields uniform. In this case the electrons will drift towards the anode with a drift velocity that will depend on the electric field and in a smaller grade on the liquid argon temperature [26, 27]. Hence, this technique provides three-dimensional imaging, as the coordinate parallel to the electric field can be known from the time that electrons take to drift. And, since the ionization charge is proportional to the energy deposition, also acts as a calorimeter of very fine granularity and high accuracy. Thus, this device is ideal to study particle interactions and does not present the problems of traditional bubble chambers, since the electronic read-out allows the self-triggering and automatic processing and analysis of the events.

Electrons can, on the other hand, recombine with their parents nuclei before they can get apart due to the action of the external electric field. This will produce excited argon atoms which will add up to those produced by the parent ionizing particle. This excited atoms will, in general, decay to photons in the energetic range of the vacuum ultraviolet, with a wavelength of 128 nm. This scintillation light provides an extra information which, together with charge, allows for particle identification at low energies. Thus, liquid argon can be used to measure low energy events, as in dark matter searches, with good positioning, calorimetric reconstruction and excellent background rejection capabilities.

1.4.1 LAr as target medium for a detector

Detectors using liquids instead of gases as target medium present a big technical issue: purity. The presence of small quantities (∼1 ppm[3]) of electronegative impurities such as O_2 can drastically

[3] 1 ppm = 1 part per million

decrease the detected signal amplitude. This reduces the choice of media to a few hydrocarbons and noble elements.

Among all the candidates, liquid argon presents some very interesting characteristics, which made it one of the most extended target medium for ionization detectors. Table 1.3 shows a summary of the main chemical and physical properties of liquid argon. The high density and low diffusion permit to have an efficient target for weakly interacting particles in a relatively small volume and a high precision in the determination of positions, which makes liquid argon a great target for the potential discovery of rare phenomena.

Atomic number	18
Concentration in air	0.934%
Naturally occurring isotopes	$^{36}Ar = 0.3365(30)$ % stable $^{38}Ar = 0.0632(5)$ % stable $^{40}Ar = 99.6006(30)$ % stable
Melting point (101325 Pa)	83.8058 K(−189.3℃)
Boiling point (101325 Pa)	87.293 K(−185.8℃)
Density at boiling point (101325 Pa)	1.396 kg/ℓ liquid 5.79 g/ℓ gas
Liquid heat capacity at boiling point (101325 Pa)	1.078 kJ/kg/K liquid
Latent energy of fusion at boiling point (101325 Pa)	161.0 kJ/kg liquid
dE/dx_{min} for a mip	2.12 MeV/cm
Critical energy (electrons)	31.7 MeV
Mean excitation potential	210 eV
Energy to produce an electron-ion pair	23.6 eV
Radiation length X_0	14.0 cm
Molière radius	9.28 cm
Nuclear interaction length	84.0 cm
Maximal breakdown strength (depending on purity level)	$1.1 - 1.4\,MV$/cm
e^- Diffusion coefficient (89 K)	4.8 cm^2/s
Recombination factor for mips (μ)	0.6 at 0.5 kV/cm

Table 1.3: Physical and chemical properties of argon.

Thanks to its properties, LAr is a good medium to detect rare events. It has a radiation length of 14 cm and a nuclear interaction length of 83.6 cm, giving good electromagnetic and hadronic calorimetric capabilities (LAr calorimeters are widely used in particle physics [28]). In addition, liquid argon acts as a great scintillator, with light yields comparable to those of crystals like NaI.

The above arguments, together with the low cost compared to xenon, for instance, makes LAr a great choice as target for the search of rare phenomena and neutrino physics.

Chapter 2

The ArDM experiment: Detector description and first experimental tests

In this chapter we describe the ArDM (Argon Dark Matter) experiment. It is a one tonne LAr detector conceived to measure WIMP elastic scattering off argon nuclei by the observation of free electrons from ionization and photons from scintillation. Those are produced by the recoiling nucleus interacting with neighbouring atoms. The ionization and scintillation signals can be measured with dedicated readout techniques, which constitute a fundamental part of the detector [29].

We have developed a detailed Monte Carlo simulation of the experimental setup. This simulation is key in order to study the light collection and the background rejection power. Thanks to this full simulation we could optimize several components that entered in the final design of the ArDM prototype.

2.1 The ArDM detection principle

We propose to build, commission and operate one tonne liquid argon detector as a tool to perform a direct search for dark matter [30]. Table 2.1 summarizes the main parameters of our detector. It is a double phase (gas-liquid) detector (see figure 2.1). Particle interactions in liquified noble gases produce charge by means of *ionization* of the atoms of the medium (42 electrons/keV) and *light* (40 photons/keV), by the de-excitation of the formed dimers [31]. Charge offers information on the energy deposited by the particle, its position and in the case of long tracks, it provides a useful variable for particle identification. While, light information is related to the determination of the primary interaction time of the particle (the so called t_0), due to its almost immediate transmission speed. Therefore, we have to detect both of them, ionization electrons and scintillation light.

Ionization electrons are drifted, by means of an intense electric field, towards the liquid surface where they are extracted. The HV system must be able to produce a huge electric field (a total of 500 kV for a field of 4 kV/cm). The extracted charge is amplified and readout with a Large Electron Multiplier (LEM) device. Among the charge amplification devices, a LEM seems to be one of the most appealing alternatives nowadays. It consists of a printed board with metallation in both sides and equally spaced holes. If a sufficient potential difference is applied, the electrons are drawn into the holes, where the high electric field induces an avalanche multiplication. Our

tests in the laboratory have shown that it is feasible to obtain amplification factors of 10^4 at LAr temperatures by using a two stage LEM [32]. This opens up the possibility to detect the ionization signals even in the presence of highly quenched nuclear recoils, like in the case of a WIMP interaction. Besides, LEM is segmented and will provide X and Y coordinates of the event, while the drift time will provide the third spatial coordinate. Thanks to this segmentation, an image of the event will be obtained.

The **scintillation light** is readout by PMTs located at the bottom of the detector, behind a transparent cathode. This light has a wavelength of 128 nm and therefore must be shifted to the visible in order to be detected by our PMTs. To this purpose the inner detector is covered by sheets of diffusive reflector (PTFE fabric $Tetratex^{TM}$, TTX) plus a wavelength shifter (Tetraphenilbutadiene, TPB) deposited on it [29]. TPB will be deposited on PMT windows as well in order to collect the non-negligible percentage of direct light.

Next section offers a detailed description of the simulation done in order to define all the elements that form the internal detector. A through description of the work done by the author with the slow control system is given in chapter 3.

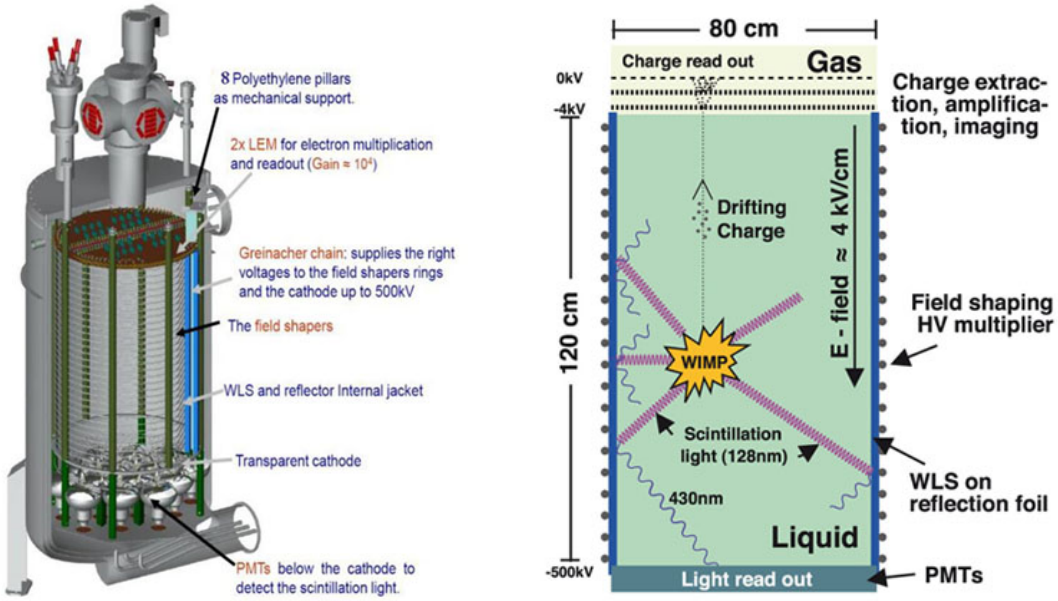

Figure 2.1: The ArDM detection principle. Charge and light produced in interactions are readout with a LEM and 14 PMTs. An electric field, uniformized by field shaping rings, is used to drift the charge up to the LEM. The drift length is 120 cm.

2.2 Detector performance and Monte Carlo

We have developed a detailed GEANT4-based [33] Monte Carlo simulation of the detector. We describe the main elements of it (cryostat, high voltage system, charge readout and light detection). In our discussion, we pay special attention to the issue of light collection.

Argon mass	850 kg
Maximum drift length	120 cm
Drift field	4 kV/cm
HV system	Greinacher/Cockroft-Walton circuit
Charge readout system	Large Electron Multiplier (LEM)
Single electron gain	$10^3 - 10^4$
Light readout system	14 hemispherical 8" PMTs
Light collection efficiency	3% of total generated γs converted in photoelectrons

Table 2.1: Main parameters of the ArDM detector.

2.2.1 ArDM cryostat

The detector is contained in a cylindrical vessel where the liquid and the vapour of the argon are in equilibrium. The inner container is a stainless steel vessel (1892 mm height, 1000 mm diameter and 12 mm thickness), which is held within a concentric outer cylinder of diameter 1110 mm and thickness 10 mm. Between both chambers there are other vessels. From the inside to the outside, we have an outer argon layer (5 mm thick), a dimple jacket of LN_2 (3 mm), an inner vacuum layer (10 mm), another cilindrical middle stainless steel vessel (6 mm) and an outer vacuum layer (25 mm) (see figure 2.2). The access to each element is provided through tubes in the top flange which connect to the LAr purification and recirculation system. Both of them are a must since LAr must be ultra-pure in order to make long electron drift paths possible [22, 24].

Fastened to the top flange, we have mounted eight polyethylene pillars (1452 mm height and 40 mm diameter) (see figure 2.3). We use them as a mechanical support for other detector components, as for example the high voltage system. They span all the length from the top flange to the cathode position. The distance from the detector centre to the pillars is 410 mm. Each of them is placed every 45 degrees. They are built out of polyethylene, since this material shows a good behaviour under LAr temperature (87 K).

We have properly implemented in the Monte Carlo the dimensions of all the vessels and the materials they are made out, including their optical properties. Thus, the eight polyethylene pillars have been simulated in their corresponding positions (see figure 2.4).

2.2.2 High voltage system

Inside the active volume there is a huge electric field (4 kV/cm). This helps reducing the recombination of the ionization electrons, even in the case of highly quenched slow nuclear recoils. To produce such a field, we use the high voltage system discussed in the next paragraphs.

At the bottom of the drift region, a light transparent **cathode** is set at high voltage (-500 kV). It consists of 78 stainless steel cylindrical wires (0.5 mm diameter), making a 20 mm x 20 mm mesh which has about 786 mm of diameter (see figure 2.5). This cathode has a light transparency of about 90% and is held by two stainless steel rings, which are fastened to the pillars.

Above the cathode, a serie of electrodes have been installed and biased along the full drift path to keep the field uniform at a level of few %. There are 30 rings in total. These **field shaping rings** are stainless steel cylinders (6 mm diameter and 1 mm thick). The distance from the detector centre is about 400 mm and the separation between two consecutive rings is 40 mm (see figure 2.3).

To supply the needed voltage (up to 500 kV), we have used a cascade of rectifier cells (Greinacher or Cockroft-Walton circuit). It takes as input an alternate voltage of amplitude V_0 and gives an

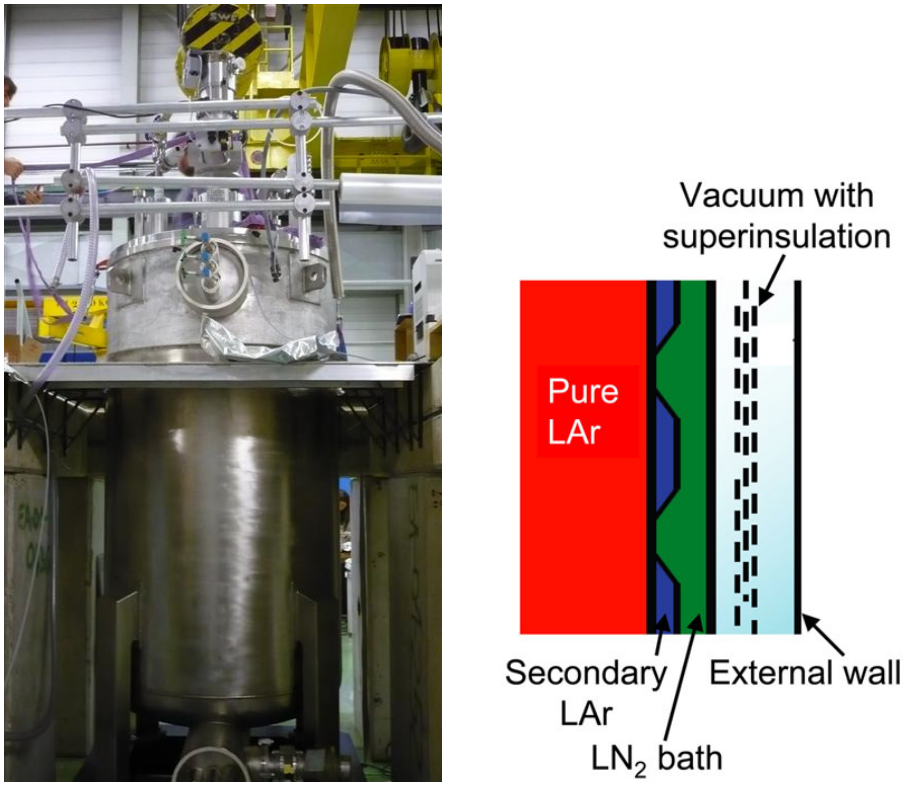

Figure 2.2: Left: ArDM vessel. The empty flange on top connects the vessel with the purification and recirculation system. Right: Cryostat layout. Cut view of the dewar wall.

output continuous, with a value $2 \cdot V_0 \cdot N$, where N is the number of stages. The whole circuit is immersed in LAr, taking advantage of its great insulation capability.

The **Greinacher chain** is made of 210 stages with 2.5 kV/stage. Each stage has four polypropylene capacitors of 82 nF. It has about 1200 mm high and is supported by a polyethylene piece, fastened to the top flange of the dewar (see figure 2.3). The 210 stage circuit has been fully assembled and successfully tested in liquid Nitrogen (see figure 2.6). In addittion, it has a stable operation in air at 120 kV.

All the components of the high voltage system have been introduced in our Monte Carlo: the cathode with the two holding rings, the 30 field shaping rings and the Greinacher chain. In particular, we have carefully implemented the dimensions of the cathode mesh and the shape of the 30 rings, since they are not exactly a complete circle (see figure 2.4).

2.2.3 Charge readout system

One of the main problems the charge detection system must cope with is the relatively small amplitude of the signals. Typically, 1 mm of a minimum ionizing track delivers less than 10^4 electrons in LAr. The signal is even smaller at lower electric fields, due to the effects of the charge attenuation and electron-ion recombination. The imaging of ionizing events requires, therefore, the use of charge amplification devices. As already mentioned, a **large electron multiplier** (LEM)

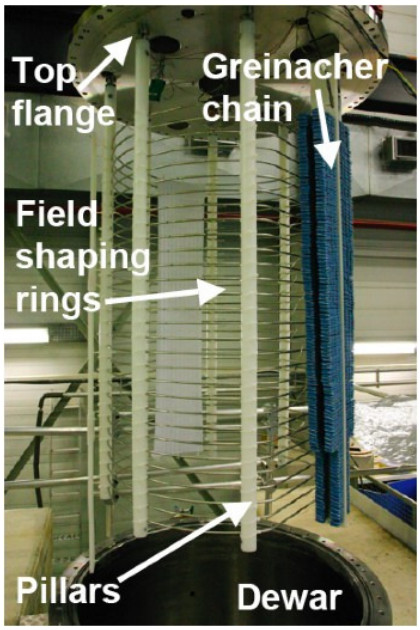

Figure 2.3: Some components of the inner detector. Field shaping rings, greinacher chain and pillars fastened to the top flange are visibles.

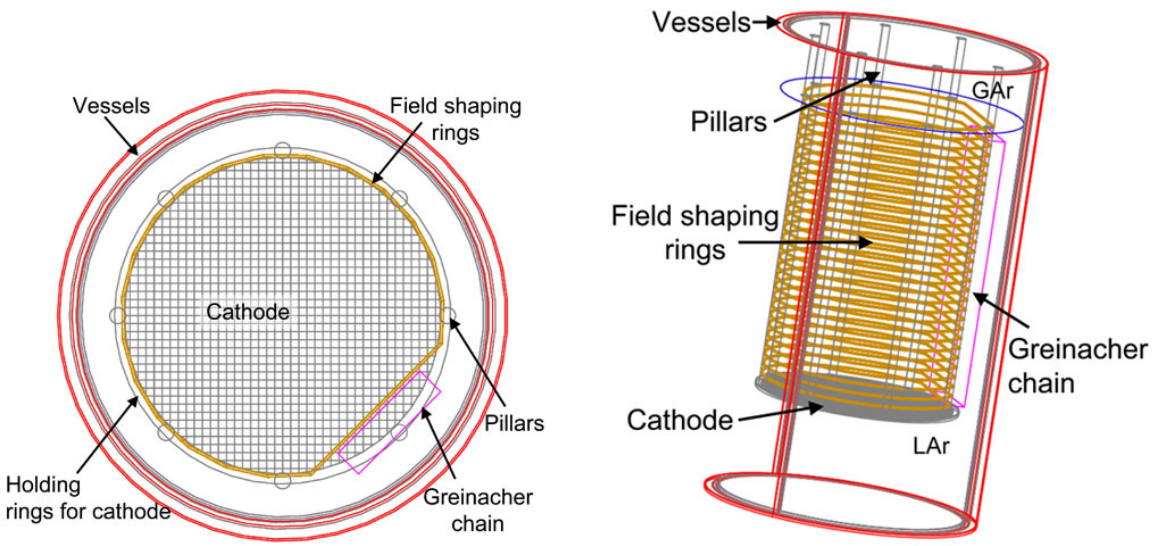

Figure 2.4: Top and lateral views of the simulated detector in GEANT4. Field shaping rings, greinacher chain, cathode and pillars are visible.

is a good device for this purpose.

Figure 2.5: The ArDM detector cathode.

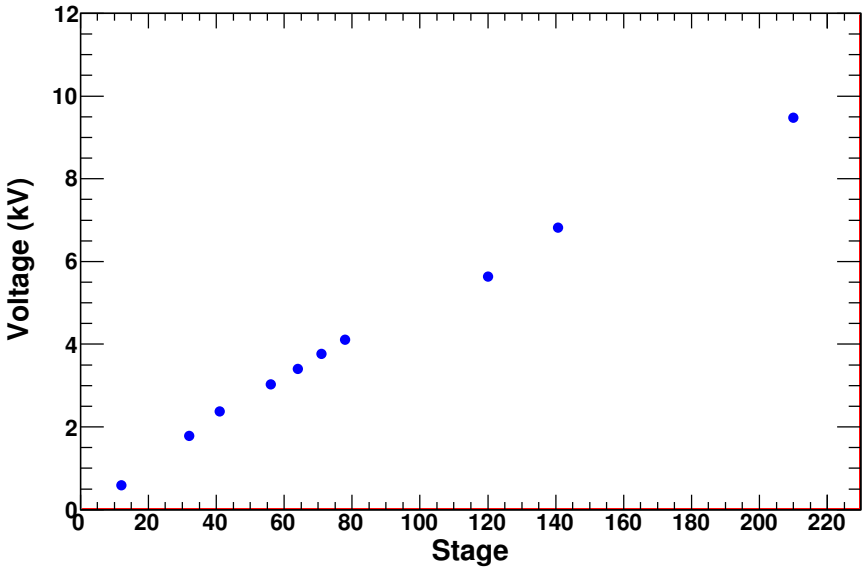

Figure 2.6: Results of the measured voltage in LN_2 for the Greinacher chain.

The ionization electrons are drifted to the liquid-vapour interface and are extracted into the gas phase. In the vapour a LEM is installed, at 5 mm above the liquid level, to provide electron amplification by means of a high field generated in small (cylindrical shaped) holes (see figure 2.7). It is a two stage LEM with 3 mm of separation between the stages. The LEM consists of two 1.6 mm thick plates of insulating material, which are covered by a copper layer on top and bottom, and a readout anode. Holes of diameter 500 μm are homogeneously distributed on the LEM, at a distance of 800 μm among them. By placing an electric field between both sides of the plate it is possible to generate an avalanche of electrons and lastly to obtain charge amplification factors of $10^3 - 10^4$, using the two stages. The avalanche spreads into several holes at second stage so higher gain can be reached w.r.t. the one stage configuration, with good stability [32]. The general technique of electron multiplication via avalanches in small holes is attractive because (1) the required electric field can be naturally attained inside the holes and (2) the finite size of the holes effectively ensures a confinement of the electron avalanche, thereby reducing secondary effects in a medium whithout quencher.

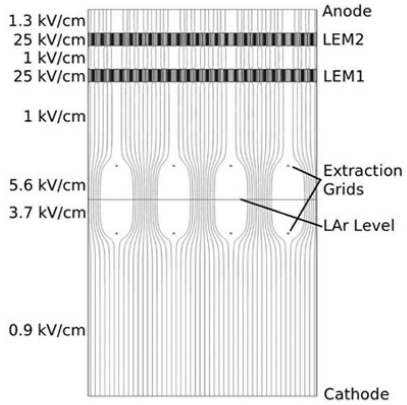

Figure 2.7: Electric field lines in the double phase operation for the LEM prototype.

In addition, LEM charge readout system is segmented. This favours the event location. The electron signal is readout via two orthogonal coordinates, one using the induced signal on the segmented upper electrode of the LEM itself (see figure 2.8) and the other by collecting the electrons on a segmented anode. We have used a small LEM prototype to test the right operation of this kind of charge readout system. Figure 2.9 shows the setup of the LEM-TPC prototype. In the LEM prototype both readout planes (second LEM stage and anode) are segmented with 6 mm wide strips, for a total of 32 readout channels in a $\sim 10 \times 10$ cm^2 active area. An example of cosmic muon track, measured with this prototype, is shown in figure 2.10. The top picture shows the arrival time of the signal versus the strip position, both for LEM and anode electrodes, allowing the spatial reconstruction of the track. The gray scale on the right is proportional to the signal amplitude. The bottom picture represents the recorded waveforms for all the channels. Notice that an excellent signal to noise ratio is visible. This example represents a proof of principle of operation of a double phase LAr LEM-TPC as a tracking device. Thus, respect to the final design of the LEM for the ArDM experiment, just to mention that the position readout is achieved by segmenting the upper LEM surface and the anode plate with 1.5 mm wide x and *y-strips* respectively, so there are 1024 readout channels which are AC coupled to charge sensitive preamplifiers located externally

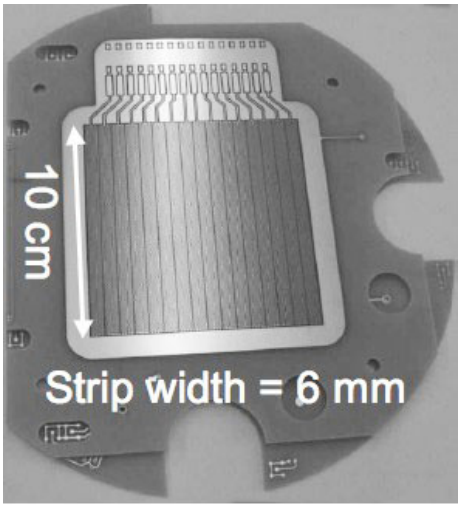

Figure 2.8: Top face of the prototype of the second LEM stage showing the hole pattern and the subdivision into strips.

on the top flange of the apparatus. On the other hand, with regard to the signal lines, we have used kapton flex-prints for signal transfers to the readout electronics. They will be connected on one side to the LEM board and exit the dewar through a slot cut in an UHV flange, sealed with a cryogenic epoxy-resin to maintain vacuum tightness.

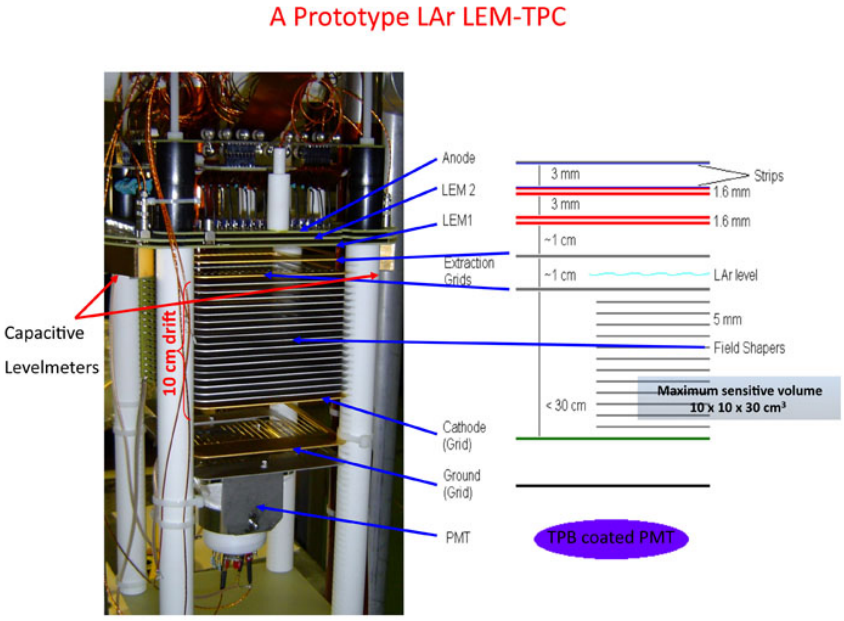

Figure 2.9: Left: Assembly of the LAr LEM-TPC prototype. Right: Schematic of the LEM-TPC setup showing the LAr level between the two extraction grids.

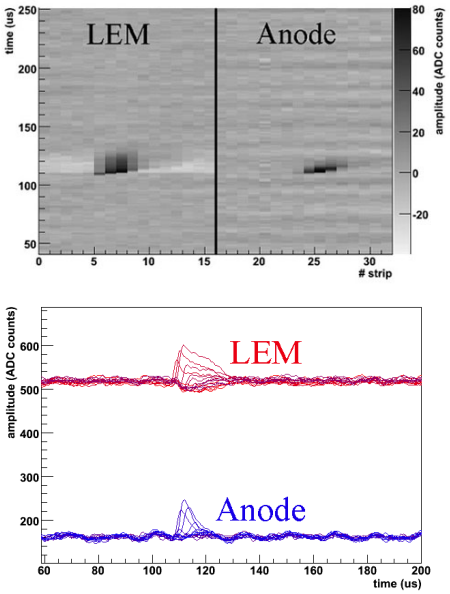

Figure 2.10: Display of a typical cosmic ray event in double phase operation. Channels 0-15 (upper traces in the bottom picture) are connected to the LEM strips and channels 16-31 (lower traces in the bottom picture) to anode strips.

In our Monte Carlo, we have carefully simulated the LEM as a circular board of 800 mm diameter an defined all its associated components.

2.2.4 Light detection system

Reactions involved in dark matter searches produce energy deposits in the range $10 - 100$ keV, which makes charge detection alone insufficient for particle identification. A good light detection for an optimal differentiation between signal and background is therefore required. Light readout is of capital importance for dark matter experiments, like ArDM, where, in addition to t_0 determination, the light is needed for energy measurements (by inferring the produced light and charge) and even for background discrimination through particle identification.

For light readout, the use of photomultiplier tubes (PMTs) is highly recommended as their time resolution allows to distinguish photons produced in a triplet state dimer (slow component) from those produced in a singlet state (fast component) [34]. As we will see, this helps improving background rejection capabilities. On the other hand, their high gain (up to 10^9) makes possible the detection of single photons without external amplification.

In this section and in first place, we will describe the components of the light detection system, mainly PMTs and reflecting sheets coated with a wavelength shifter. Later we will give some details about the chosen PMT configuration and show the light collection studies that we have carried out.

As we noticed in section 2.1, scintillation light in LAr has a wavelength of 128 nm, so it must be shifted to the visible range in order to be detected by our PMTs. Because of that, the inside of the field shaping rings is covered with 15 cylindrically arranged **reflecting sheets** (120×25 cm^2), made

out of the PTFE fabric Tetratex^{TM} (**TTX**), which are **coated with a thin layer** (1.0 mg/cm^2) **of TPB** (see figure 2.11). These sheets spread from the top ring to the cathode (see figure 2.12), clamped to the upper- and lowermost field shaping rings.

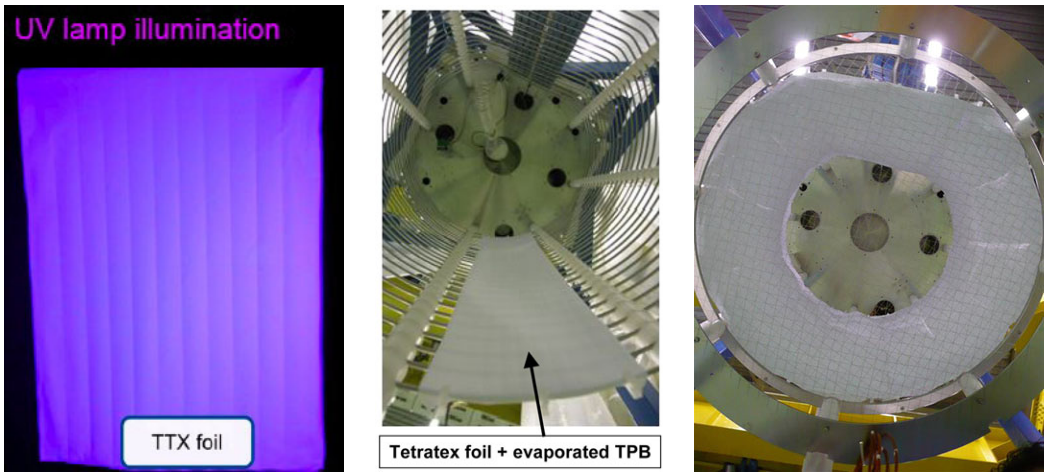

Figure 2.11: Left: Tetratex reflecting foil + evaporated TPB under UV lamp ilumination. Centre: View of a reflecting sheet installed in the inner detector. Pillars, field shaping rings and top flange are also visible. Right: Completed assembly of the reflecting sheets (down view).

TTX is an aligned polytetrafluoroethylene (PTFE) fibrous cloth and is nearly a 100% diffuse lambertian reflector. We employ TTX, from the company Donaldson Membranes, in the thickness of 254 μm. Several tests have been carried out before choosing TTX as the reflecting sheet [29]. In these tests, TPB coated TTX cloth has been found to be a superior reflector when compared with $3M^{TM}$ foil due to its better light yield and greater tolerance to TPB layer thickness. The optimum coating and reflector combination is found to be between 0.2 mg/cm^2 and 1.0 mg/cm^2 TPB deposited via evaporation on TTX cloth (see figure 2.13). In this figure, the visible difference between 0.2 mg/cm^2 sprayed and evaporated TPB on TTX cloth implies that spraying produces areas of low coating thickness and large inhomogeneity, while deposition via evaporation produces better coating uniformity. In addittion, TPB evaporated on TTX substrates has been found to be almost independent of thickness. Therefore, regarding the test results, TTX cloths coated with 1.0 mg/cm^2 TPB have been chosen for the ArDM reflectors.

TPB is a wavelength shifter which absorbs 128 nm light and re-emits it isotropically in the blue region with a peak at about 430 nm. In figure 2.14 we show the emission spectrum of TPB [35]. It has a high shiffting efficiency and a good absorption power in the VUV range. Members of ArDM collaboration have measured the efficiency of TPB at converting 128 nm light into visible range: it is $87 \pm 5\%$. Moreover, based on spectroradiometer measurements, TPB coated TTX is found to have $97 \pm 1.4\%$ reflectance at 430 nm for all coating thicknesses. That is a high enough value to provide a good light collection.

To simulate the reflecting sheets covered with TPB we have introduced the PTFE material in our Monte Carlo and taken into account the measured properties of TPB that we just mentioned above.

Photomultiplier tubes are the light detection devices we use. As it is well known, they produce a current proportional to the incident amount of light. Currently running noble liquid

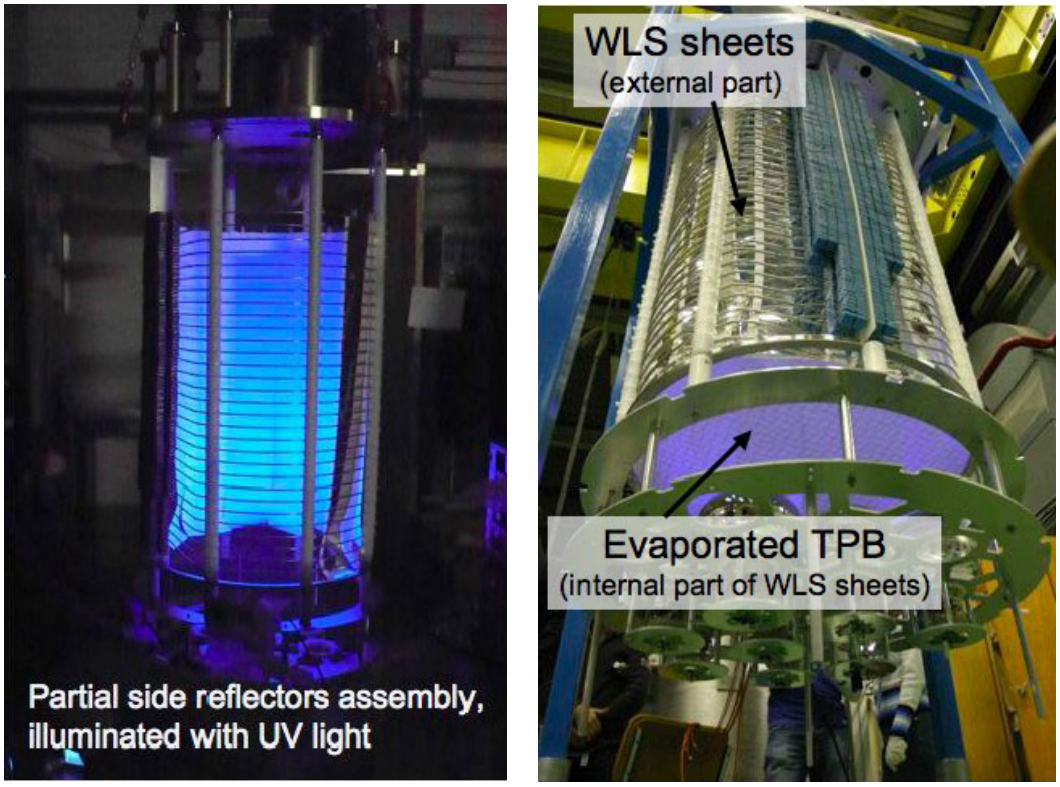

Figure 2.12: Left: Lateral reflectors with TPB coating assembly under UV lamp ilumination. Right: Completed assembly of the reflecting and wavelenght shifting system. External and internal parts of the reflecting sheets are visible.

dark matter detectors like WARP [36] and XENON [19], employ small size phototubes ($\sim$ 2-inch window) because of the relative small active volume of such prototypes (few liters). However, in our case, due to the large volume of ArDM experiment (about one tonne of LAr), it is better to install large area photocathode tubes (8-inch window). These large PMTs will allow coverage of bigger surfaces at lower cost, reducing at the same time the non sensitive surface (increasing the geometrical acceptance). Among the companies surveyed, only Electron Tubes Limited [37] and Hamamatsu [38] can offer large photocathode PMTs suitable to work under cryogenic conditions, in particular at LAr temperature.

Therefore, 14 PMTs of 8-inch diameter (type Hamamatsu R-5912-02-MOD) are installed outside of the drift region, just below the cathode. The PMT windows are also coated with TPB to convert directly impinging VUV photons. Figure 2.15 presents the optimum PMT window coatings obtained during a test, for different coating techniques (evaporation, spraying, paraloid and polystyrene matrices). From the results of this test, the best window coating was deduced as 0.05 mg/cm^2 TPB deposited via evaporation [29]. In addition, to shield the PMTs, a grounded grid has been installed, 120 mm below the cathode and 21 mm above the surface of PMTs. It is a stainless steel mesh with about the same dimensions than the cathode and a holding ring of 5 mm thick (see figure 2.16).

Since light collection is a fundamental aspect of our experiment, we give some details about

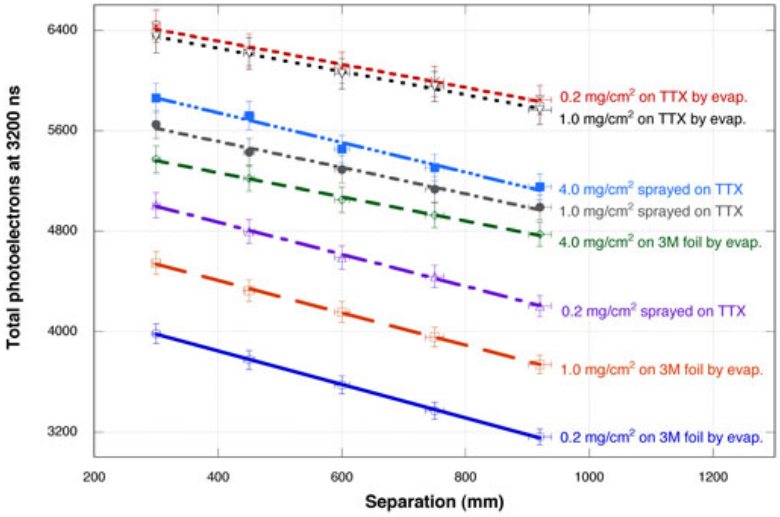

Figure 2.13: Total photoelectrons for 3200 ns purity against separation from the α source to PMT for TPB coated reflector walled tube.

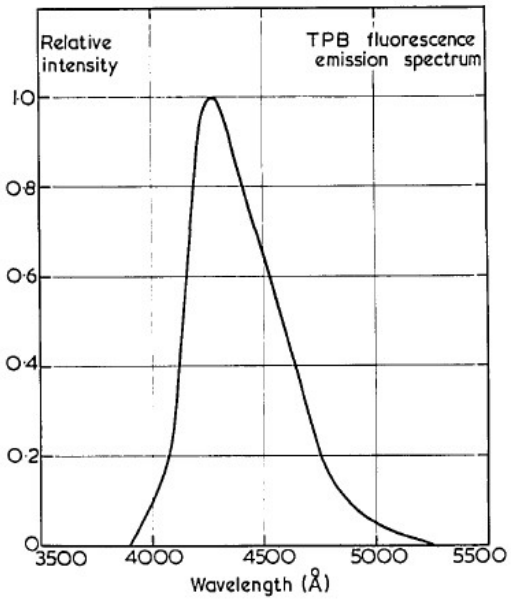

Figure 2.14: The emission spectrum of TPB fluorescence.

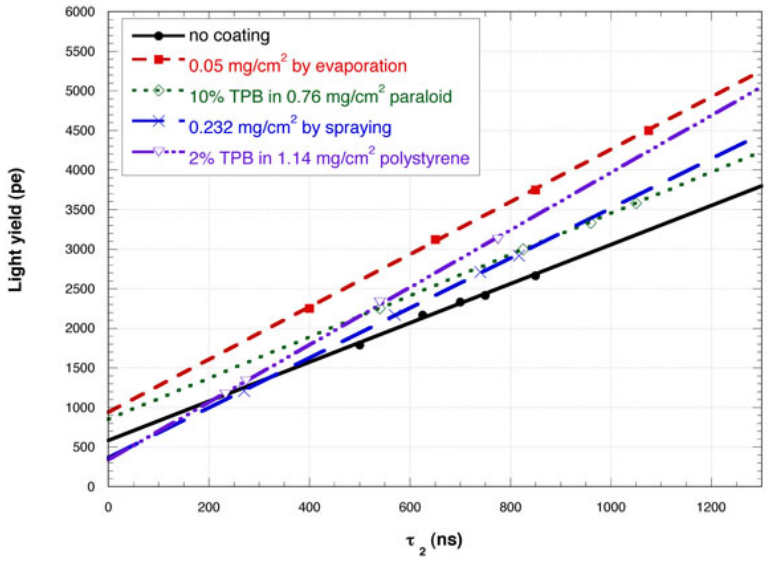

Figure 2.15: The optimum PMT window coatings (polysterene and paraloid matrices, evaporation and spraying). The best window coating is by evaporation with a thickness of 0.05 mg/cm^2, improving the total light collection by $38 \pm 3.4\%$ at 1000 ns purity compared to that collected with no PMT coating.

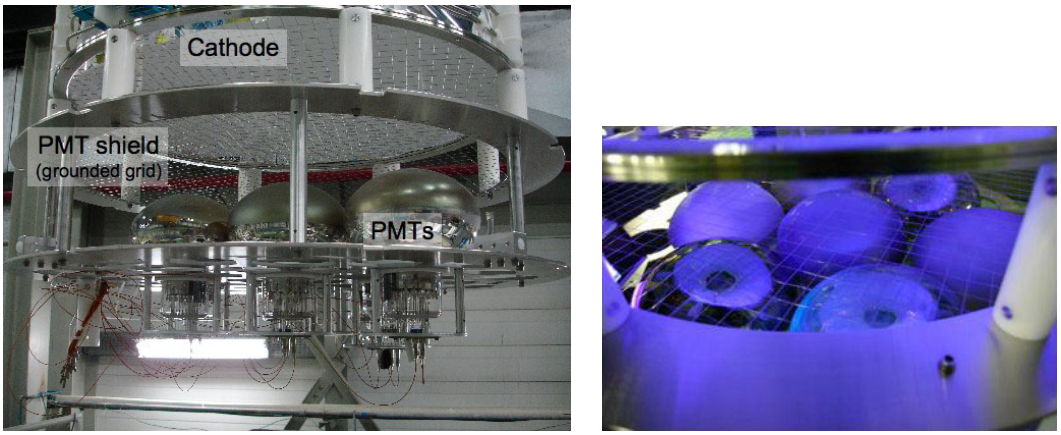

Figure 2.16: Left: Large photomultiplier tubes assembly. PMT shield is also visible. Right: PMTs with TPB coating under UV lamp ilumination.

why we have chosen this PMT configuration and how we have implemented it inside the GEANT4 simulation.

Light collection studies

In order to study which PMT configuration has a better light collection (mainly geometrical acceptance), we implemented three different ones in the Monte Carlo. These configurations were:

- 69 squared 3" PMTs, type Hamamatsu R-6237-01.
- 85 hexagonal 3" PMTs, type Hamamatsu R-6235-01.
- 14 hemispherical 8" PMTs, type Hamamatsu R-5912.

Out of the available models, we have chosen these PMTs because we intended to study configurations with different geometries and their properties match our experiment requirements: a good PMT response over a wide range of illumination levels and, naturally, proper behaviour at cryogenic temperatures O(100 K). The first two patterns use small PMTs (3-inch window) whereas the third one uses large PMTs (8-inch window). The shape of their PMT window has been precisely coded into the simulation (see figures 2.17, 2.18 and 2.19).

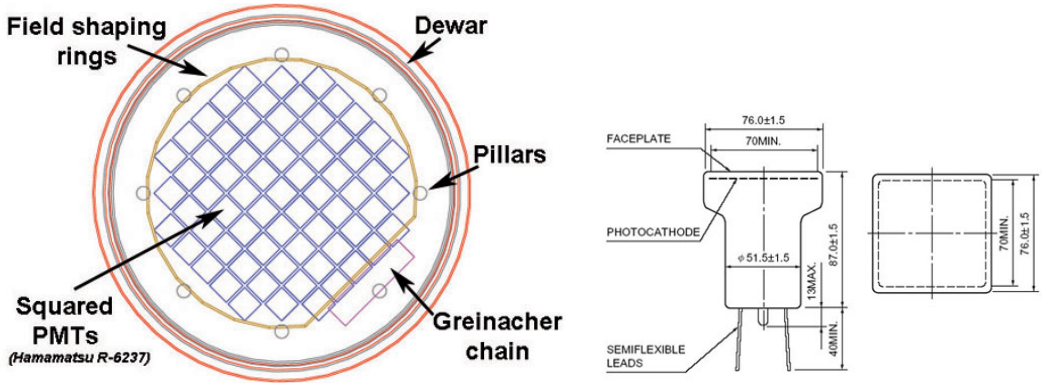

Figure 2.17: Left: GEANT4 simulated configuration of squared PMTs. Right: Scheme of a PMT type Hamamatsu R-6237-01.

For each configuration, we have studied the percentage of direct and total photons hitting the PMTs, as a function of the vertical position of the primary interaction point. By direct photons we mean those which do not touch the WLS (wavelength shifter) evaporated on the sheets placed inside the field shaping rings. Therefore they are not shifted to visible light before hitting the PMT. Likewise, total photons refer to all photons, shifted or not. To do these studies, we randomly shot scintillation photons from all over the fiducial volume of our detector. In figures 2.20, 2.21 and 2.22 we show the results obtained. The center of the detector is taken as the 0 cm reference. Negative distances refer to positions close to the detector bottom, while positives ones correspond to locations close to the LAr surface.

The percentage of direct photons w.r.t. photons hitting PMTs is the same for the three configuration (see figure 2.20). As we expected, the closer the vertex position to the PMTs the higher percentage of direct photons collected. On average we obtain that ∼24% of photons hitting PMTs are direct. Naturally, as we just mentioned, close to the PMTs this percentage is higher, about 48% and near the dewar top the percentage is smaller, about 11%. If we do not consider the photocathode dimension for the case of the hemispherical PMTs, this configuration collects more photons than the other two (see figure 2.21). The photocathode of a PMT is the sensitive part of

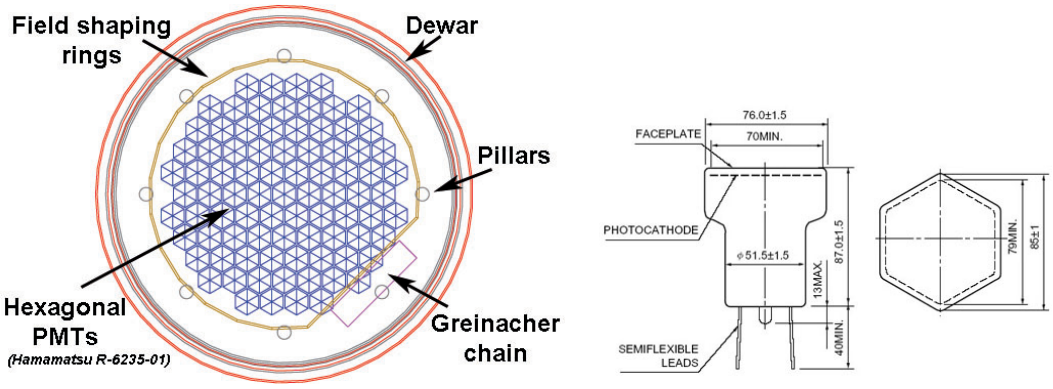

Figure 2.18: Left: GEANT4 simulated configuration of hexagonal PMTs. Right: Scheme of a PMT type Hamamatsu R-6235-01.

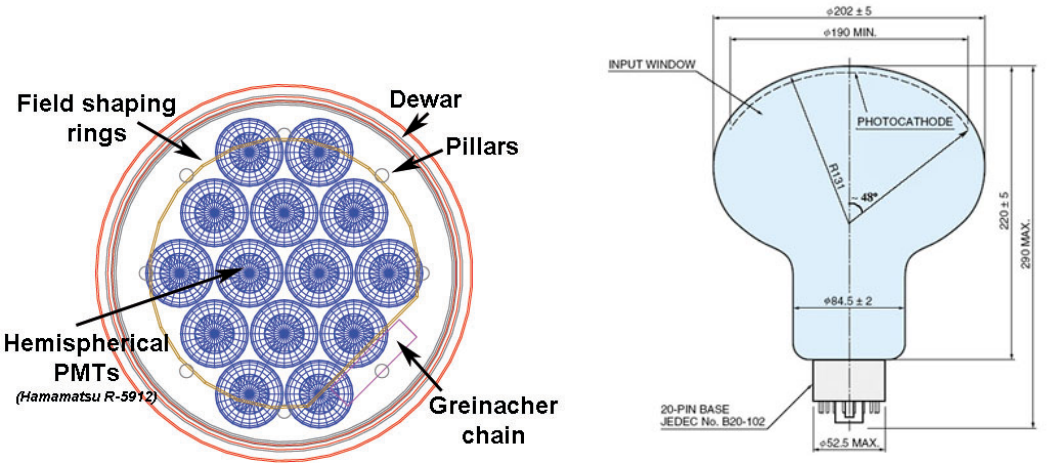

Figure 2.19: Left: GEANT4 simulated configuration of hemispherical PMTs. Right: Scheme of a PMT type Hamamatsu R-5912. Photocathode size is also shown.

the PMT in which the photoelectric conversion of the incoming light takes place. However, when the photocathode is properly taken into account (meaning that a cut of about 48° in the window of the hemispherical PMTs is done (figure 2.19)), the percentage of total photons detected by them is slightly lower (see figure 2.22). Here we have implemented accurately all PMT geometries and we obtain on average that about $21-23\%$ of light generated is collected by the PMTs (depending on the PMT configuration). Certainly, when the vertex position is near the PMTs this percentage is higher, about $30-32\%$ whereas if it is near the LAr surface the percentage is lower, about $16-17\%$.

Therefore, after these studies, as the light collection efficiency for the three configurations is very similar, *we have decided to use the one with only 14 large PMTs*, thus reducing the amount of readout channels and therefore the cost. Besides, as they have no plastic housing, their spatial packing is better than those offered by other a priori more compact solutions, such as the square or

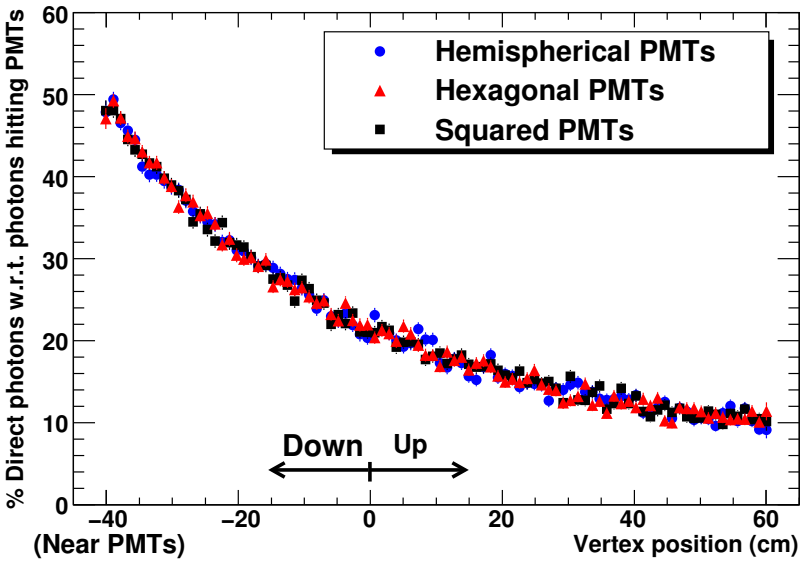

Figure 2.20: Percentage of direct photons hitting PMTs. Blue dots correspond to the configuration of hemispherical PMTs, red triangles to the hexagonal PMTs and black squares to the squared PMTs.

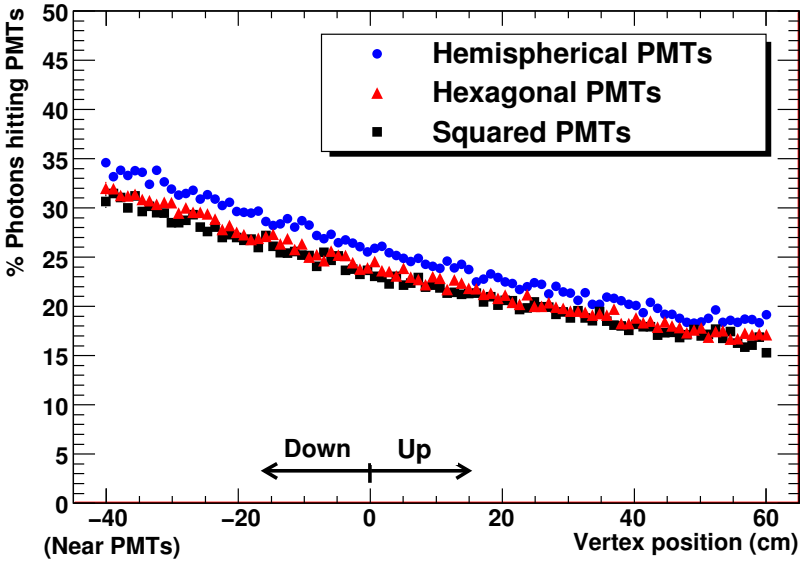

Figure 2.21: Percentage of total photons hitting PMTs. The photocathode of hemispherical PMTs has the same dimensions than the PMT window (blue dots).

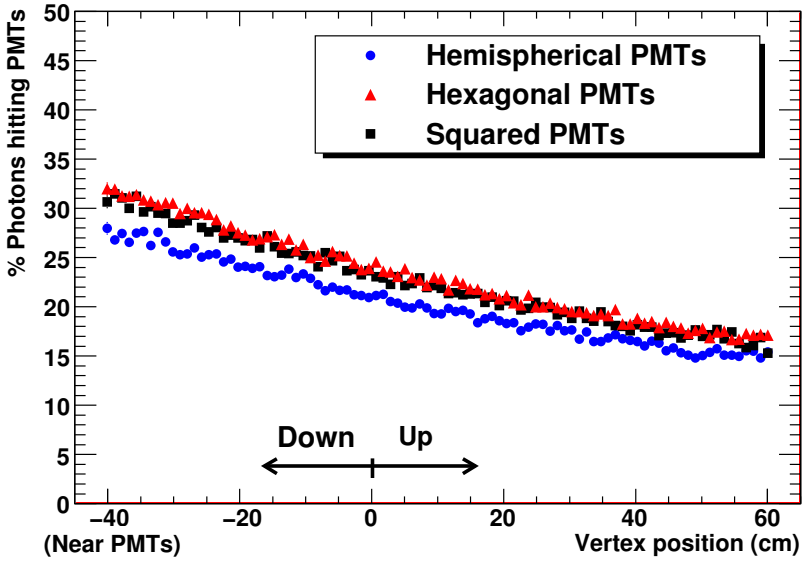

Figure 2.22: Percentage of total photons hitting PMTs. The photocathode size for hemispherical PMTs has been properly implemented (blue dots).

hexagonal PMTs. In addition, these hemispherical PMTs can be manufactured in low background glass with the great adavantage this represents for our physics studies.

Coding the behaviour of our PMTs

In order for the Monte Carlo simulation to model properly the PMT behaviour, it is necessary to include the **quantum efficiency** (QE) as a function of incident photon angle. The dominant effect comes simply from the solid angle sustended by PMT as a function of the angle of incidence. To model the PMT shape we have used a sphere of radius 131 mm and two ellipsoids, one of axis 99.9 mm and 73.1 mm and another of axis 101 mm and 78.3 mm (see figure 2.23). The photocathode sensitive area spans up to an angle of 48°.

The quantum efficiency is defined as the ratio between the number of electrons produced in the photocathode over the number of incoming photons. Usually, QE can only be measured convoluted with collection efficiency, a property of the dynode chain. In general, the probability that photoelectrons will land on the effective area of the first dynode is termed as the collection efficiency. This effective area is the area where photoelectrons can be multiplied effectively at the successive dynode stages without deviating from their favorable trajectories. This value increases with the voltage between cathode and first dynode, being almost 100% for a wide range of values.

For our PMTs, the relative efficiency as a function of incident photon angle w.r.t. the PMT tube axis has been implemented applying the following parameterization [39]:

$$f(\theta) = 1 + a_2\theta^2 + a_4\theta^4 + a_6\theta^6 \tag{2.1}$$

where:
θ = angle of incident light from the tube axis measured in degrees.

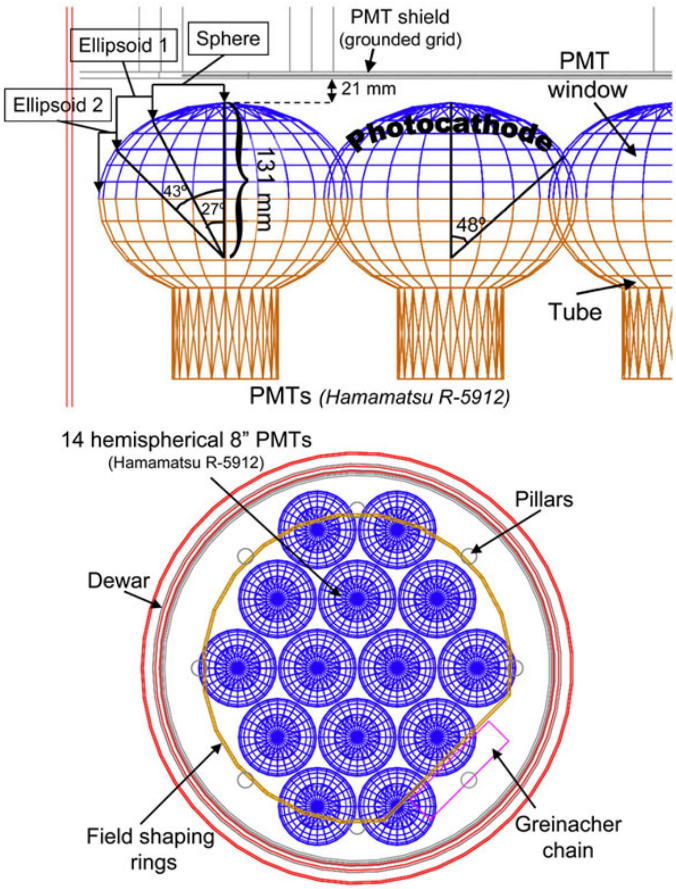

Figure 2.23: Simulated hemispherical PMTs in GEANT4. Top: Lateral view of PMTs. Geometrical shapes used to model PMT window (blue) and the photocathode angle are pointed out. Bottom: Top view of PMT configuration.

$a_2 = -1.181 \times 10^{-4}$
$a_4 = 4.906 \times 10^{-9}$
$a_6 = -7.213 \times 10^{-14}$

In figure 2.24 we show a plot for this relative efficiency. It is normalized to max $E_{rel} = 1$ at $\theta = 0°$ and it has a roughly bell-shape, as one would expect from the shape of the tubes.

Then, we have coded QE as the result of multiplying this function of incident photon angle by the value of the QE peak:

$$\text{QE}(\theta) = \text{QE peak} \times f(\theta) \tag{2.2}$$

We have used a QE peak of 20% for Hamamatsu R-5912 PMTs, since that is the value of QE measured for a wavelength of about 430 nm. The experimental measurements of QE at LAr temperature were carried out at the cryogenic laboratory of the Granada University High Energy group [40].

In addition, we have taken into account another effect which affects the PMT efficiency: the angle of incident light w.r.t. the perpendicular at the surface on the impact position (see figure 2.25).

We have modeled the dependence of the PMT behaviour with this angle as well. This angular response has been coded as a cos(ϕ) curve [41]. In summary, the final PMT efficiency is given by:

$$\text{Efficiency}_{PMT} = QE(\theta) \times \mid cos(\phi) \mid \tag{2.3}$$

where:
θ = angle of incident light w.r.t. the tube axis,
ϕ = angle of incident photon w.r.t. the perpendicular on the impact point.

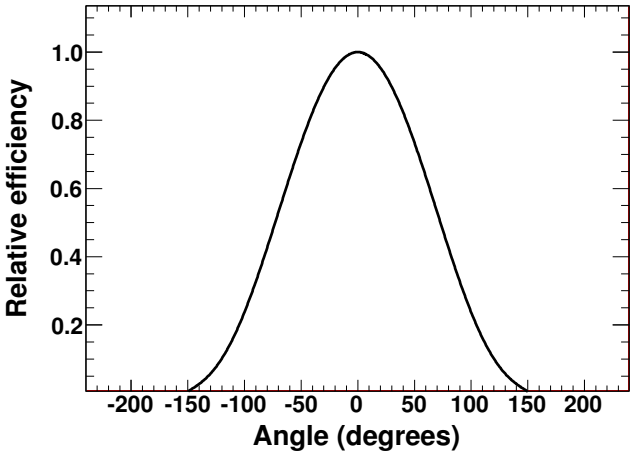

Figure 2.24: Relative efficiency versus incident photon angle θ w.r.t. PMT tube axis.

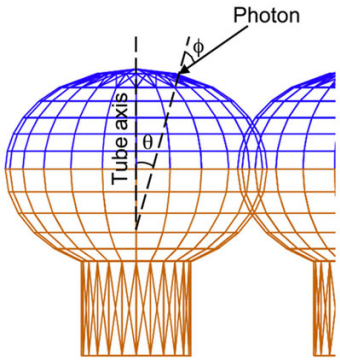

Figure 2.25: Lateral view of a PMT. The two angles taken into account in our GEANT4 simulation are shown. θ is the angle of incident photon w.r.t. the tube axis while ϕ is the one w.r.t. the perpendicular on the impact point.

Scintillation photons in our Monte Carlo

For the studies of light collection, we must simulate the properties of liquid and gaseous argon, the scintillation photons and their interactions. In figure 2.26 we show the energy spectrum used for

these photons in LAr. Notice that peak corresponds to about 9.69 eV (128 nm).

The propagation of these photons in argon and their interactions with the different components of the chamber are simulated using the optical processes, from GEANT4, in particular the Rayleigh scattering and refraction/reflection. In fact, we have simulated the Rayleigh scattering length $l_R(\lambda; \epsilon_{Ar}; \rho_{Ar})$ using equations given in [42] (ϵ_{Ar} and ρ_{Ar} are the Ar dielectric constant and density). We calculate the refractive index of argon from the Bideau-Sellmeier formula [43]. Furthermore, no light absorption is considered since we suppose an infinite attenuation length for pure LAr.

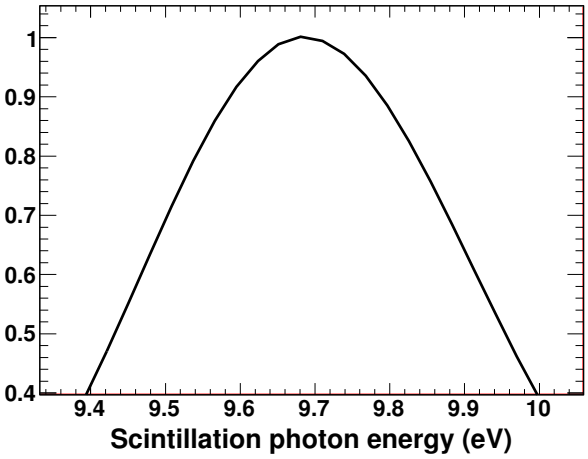

Figure 2.26: Energy spectrum of simulated scintillation photons in liquid argon.

We have described the main components of our experiment and given some details about the implementation of scintillation photons and light collection in our simulation. The inner detector components have been carefully implemented in our Monte Carlo, taking into account their dimensions, materials and optical properties. In figure 2.27 we show a view of the simulated detector as a whole: PMTs, reflecting sheets, LEM, cathode, Greinacher chain, field shaping rings and pillars are visible. On the other hand, in picture 2.28 we see the current state of our detector. The inner detector assembly is taking place at CERN. Our one tonne prototype is intended to go through a series of surface tests in order to prove that all the adopted solutions for electric field, charge readout and light readout work according to expectations.

2.3 Experimental tests in Gas Argon

In this section we describe some measurements carried out in gas argon with the ArDM prototype during a first technical run. We compare the light collection data with the Monte Carlo predictions. This will help us to assess the reliability of the detector simulation code.

From September to November 2007, a part of the light system of the ArDM detector was assembled, brought inside the experiment dewar and put to test to understand its performance. This included all the wavelength shifter foils together with a half of the final experiment PMTs (see figure 2.29).

During this test period, the detector was filled with gaseous argon to study the light acquisition system (PMTs + reflectors) performance under the interactions produced by alpha particles.

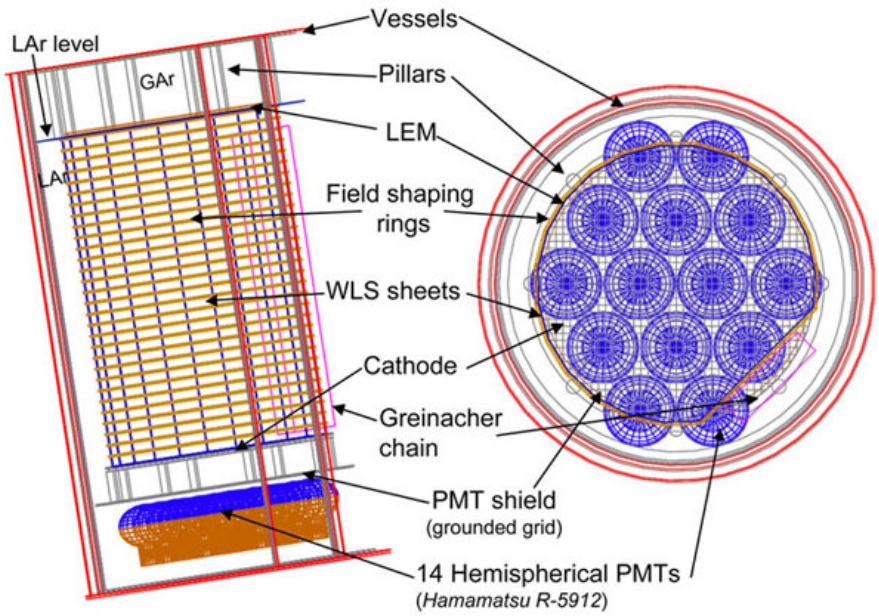

Figure 2.27: Lateral and top view of the simulated ArDM detector in GEANT4.

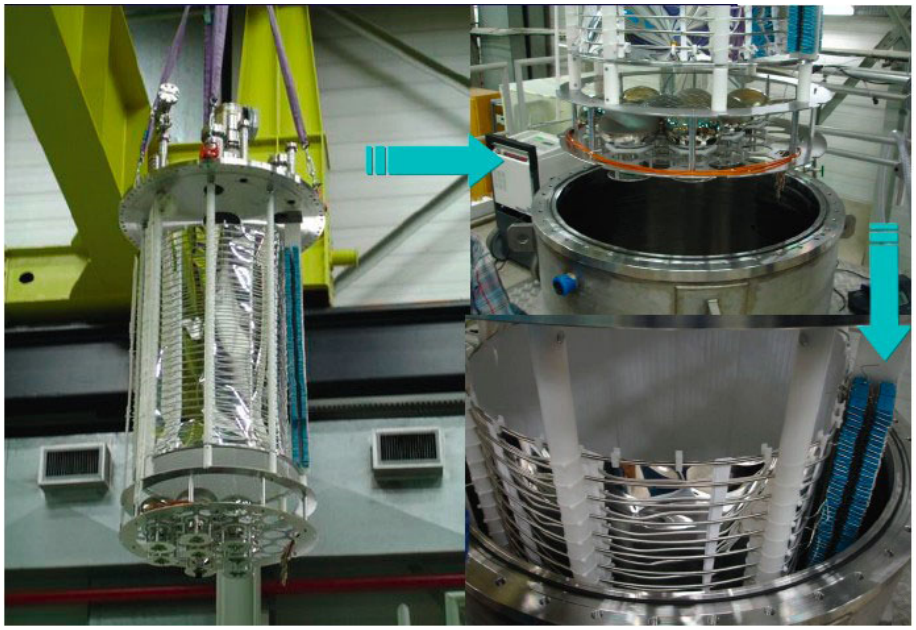

Figure 2.28: Inner detector installation (November 2007).

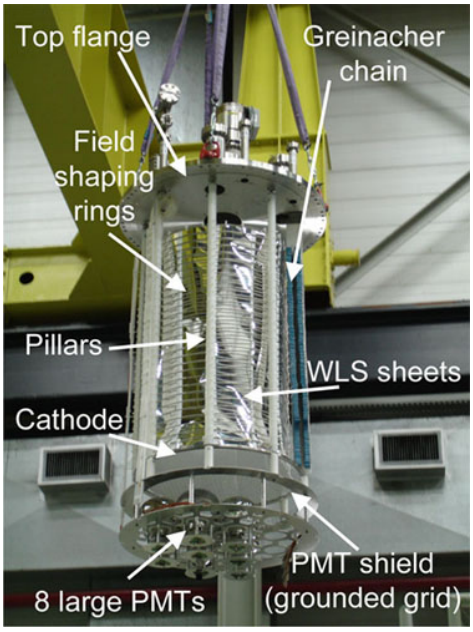

Figure 2.29: Setup used during the first surface test of the ArDM prototype.

2.3.1 Light measurements

The first series of surface measurements aimed to assess the performance of the light acquisition system prior to full detector assembly. Measurements were carried out by means of radiactive sources. This was accomplished by installing on the top flange a metallic rod that could be moved inside the dewar without breaking the vacuum thanks to a magnet placed in the outside (see figure 2.30). At the end of this metallic rod, a LED was installed, providing illumination of the PMTs, together with an alpha source[1]. The alpha source was placed inside a capsule of palladium for safety purposes, which made the alpha energy to decrease in $\sim$ 1 MeV, resulting in a total deposited energy of 4.4 MeV.

During these tests only the light system and the slow control were working in the experiment, while all the electric field system, charge readout, and argon recirculation systems were switched off.

Since the argon recirculation system was not available during these tests, a method different from the final one for the argon filling was adopted. The dewar was pumped for more than 24 hours until a good vacuum was reached inside (10^{-5} mbar). Then it was filled with gaseous argon to take away the impurities left and vacuum was done again. Finally the dewar was filled from very pure gaseous "Argon 60" bottles, and the measurements with the alpha source could be done. After one to two days, the purity inside the experiment degraded and was not good enough to take data. New measurements demanded repetition of the whole process, previously described.

For these tests of the light system only the central 8 PMTs were installed, using three different models of PMTs: ETL 9357 KFLB, Hamamatsu R-5912-MOD and Hamamatsu R-5912-02-MOD, since we wanted to test in-situ the performance of every one of them. These PMTs were placed as shown in figure 2.31. Their positions were chosen to be the closest to the centre of the detector

[1] ^{241}Am $\sim$35.8 KBq activity, α-energy 5.3 MeV

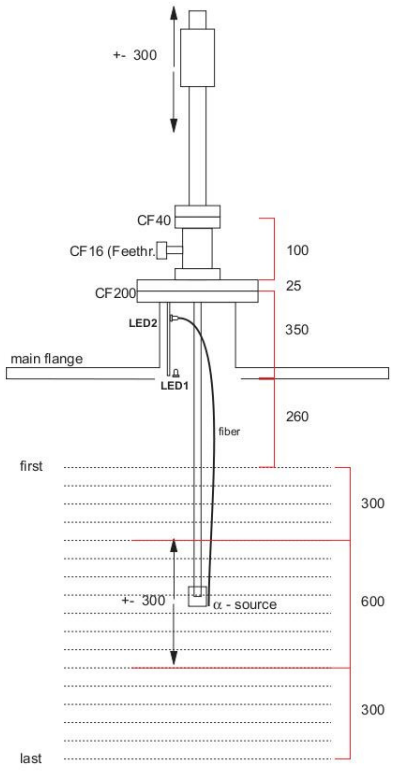

Figure 2.30: Schematic of the setup used for the first surface tests. A movable α-source and a LED are attached at the end of a rod which can be moved through a magnetically connected external piece. Another LED is fixed in the top of the detector.

and to have the smallest surface of the PMT outside the region delimited by field shaping rings.

Figure 2.31: Positions of the PMTs during the first surface test in the ArDM experiment. The position of the field shaping rings is marked with a white line. The first line on every PMT refers to the coating procedure (see text) and if the window has been shotblasted. The second line is the PMT model and the third one the serial number used in our simulation.

As already mentioned, VUV light produced in the events is shifted to visible light by means of TPB coated sheets placed in the inner side of the field shaping rings. However, some photons can reach PMTs without hitting the sheets (direct photons). To study the possibility to collect as well these photons, some of the PMTs have been coated with TPB to convert the 128 nm direct light to visible light that can be detected by the PMTs. Those uncoated are referred to as "unctd" in figure 2.31. Two different procedures have been used in order to establish which one produces more stable and efficient coating:

1. The PMT is placed in a chamber in which vacuum is done. A TPB sample is placed in front of the PMT and slowly heated by means of a resistor. When the TPB evaporates, it produces an homogeneous coating of the PMT. PMTs coated using this method are referred to as "evap" in figure 2.31. The thickness of TPB evaporated onto our PMTs is 0.05 mg/cm^2 and is constant irrespective of the position on the PMT face.

2. The PMT is dipped in a solution of chloroform, TPB and PRL, a polymer to make more stable the deposition. When it comes out, the chloroform evaporates very fast, and only TPB

and PRL remain. This produces a coating almost transparent for visible light that could help a more efficient collection of shifted light. PMTs coated using this method are referred to as "TPB/PRL" in figure 2.31.

During these tests, only gaseous argon was used. Given the low rupture voltage in this medium, some of the PMTs could not operate at their rated voltage due to spark production. Data could only be collected from 6 of the PMTs (five R-5912-02 and one R-5912). This, however, will not be a problem when working in LAr, where every PMT has been individually tested and with a much higher rupture voltage.

The first measurements carried out have been coincidence measurements in order to set an appropriate trigger for the source. We have measured the number of coincidences between PMTs as a function of the threshold level, i.e., as a function of the event energy [22]. We have repeated the measurement for different number of PMTs in coincidence (i.e., different majority threshold). From this measurement, it has been decided to consider as trigger for the rest of the measurements, an event in which four of the PMTs have a signal above the valley simultaneously. Results for 4 PMTs simultaneous signals are shown in figure 2.32, for different positions of the alpha source. It can be seen clearly that the trend for 4 PMTs is similar to the expected behaviour of the source, with the number of events decreasing constantly with energy and a maximum threshold over which no events can be seen.

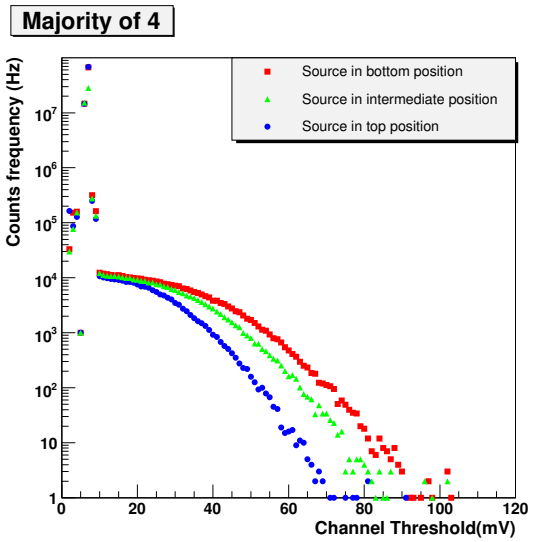

Figure 2.32: Number of counts with a coincidence of at least 4 PMTs with the ^{241}Am alpha source in gaseous argon.

On the other hand, we have carried out two tests at 1.1 bar, one at room temperature (300 K) and another one at cryogenic temperature (88 K), taking measurements with the alpha source at different positions for all of the 6 PMTs. We present the experimental data taken during these tests in figures 2.33 and 2.34. They show the average number of photoelectrons measured at different distances from the center of the detector by each of the PMTs, assuming clean gas. Both of them correspond to a pressure of 1.1 bar and a temperature of 300 K and 88 K, respectively. In these plots, negative distances refer to positions close to the top, while positive ones correspond to those

close to the bottom.

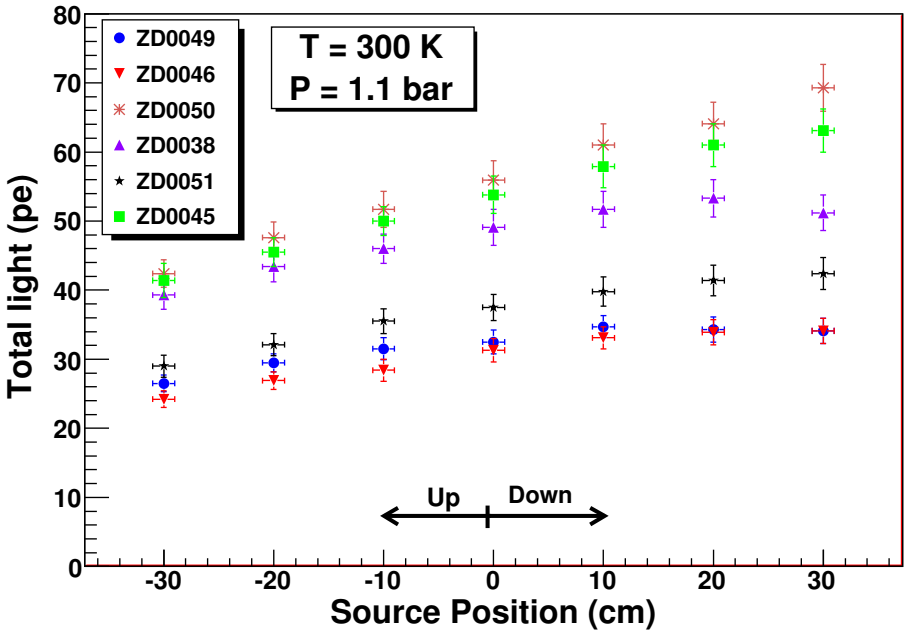

Figure 2.33: Average number of photoelectrons measured at 1.1 bar and 300 K.

As expected, the closer the source to the PMTs, the higher number of detected photoelectrons. There are two clear regions differentiated in the plot: the upper one, corresponding to those PMTs in the center of the detector; and the lower one, to those which are on the side and whose collection window is not completely inside the detection area. A second effect visible in this plot is that there are two PMTs for which the number of seen photoelectrons does not increase with distance uniformly. These two PMTs (ZD0038 and ZD0049) are those which are not coated with TPB and hence they are only sensitive to shifted light. The observed behaviour can be explained by considering that once the source is close enough, there is no decrease in the amount of indirect light and only the direct one increases.

Therefore, through these tests, we have proved the satisfactory operation of the PMTs inside the dewar and the good performance of the acquisition electronics.

2.3.2 Comparison with Monte Carlo simulation

We have already shown the experimental measurements taken in gas argon at 300 K and 88 K during the test period. As we intend to assess the reliability of our Monte Carlo, we simulate alpha particles at different heights from the center of the detector dewar. The produced photons are tracked inside the detector and we measure the percentage of photoelectrons seen by each PMT.

We outline the procedure followed along this section:

1. We fix the reflectivity value for the detector components and the efficiency of the TPB, as well.

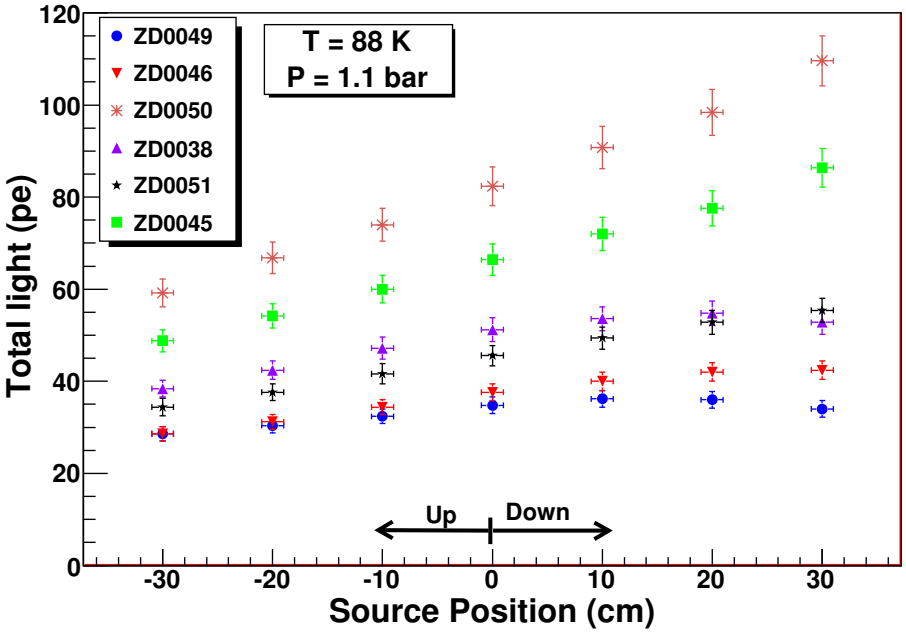

Figure 2.34: Average number of photoelectrons measured at 1.1 bar and 88 K.

2. Since we only have measured the QE curve for the PMT with serial number ZD0038, we will compare the measured photoelectrons detected by this PMT with the prediction given by the Monte Carlo.

3. This comparison will be used to check the reliability of our Monte Carlo.

4. We will use our simulation to predict the QE of the rest of the PMTs.

5. We will show the how well our Monte Carlo agrees with the experimental measurements.

6. To end, we will give the prediction of the light yield in LAr. That is a fundamental parameter for the physical studies carried out with our detector.

Therefore, in a first step, we itemize the *main modifications introduced in our Monte Carlo* in order to simulate properly the experimental setup used during the first surface tests:

- Inner vessel is filled only with gaseous argon.
- Absorption and Rayleigh scattering are not considered.
- Density of gas argon at 88 K is about three times higher than at 300 K (pressure in both cases was the same, 1.1 bar).
- LEM is not taken into account (in this first run we did not have it yet) .
- Only 8 large PMTs are simulated and placed as in the experimental setup (see figure 2.35).

- The rest of the inner detector components are simulated.
- Alphas of 4.4 MeV are generated at different heights. They quickly slow down since the range of alpha particles in argon at 1 bar of pressure is small (about 48 mm) [44].
- A yield of about 72 eV/gamma [45] is considered in gas argon at 1.1 bar.

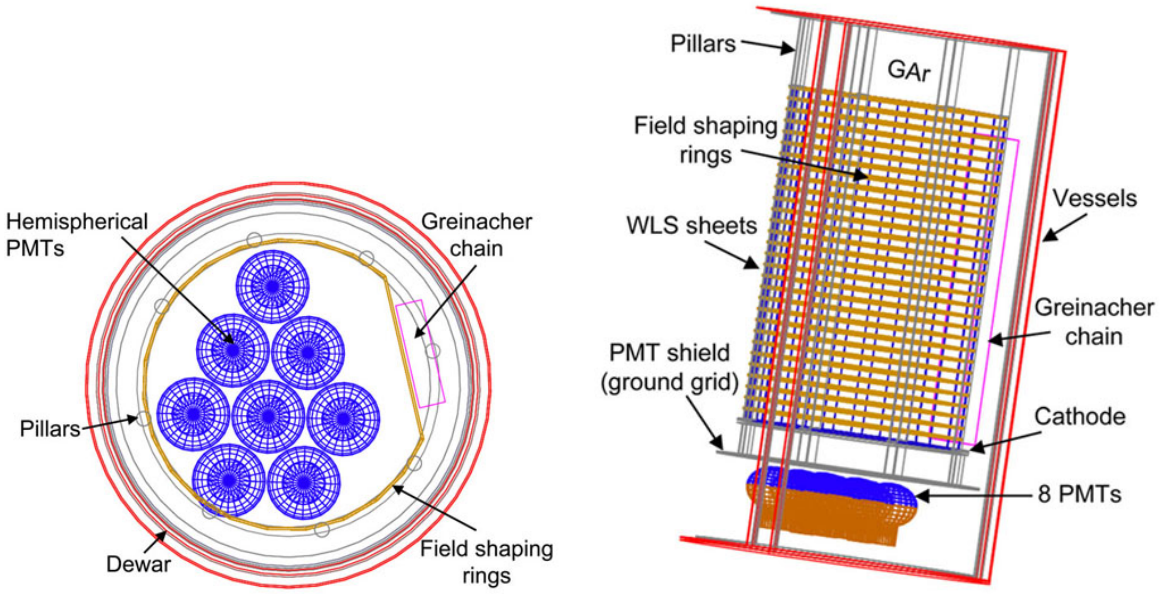

Figure 2.35: Top: PMTs simulated in GEANT4. They have been placed as they are mounted in the prototype. Right: Lateral view of the simulated experimental setup in GEANT4.

The *optical properties* of materials used in the simulation are in table 2.2 and the *TPB efficiency* used is detailed in table 2.3. We consider that blasted glass windows have a better and more uniform response from the TPB coating [46]. We do not expect any change in the TPB efficiency due to the different temperatures of the gaseous argon in our tests, so we have used the same efficiency at both temperatures, 300 and 88 K. In addition, we have taken into account that uncoated PMTs only detect indirect light while the coated ones are able to collect direct plus indirect photons.

Detector component	Light reflectivity
Stainless steel components	20%
Polyethylene pillars	50%
Reflector sheets covered with TPB	97%

Table 2.2: Percentage of light reflectivity for the main detector components [47, 29].

Now, to compute the QE of the PMTs in the Monte Carlo, since the six PMTs working in gas argon are Hamamatsu R-5912, we have used the equation 2.3 (see section 2.2.4). Hence, the angles of incident photon w.r.t. the PMT tube axis as well as w.r.t. the perpendicular on the impact

TPB covering the reflecting sheets	30% total conversion efficiency (including absorption efficiency and conversion efficiency of gamma-to-gamma)
TPB covering the PMT windows	30% in smooth glass windows (ZD0050, ZD0046, ZD0045) 32% in blasted glass windows (ZD0051)

Table 2.3: Efficiency considered in our Monte Carlo for the TPB covering the reflecting sheets and the PMT windows.

point of the PMT surface have been taken into account. To apply this QE equation we need to know the QE peak for each PMT.

Among all our working PMTs, *we have only measured the QE curve for the PMT with serial number ZD0038*, at the cryolab in Granada [40]. Then we have used the measured value of QE for a wavelength of 430 nm as the QE peak for this PMT in our Monte Carlo. The QE curve for the rest of PMTs has not been measured at the cryolab. We compare the experimental measurements of detected photoelectrons, for PMT number ZD0038, with the predicted values given by the Monte Carlo (see figures 2.36 and 2.38). Since there is a *good agreement* of the simulation with respect to the experimental data, we deduce that the modifications and the different parameters included in our Monte Carlo (optical properties of the detector components, TPB efficiency and the considered alpha yield) are correct.

Once we are sure about the reliability of all the parameters introduced in our Monte Carlo, *we can use the simulation to predict the QE peaks for the rest of PMTs*. They will be in the ranges: from 10 to 16% at room temperature and from 14 to 20% at cryogenic temperature. In table 2.4 we show the values of QE peaks used in our simulation for each PMT at the temperatures of both tests, 300 and 88 K (pressure was 1.1 bar in both cases). As expected, the QE of the PMT is higher at cold temperature and there are slight differences among PMTs. Indeed, it is found that the quantum efficiency properties of the PMTs change substantially with temperature, even if the Hamamatsu model is the same [40], so in order to have a good control of the performance of our detector and produce reliable physics results, *a careful measurement of QE(λ) in cryogenic conditions is mandatory before installing the PMTs into the dewar.*

PMT serial number	Peak of QE at T=300 K (in %)	Peak of QE at T=88 K (in %)
ZD0049	12.90	14.50
ZD0046	11.90	15.30
ZD0050	14.20	22.50
ZD0038	14.50	16.00
ZD0051	12.80	16.75
ZD0045	15.50	20.50

Table 2.4: Peak of QE used in our simulation for each PMT.

The comparison between real data and Monte Carlo, for each PMT and for both temperatures, 300 and 88 K, is shown in figures 2.36, 2.37, 2.38 and 2.39. We plot the average number of photoelectrons seen, at different distances from the centre of the detector, by each of the PMTs. Values are computed assuming a clean gas. As usual, negative distances refer to positions close to the top, while positive ones correspond to those close to the bottom. Error bars for Monte Carlo

and experimental measurements are the same order of magnitude so, for the sake of clarity in the plots, we have only represented the experimental ones.

Regarding the predicted average number of photoelectrons, **we observe a good agreement of our Monte Carlo with respect to the experimental measurements**. As expected, central PMTs detect more photoelectrons than the ones placed at the sides of the detector. The number of photoelectrons increases as the source is closer to the PMT surface. Furthermore, if we add now the number of photoelectrons that our six working PMTs have measured and extrapolate this number to the whole 14 hemispherical PMTs, we can compute the light yield for our 4.4 MeV alpha source. We obtain that, *in gas argon, the light yield is* $\sim 0.23 - 0.27$ *pe/keV*, depending on whether the temperature is 300 or 88 K.

In conclusion, this first set of measurements has allowed us to test the light collection system. It performed well. Our Monte Carlo simulation reliably reproduces the data. Hence it can be used to evaluate the physics performance of our detector when a search for dark matter is conducted in an underground lab.

Extrapolating these results to the ones expected when LAr is used is not straightforward, since there are several parameters that influence the light yield like pair creation energy or ionization density. They vary from gas to liquid phase. To make a light yield prediction for operation in LAr, we have considered a yield of 25 eV/gamma and a quenching factor of 0.3 [48]. Using this modified simulation for *liquid argon* and considering now the final configuration with 14 PMTs, we obtain a *light yield of 0.7 pe/keV*. Checks of this number will be done in the near future. At the time of this writing, the collaboration is starting a data taking campaign with LAr, once the detector and all the ancillary system have been certified to comply with the strict safety regulations imposed by CERN.

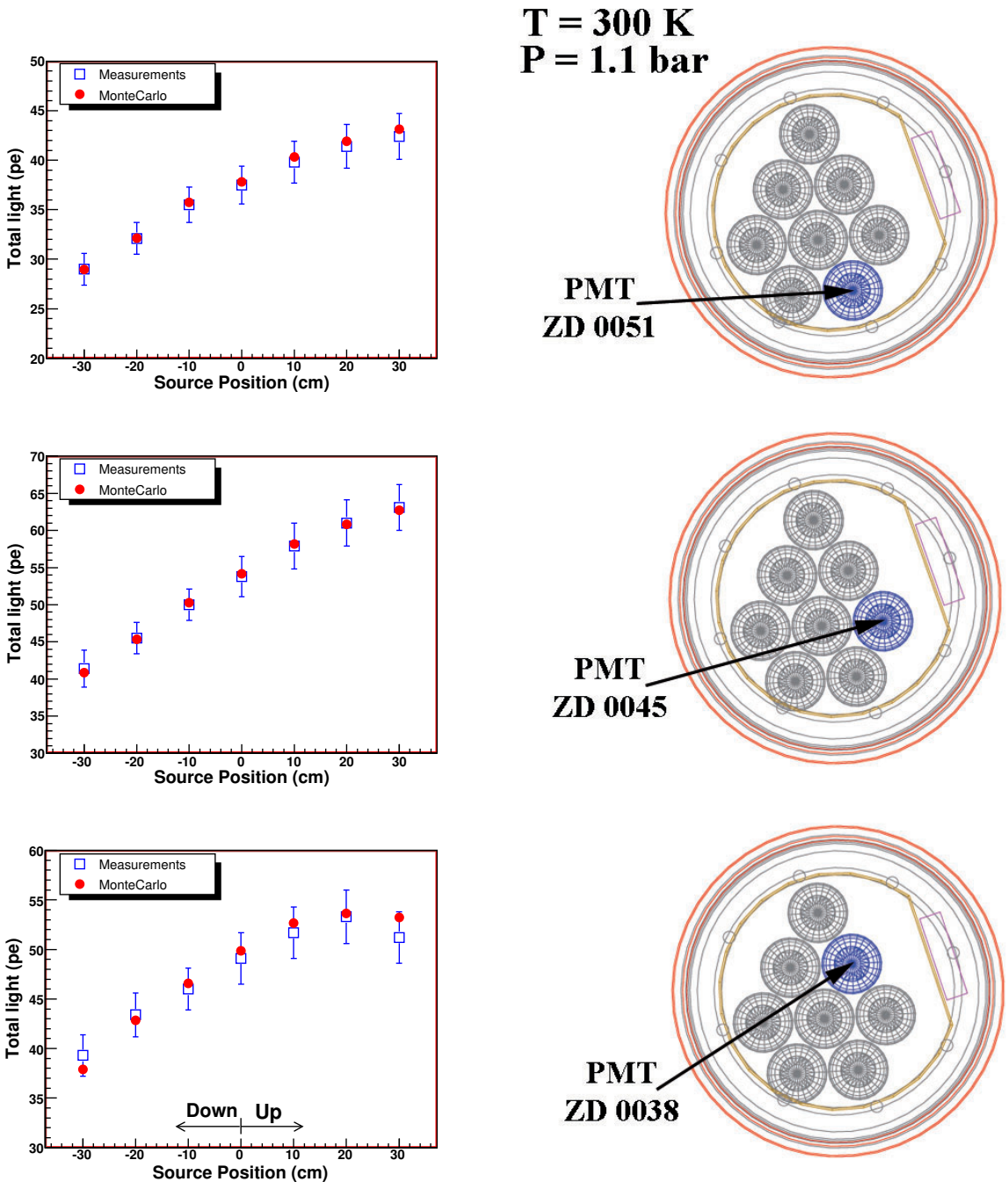

Figure 2.36: Comparison between experimental measurements in gaseous argon and Monte Carlo for PMTs with serial number ZD0051, ZD0045 and ZD0038. These results correspond to a pressure of 1.1 bar and a temperature of 300 K.

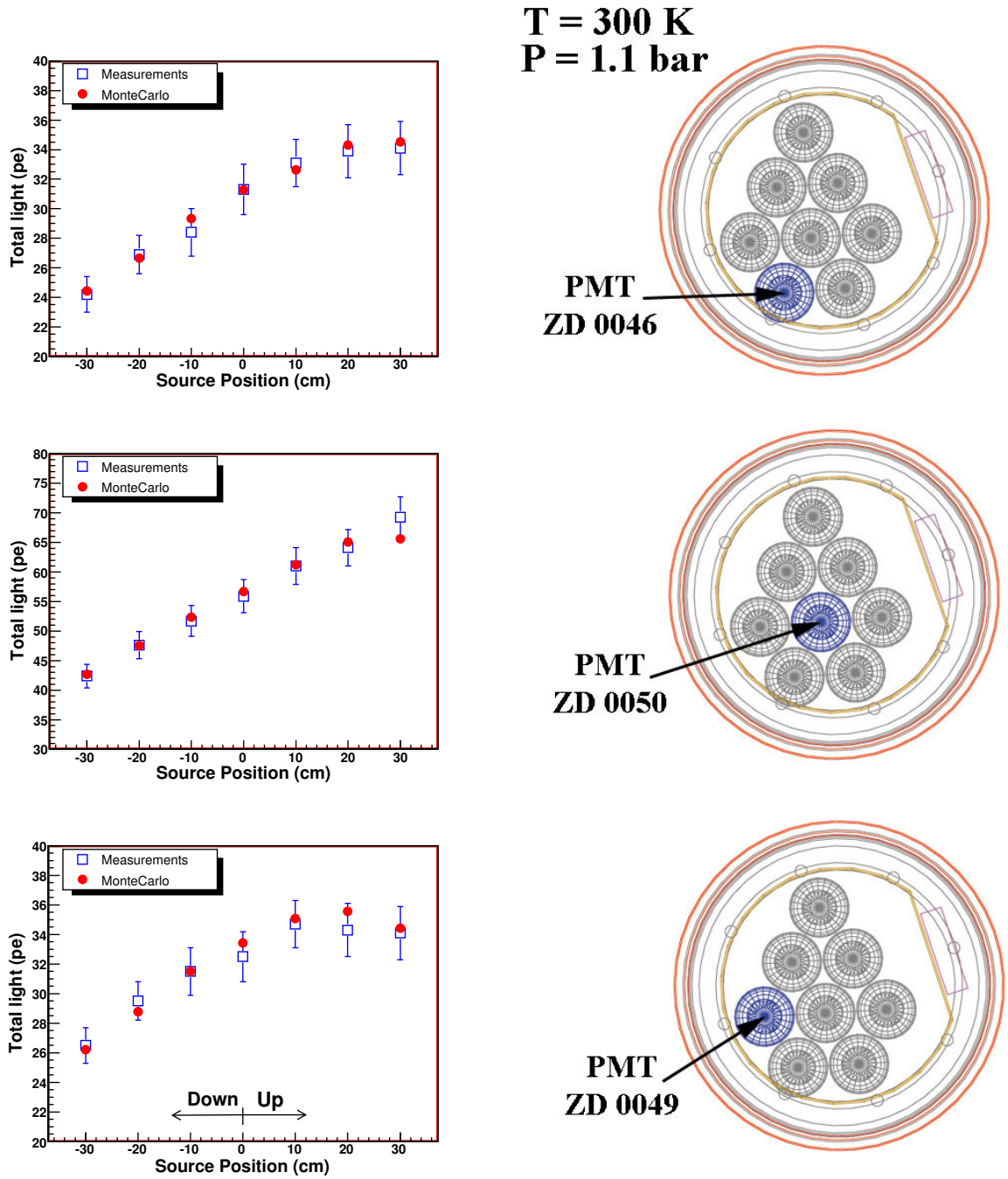

Figure 2.37: Comparison between experimental measurements in gaseous argon and Monte Carlo for PMTs with serial number ZD0046, ZD0050 and ZD0049. These results correspond to a pressure of 1.1 bar and a temperature of 300 K.

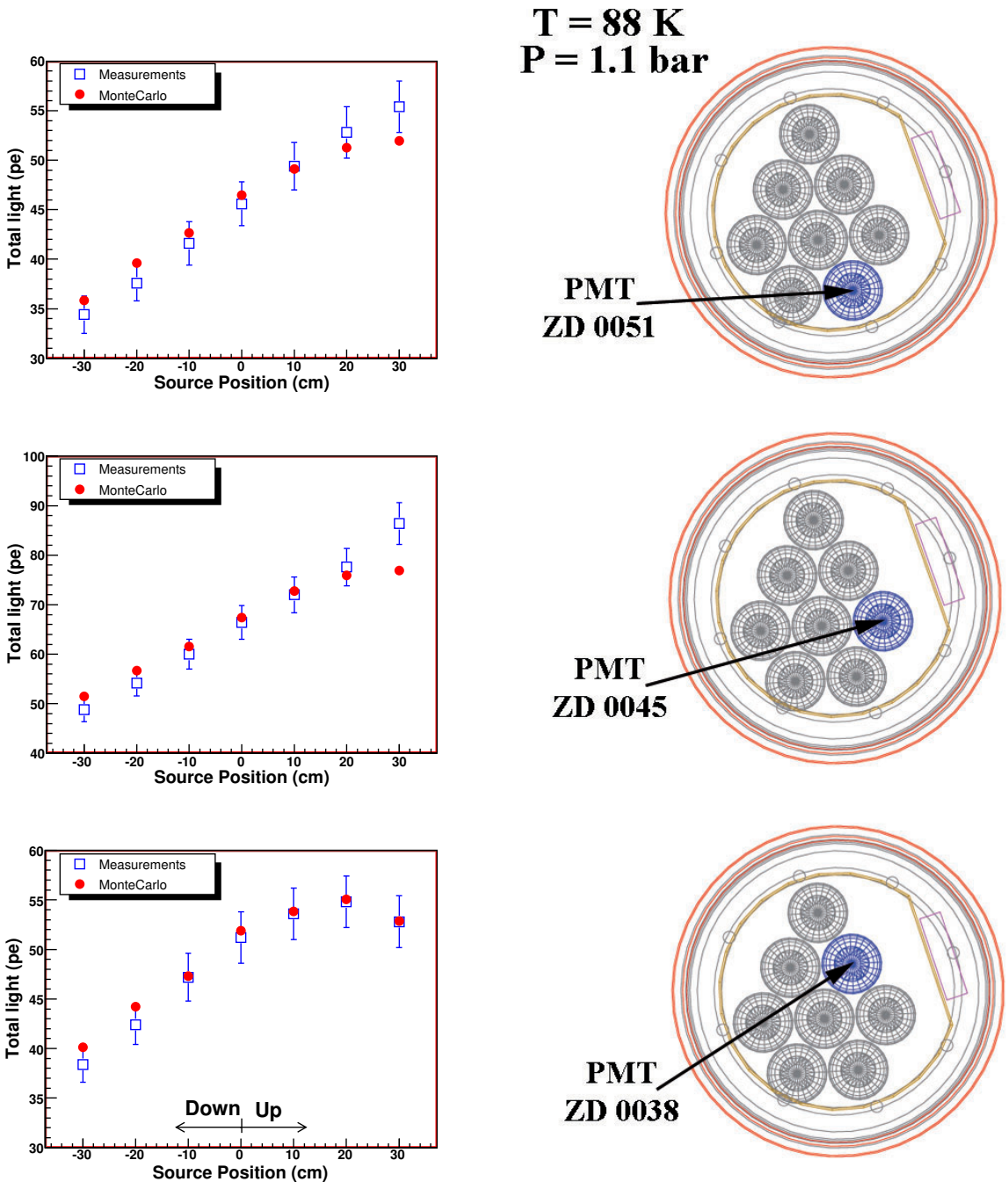

Figure 2.38: Comparison between experimental measurements in gaseous argon and Monte Carlo for PMTs with serial number ZD0051, ZD0045 and ZD0038. These results correspond to a pressure of 1.1 bar and a temperature of 88 K.

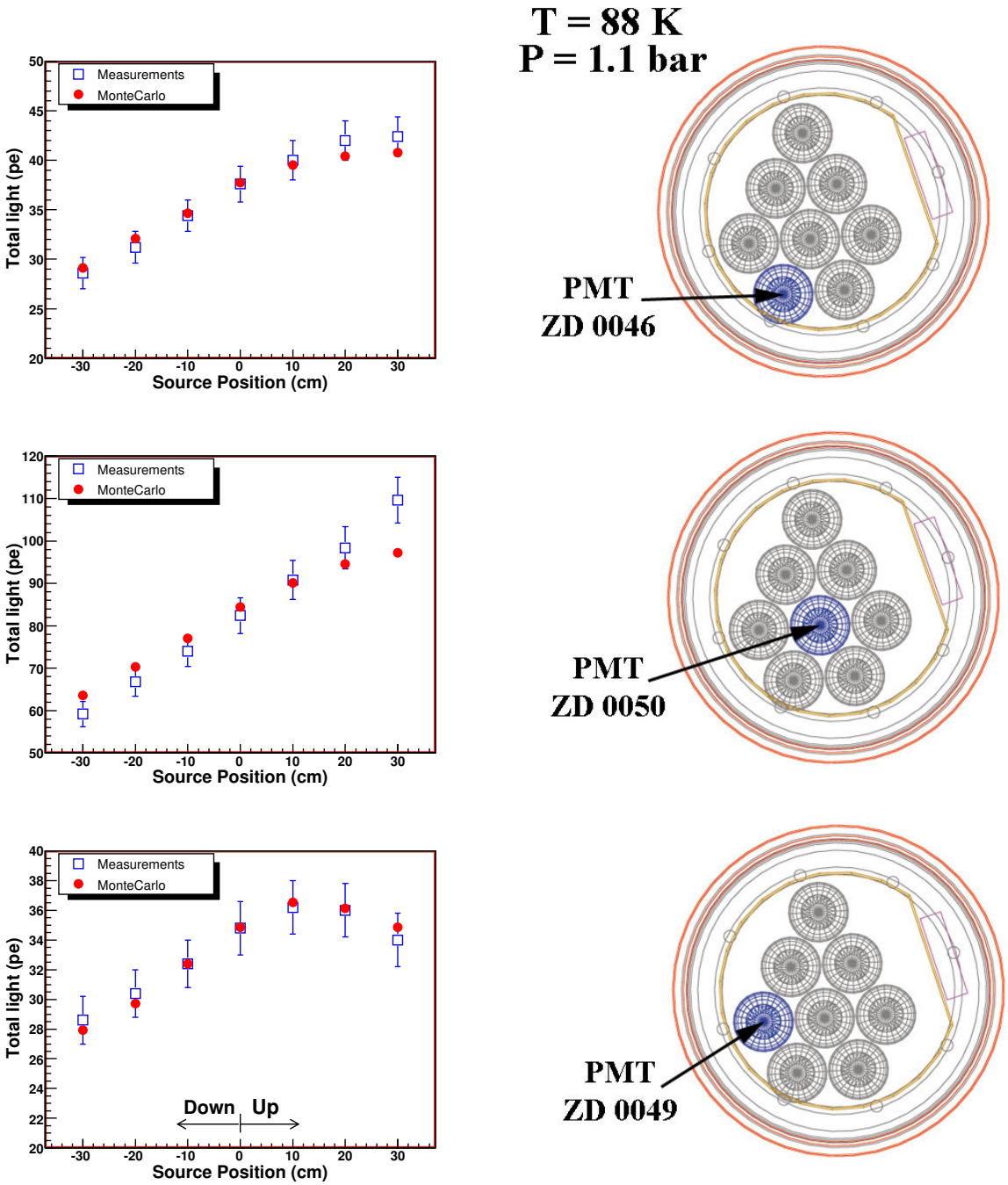

Figure 2.39: Comparison between experimental measurements in gaseous argon and Monte Carlo for PMTs with serial number ZD0046, ZD0050 and ZD0049. These results correspond to a pressure of 1.1 bar and a temperature of 88 K.

Chapter 3

The ArDM experiment: The Slow Control System

Slow control sensors are crucial to monitor the detector performance during the critical phases of its operation, like the pumping period, the cooling down with LN_2, the filling with LAr and during the warming up [49]. Besides, it is important to monitor permanently the experiment during the data taking phase.

In ArDM, we specifically need to monitor the temperature, pressure and level of LAr. Hence, we use three different kinds of slow control sensors. Some resistors measure the temperature in several positions: inside the target, around the cryostat and also in the cooling system. Pressure gauges measure the argon and the nitrogen pressure and the level meters measure the level of LAr. All data are read by a dedicated computer in a cycle of about twenty seconds and stored in a database.

In what follows, we describe in detail each component of the system: namely temperature, level and pressure gauges.

3.1 Temperature measurement

The inner detector of the ArDM experiment is located inside a cilindrical vessel almost full of LAr (see chapter 2), so it is at cryogenic temperature (∼87 K). Therefore, we need to know the temperature gradient inside this vessel, in a vertical and in a radial way. For this purpose, we use small resistors, placed in different positions of the detector, as temperature gauges.

In this section, we describe these temperature gauges, their calibration at very low temperatures, the precision obtained in experimental measurements in LAr and their installation inside the detector. In addition, we give some details about the electronics used for the right operation of these sensors and the software developed in order to monitor the temperature measurements.

3.1.1 Temperature gauge

Nowadays, the market offers a broad catalogue of temperature sensors. Out of the available models, we have chosen small platinum resistors because we need small sensors, easier to place inside the detector, with long-term stability, resistance against vibration and temperature shocks, measurement accuracy, wide temperature range of operation and simple interchangeability. In particular, we use thin-film resistor from IST AG [50], type P10K.520.4W.Y.010 (see figure 3.1),

since, among the platinum resistors, they have the highest sensitivity and we pretend to reach a precision better than 0.5 K. These sensors are resistors of 10 KΩ at 0 °C, so, in what follows, we refer to them as Pt10K sensors.

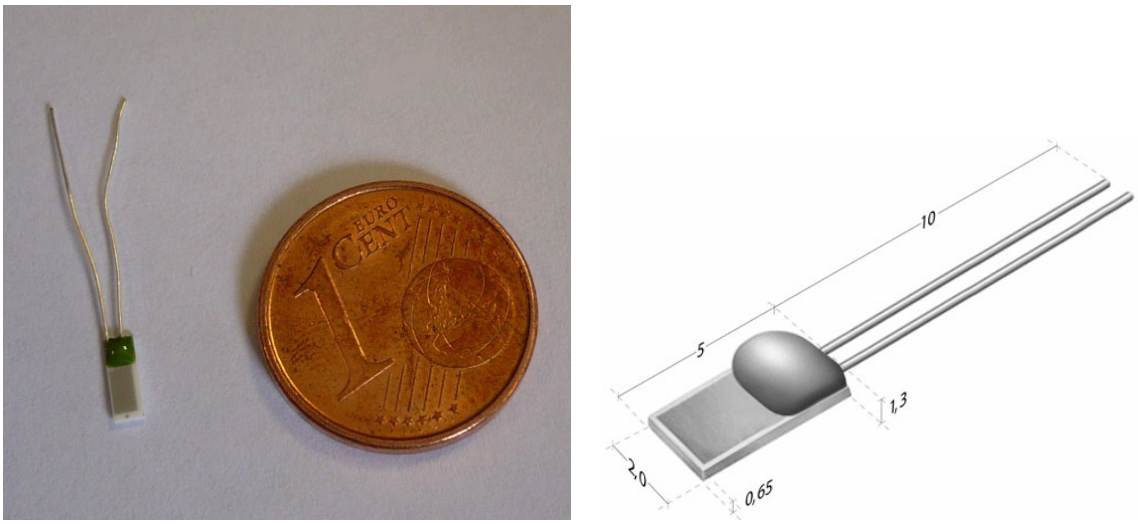

Figure 3.1: Left: Pt10K temperature sensor. Right: Dimensions of a Pt10K sensor in mm.

Pt10K sensors are platinum-surface mounted resistors with dimensions 5 mm×2 mm×0.65 mm (see figure 3.1). They show temperature dependent resistance. Hence, the local temperature in a given position is obtained by measuring the voltage drop across the Pt10K sensor when a current of 100 μA flows through it.

The manufacturer supplies the following definition of the temperature curve for Pt10K sensors, according to the DIN EN 60751 standard[1]:

$$R_{manufacturer}(t[^\circ\mathrm{C}]) = R_0(1 + At + Bt^2 + C[t - 100]t^3) \tag{3.1}$$

for a temperature range from -200 to 0 °C, and

$$R_{manufacturer}(t[^\circ\mathrm{C}]) = R_0(1 + At + Bt^2) \tag{3.2}$$

for a range from 0 to 400 °C, where:
$R_0 = 10000\ \Omega$ (resistance value in ohms at 0 °C),
$A = 3.9083 \times 10^{-3}\ ^\circ\mathrm{C}^{-1}$,
$B = -5.775 \times 10^{-7}\ ^\circ\mathrm{C}^{-2}$,
$C = -4.183 \times 10^{-12}\ ^\circ\mathrm{C}^{-4}$,
t = temperature in accordance with ITS-90[2].

In addition, for this type of sensors, the manufacturer applies a tolerance of $\pm 0.10 + 0.0017\ |T|$ ($|T|$ is the numerical value of the temperature in °C without taking into account either negative or positive signs).

[1] DIN, *Deutsches Institut fur Normung*, is the German national organization for standardization and DIN EN is used for the German edition of European standards.

[2] ITS-90, the International Temperature Scale of 1990, is an equipment calibration standard for making measurements on the Kelvin and Celsius temperatures scales.

Since we use Pt10K sensors to measure the temperature at different locations of the ArDM detector, first of all, we tested these resistors at our cryogenic laboratory in order to know if, at LAr temperature, their behaviour matches the temperature curve supplied by the manufacturer. We show in the following section that, actually, the manufacturer polynomial at very low temperatures (equation 3.1) can not be used, so finally we had to calibrate the Pt10K sensors.

3.1.2 Calibration of Pt10K sensors at very low temperatures

In this section, we describe the tests carried out for the calibration of the Pt10K sensors at very low temperatures. First, we measured some resistors at different temperatures and compared the measurements with the values given by the manufacturer polynomial.

We measured five resistors at the following temperatures: 76.9 K (LN_2), 86.9 K (LAr, the boiling point at 1 atm is 87.3 K) and 273.6 K (ice-water mixture). The measurements were taken in an open dewar at a barometric pressure of 960 mbar and the sensors were fastened to a copper plate (see figure 3.2). The results are summarized in table 3.1.

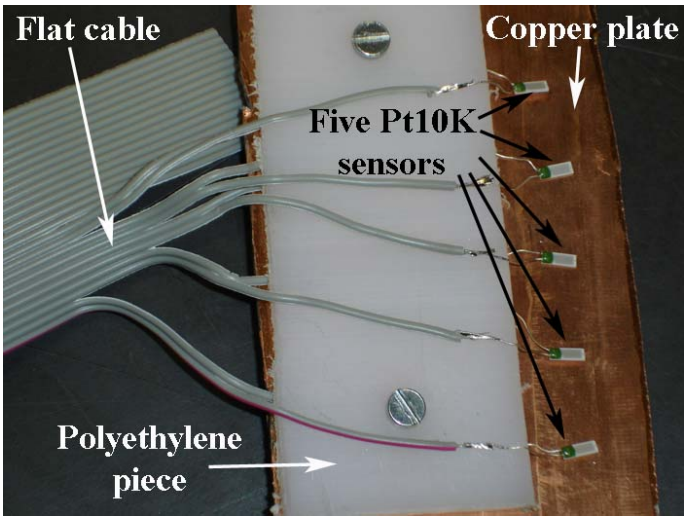

Figure 3.2: Setup for the calibration of the Pt10K. The main copper plate is clearly visible. Pt10K sensors are also distinguishable.

	R_{nom} (Ω)	S_1	S_2	S_3	S_4	S_5
LN_2	2014 ± 19	1978 ± 5	1972 ± 2	1974.7 ± 1.9	1973.8 ± 1.8	1974.7 ± 1.8
LAr	2443 ± 18	2412 ± 5	2408 ± 2	2407.0 ± 1.8	2410.0 ± 1.9	2410.0 ± 1.9
Ice-water mixture	10016 ± 4	10017 ± 9	10020 ± 3	10018 ± 2	10019 ± 2	10015.8 ± 1.7

Table 3.1: Measured resistance values S_n in Ω of the first batch of five Pt10K sensors at LN_2, LAr and ice-water mixture temperatures. The nominal resistance expected from the manufacturer polynomial dependence is also shown.

As we show in table 3.1, all sensors give consistent results. On one hand, for the case of very low temperatures, the measured average value is 2408.8±0.9 Ω for LAr and 1974.0±0.9 Ω for LN_2 temperature. However, the nominal values, as given by the manufacturer polynomial (equation 3.1), are 2443±18 Ω for LAr temperature and 2014±19 Ω for LN_2 temperature. Hence, the measured resistances are systematically lower by about 34 to 40 Ω than predicted by the polynomial (see figure 3.3). These differences in resistance are equivalent to about $0.8 - 0.9$ °C in temperature.

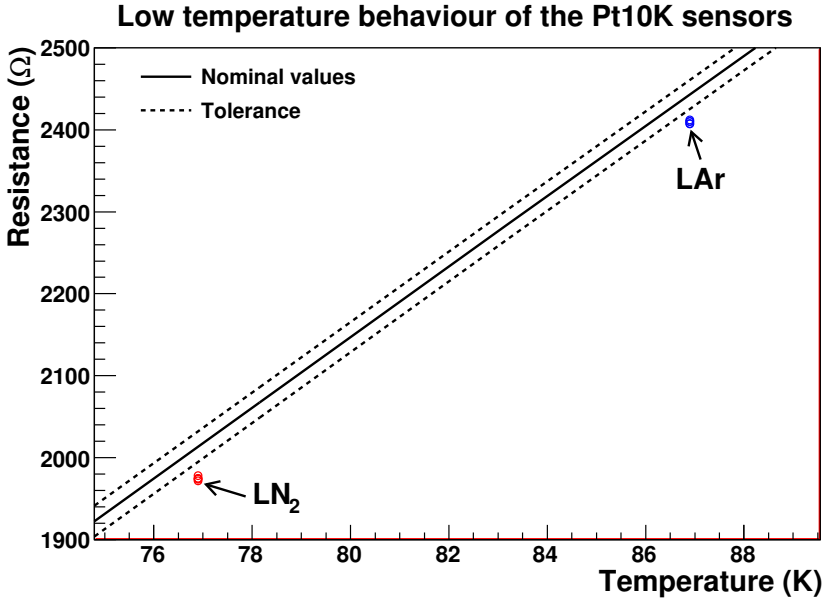

Figure 3.3: Measured resistances of the Pt10K sensors in LN_2 and LAr compared with the nominal polynomial dependence given by the manufacturer.

On the other hand, for the ice-water mixture (temperature of 0.4 °C), we obtain that the measured average value is 10017.7±1.0 Ω and the resistance given by the manufacturer polynomial is 10016±4 Ω. Hence, we find the measured resistances lie within the tolerance range (see figure 3.4).

Regarding the test results, we realized that the lower temperature the worse the manufacturer polynomial matches the experimental measurements. Therefore, the origin of the discrepancy in figure 3.3 was only due to an operation outside the range of validity and **we must calibrate the Pt10K sensors at very low temperatures**.

In order to find a polynomial that fits the measurements better than the one of equation 3.2, we have used the experimental measurements taken in the previous test (see table 3.1). We have adjusted the constant term to 10014.3 Ω at 0 °C (from the measurements of a precise resistance of 10 KΩ) and changed the coefficient of the linear term A to match the data at very low temperatures. To fit this coefficient, we have used the measured values at LAr and LN_2 temperatures, in order to have a higher range of application, since ArDM experiment works at these cryogenic temperatures (see figure 3.5). We have not modified the small coefficients B and C. The **corrected polynomial** is:

$$R_{corrected}(t[^\circ\mathrm{C}]) = R_0(1.00143 + At + Bt^2 + C[t - 100]t^3), \tag{3.3}$$

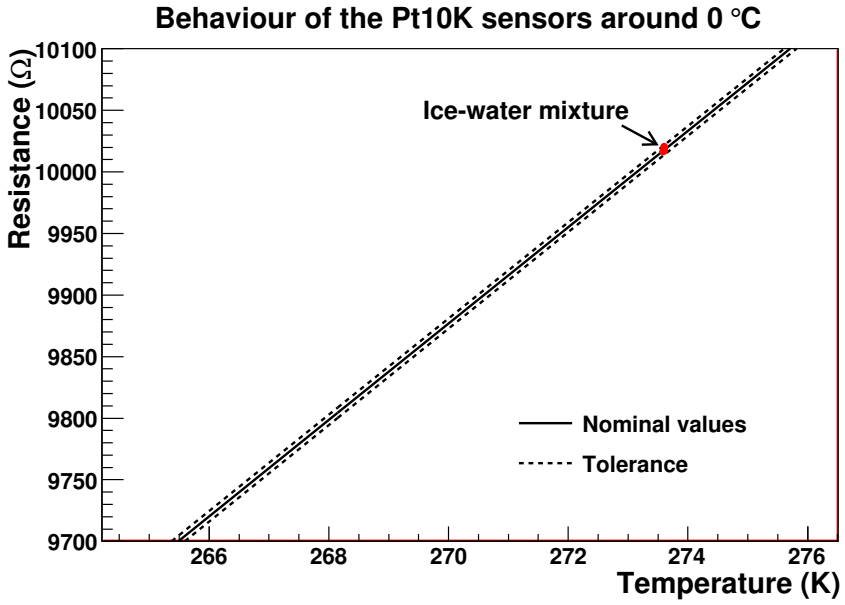

Figure 3.4: Measured resistance of the Pt10K sensors in ice-water mixture compared with the nominal polynomial dependence given by the manufacturer. The measured points are within the tolerance.

where
$R_0 = 10000\ \Omega$,
$A = 3.9348 \times 10^{-3}\ ^\circ\mathrm{C}^{-1}$,
$B = -5.775 \times 10^{-7}\ ^\circ\mathrm{C}^{-2}$,
$C = -4.183 \times 10^{-12}\ ^\circ\mathrm{C}^{-4}$.

In figure 3.6, we show the resistance as a function of the temperature over the whole temperature range, calculated with the adjusted parameters, and the measured resistances. The characteristic polynomial given by the manufacturer yielded higher values for the resistance at low temperatures, however, a good description of the temperature behaviour over the interest temperature range (mainly LAr temperature) is obtained with the fitted polynomial (equation 3.3).

Therefore, we have already obtained a fitted polynomial which matches the measured resistances. Now, our interest pursues to assessing the precision offered by the Pt10K sensors when operated with the final electronics. To this end, we have made a test at LAr temperature. Since we actually measure resistances, we use the fitted polynomial, previously discussed, to obtain the temperature value which corresponds to the resistance one.

Figure 3.7 shows the setup used in this test: the electronic box for the temperature sensors, the computer with our slow control program installed to monitor the temperature measurements and save them in a file, a dewar full of LAr and a flat cable that connects one end to the electronic box and the other to the Pt10K sensors fastened to a copper plate. We have measured twenty sensors in three batches (A0-A4, B0-B4, C0-C9) at a LAr temperature of 86.9 K (see table 3.2).

Figure 3.8 shows the dispersion of measurements for the twenty sensors at a fixed temperature of 86.9K. The average resistance is 2408.6±0.4 Ω, corresponding to a temperature of 86.915±0.009 K. In addition, regarding the table 3.2, we notice that the largest measured deviation from the mean

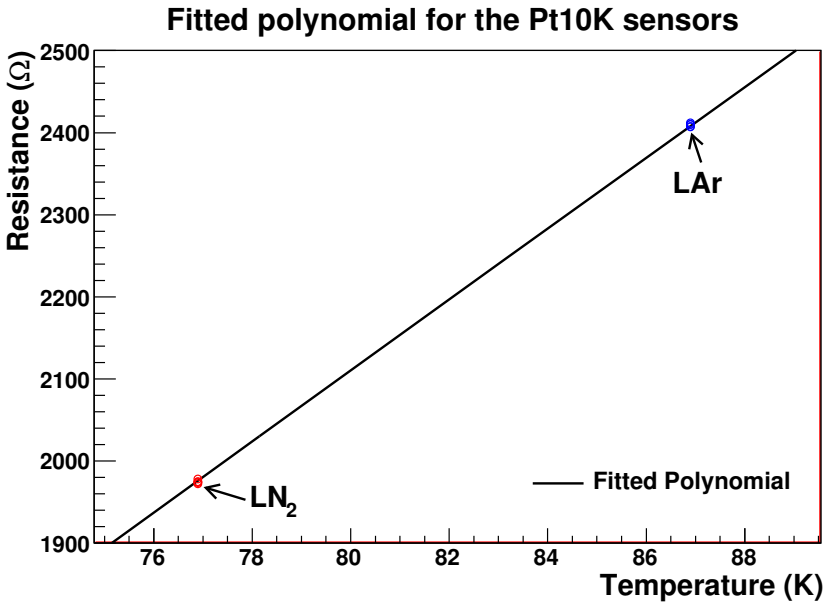

Figure 3.5: Result of the fit to the measured resistance of the Pt10K sensors (see text for details).

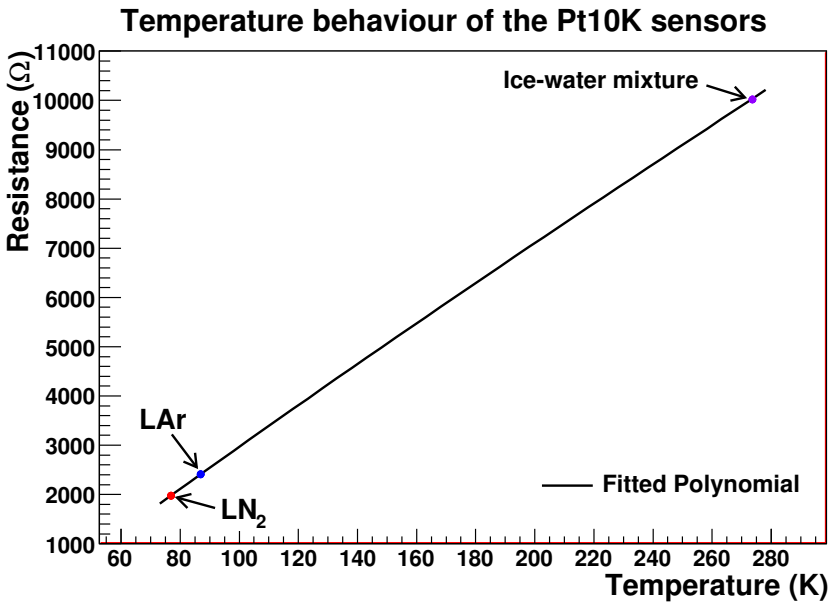

Figure 3.6: Measured resistances of the Pt10K sensors compared to the fitted polynomial dependence over the full range of measured temperatures.

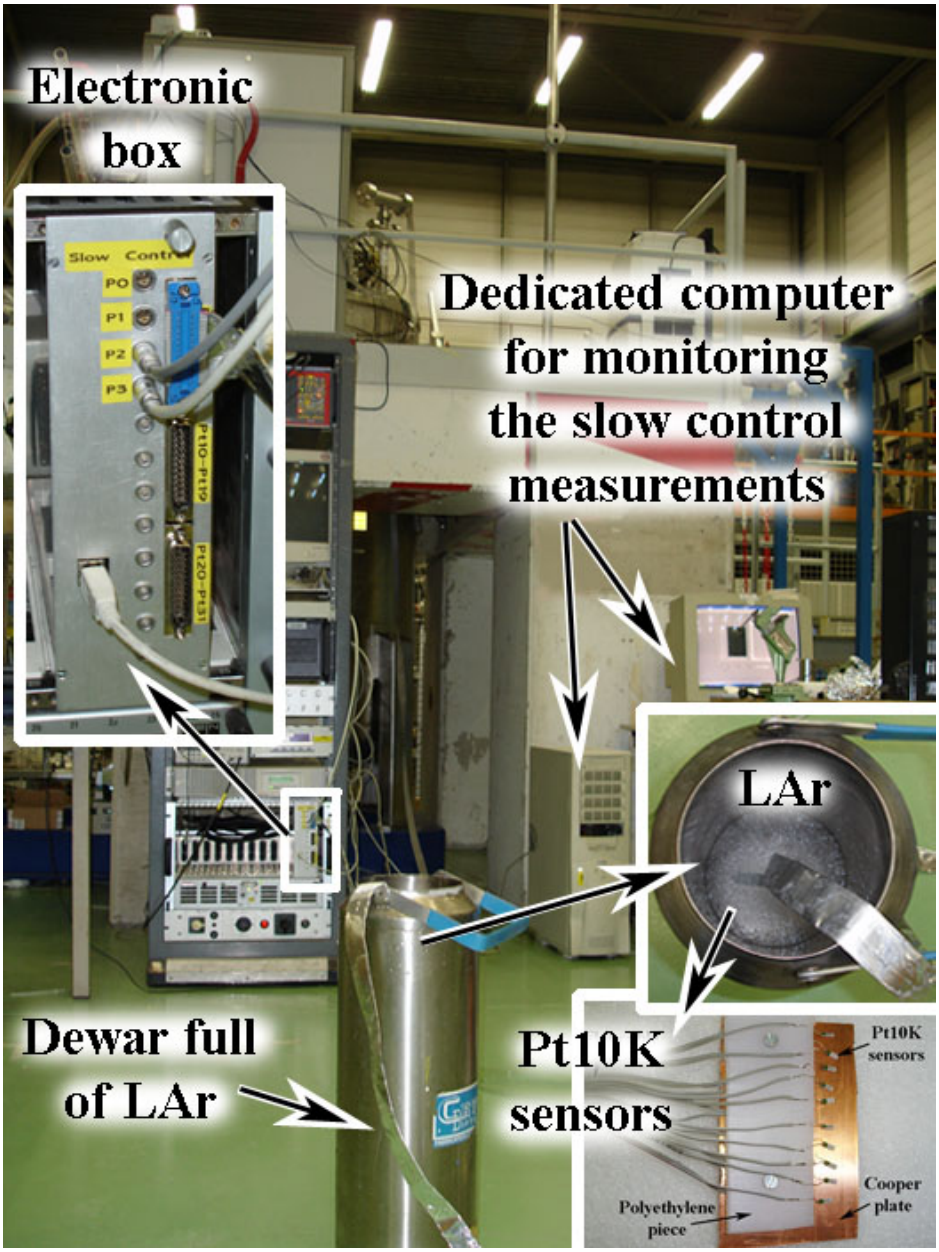

Figure 3.7: Setup used for the Pt10K tests.

Sensor	Resistance (Ω)	Temperature (K)
A0	2415 ± 3	87.05 ± 0.08
A1	2410.5 ± 1.7	86.96 ± 0.04
A2	2409.4 ± 1.6	86.93 ± 0.04
A3	2412.3 ± 1.3	87.00 ± 0.03
A4	2411.9 ± 1.5	86.99 ± 0.03
B0	2408 ± 3	86.89 ± 0.08
B1	2409 ± 3	86.93 ± 0.07
B2	2406 ± 2	86.84 ± 0.05
B3	2408 ± 3	86.90 ± 0.06
B4	2406 ± 2	86.86 ± 0.05
C0	2409 ± 4	86.92 ± 0.10
C1	2410 ± 2	86.95 ± 0.05
C2	2407.8 ± 1.7	86.89 ± 0.04
C3	2405.6 ± 1.6	86.84 ± 0.04
C4	2405.3 ± 1.5	86.84 ± 0.04
C5	2408.1 ± 1.6	86.90 ± 0.04
C6	2406.9 ± 1.2	86.87 ± 0.03
C7	2410.5 ± 1.6	86.96 ± 0.04
C8	2406.1 ± 1.4	86.86 ± 0.03
C9	2409.1 ± 1.7	86.92 ± 0.04

Table 3.2: Measured resistance values (Ω) of the three batches (A0-A4, B0-B4, C0-C10) of Pt10K sensors at LAr temperature. The third column shows the corresponding temperature values (K) obtained from the fitted polynomial (equation 3.3).

is ∼6 Ω (sensor A0), corresponding to 0.14 K. Considering all the sensors, we obtain an average deviation of about 0.05 K. On the other hand, the uncertainties for the temperature values are less than 0.1 K. Therefore, through this test we get that the **precision in temperature is very good, better than 0.5 K**. That is enough to match our experimental requirements.

We have made some tests to assess the behaviour of the Pt10K after going through several LAr to room temperature cycles. To this end, we have exposed twenty Pt10K sensors to fifteen temperature cycles. Then, we have compared the measured temperature using these sensors with the value given by new sensors. At LAr temperature, the difference between temperature measurements given by new Pt10K sensors and those measured by the sensors with fifteen temperature-cycling is very small, about 2 Ω, that is ≈0.05 K. Hence, it appears that the **temperature cycling does not affect the behaviour of the sensors**.

3.1.3 Installation of Pt10K sensors inside the ArDM vessel

Once we have calibrated the Pt10K sensors, we installed them inside the detector. The ArDM detector operates with thirty-two Pt10K sensors, because that is the number of input channels for temperature sensors in our electronic box (namely Pt0 to Pt31), enough for our requirements. We opted for locating twenty sensors inside the vessel (corresponding to the input channels Pt0 to Pt19) and ten sensors outside, around the dewar and inside the cryogenic system (channels Pt20 to Pt29). An additional sensor is placed on the plate of the electronic box for the temperature sensors in order to monitor the temperature when the NIM crate is on. It is useful in case there is

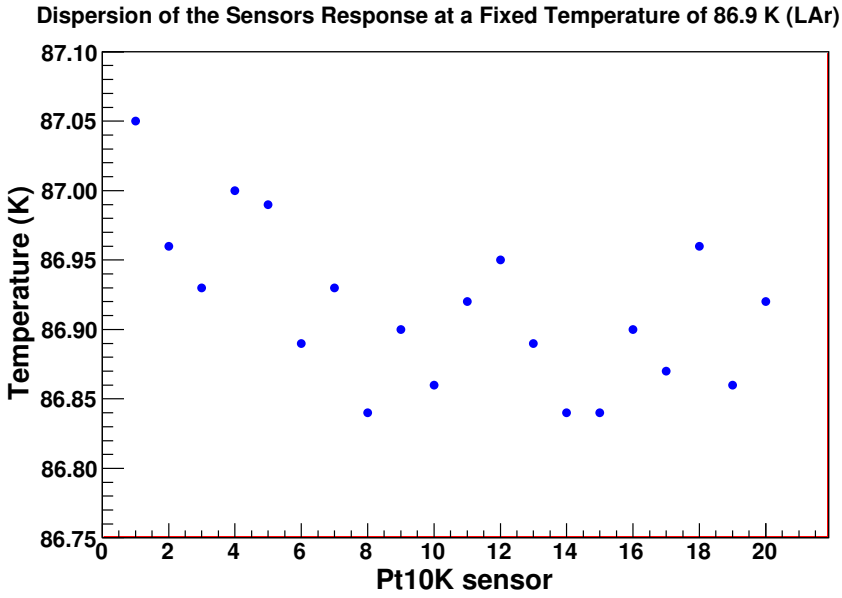

Figure 3.8: Dispersion of measurements for the twenty sensors to be used for the ArDM detector.

a sudden increase of the temperature inside the electronic box. The last sensor (channel Pt31) is a resistance of 10 KΩ, used as reference in the calibration.

We install twenty sensors into the inner vessel in order to control the temperature gradient from top to bottom and from the outside to the inside. Ten of these Pt10K sensors have already been installed in a vertical column (see figure 3.9) and the other ten sensors will be placed around the LEM support. This support is currently being assembled, so they could be mounted for the first tests of the prototype.

The ten installed sensors are used to monitor the temperature gradient along a vertical axis and as discrete level meters during the filling with LAr. We have used a rectangular piece of polyethylene of 1500 mm × 55 mm, placed on one of the detector pillars, as support for the cable and the Pt10K sensors. However, since the pillars are the support for the field shaping rings, we must separate this Pt10K support from the pillar to avoid discharges. Hence, we have fastened the Pt10K support to the pillar through plastic sticks, nuts and screws (see figure 3.10) allowing a separation of 4 cm between both of them. This distance places the Pt10K sensors close to the wall of the inner vessel and away enough from the field shapers.

Figure 3.11 shows a sketch of the positions of these ten sensors. We have placed the uppermost temperature sensor at 26.2 cm from the top flange, close to the LEM position, and the last one near the PMT surface. The vertical distance between two consecutive sensors is 4.5 cm for the top ones and 21.7 cm for the rest of them. The separation between the four upper ones is smaller because the LEM will be placed in this region and we must monitor with better granularity the temperature around it.

We have used a flat cable[3] to transfer the signal from the temperature sensors to the feedthrough, placed at the top flange. In fact, two feedthroughs[4] (see figures 3.12 and 3.13), each one for ten Pt10K sensors, have been mounted to allow the signal lines of temperature sensors to go through

[3]Cable HV/ 25-way connector, from CABURN.
[4]Multi-pin feedthrough, 25 pins on a DN63CF flange, from CABURN-MDC Europe[51].

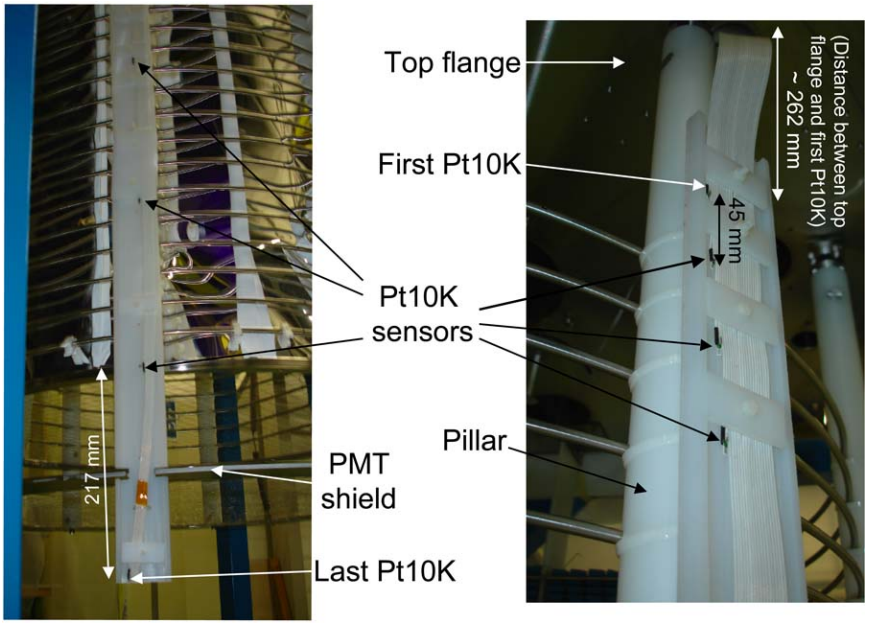

Figure 3.9: Views of some Pt10K sensors installed inside the dewar.

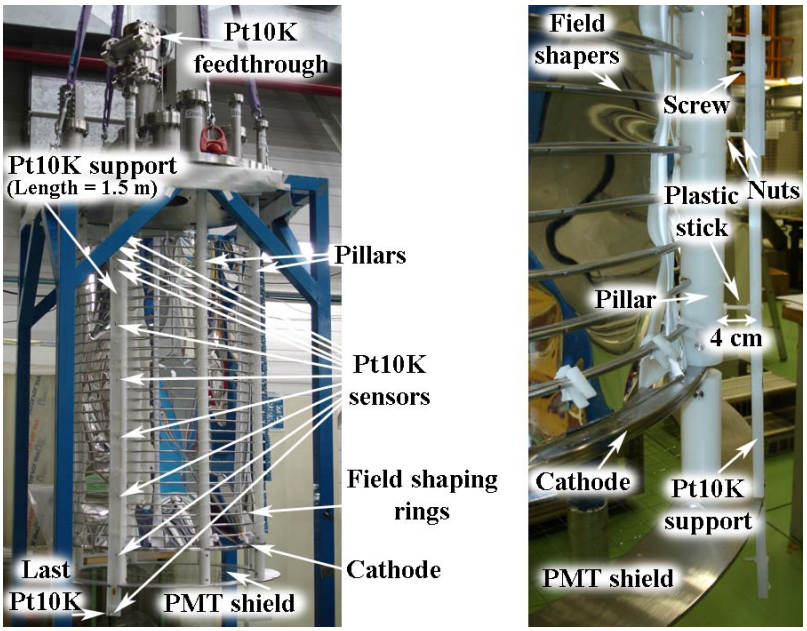

Figure 3.10: Left: Polyethylene support with the Pt10Ks installed. It is fastened to a pillar. Right: View of the pillar and the support of Pt10K sensors where the separation between them is visible.

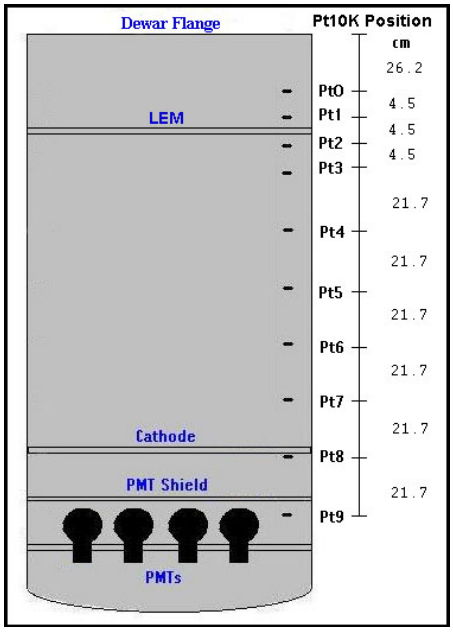

Figure 3.11: Sketch of the positions of temperature sensors.

the top flange of the ArDM dewar up to the electronic box. This is placed in the NIM crate and connected to a dedicated computer to monitor the measurements of the slow control devices. While welding the temperature sensors to the flat cable, care must be taken in order to avoid that the two connections of the Pt10K touch each other. For this purpose, we have cut them and we have covered one of the connections with a small plastic tube (see figure 3.14). We have also set loose all the Pt10K sensors to favour their contact with LAr. Moreover, we have checked the sensors work properly after installation into the vessel.

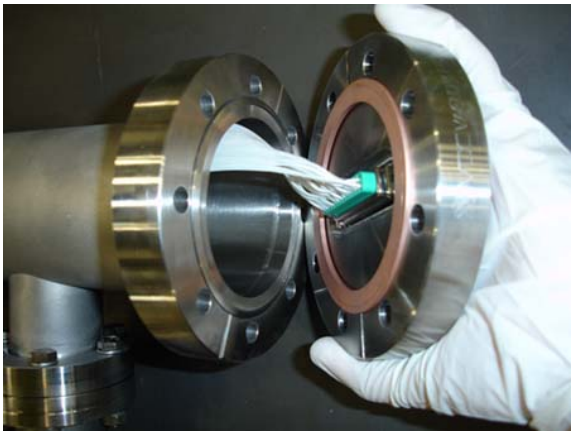

Figure 3.12: Flange with connectors used as feedthrough during installation. Cables going to the Pt10K sensors are visible.

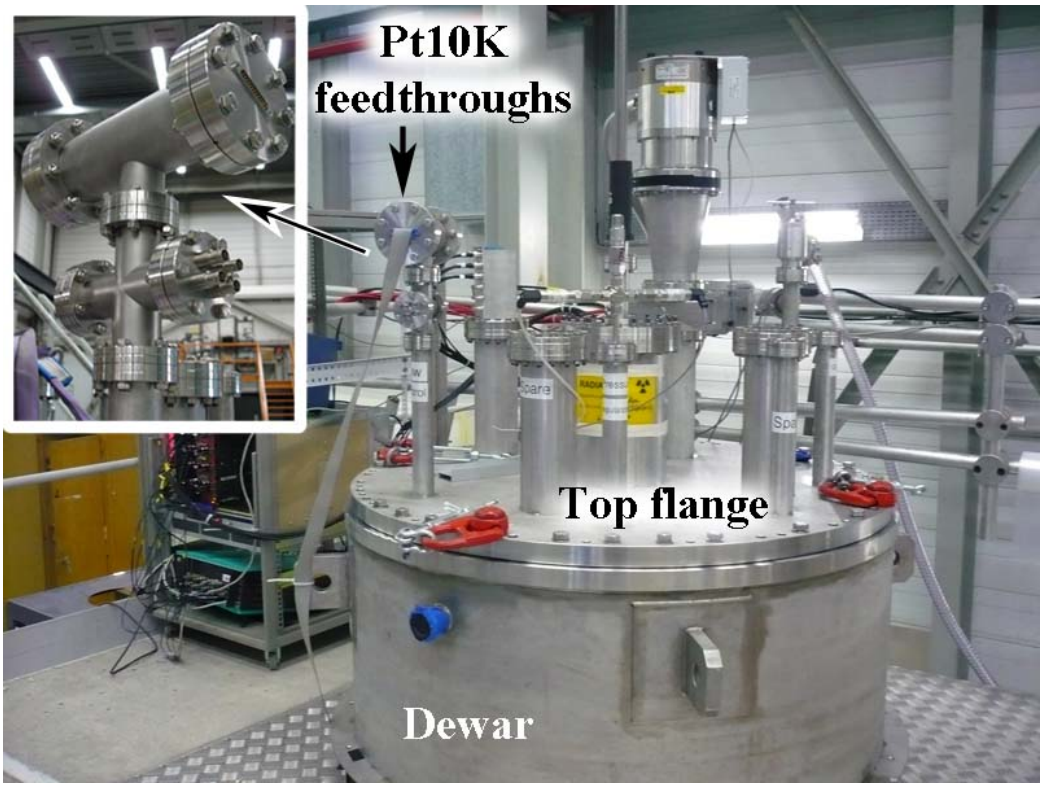

Figure 3.13: Feedthroughs for temperature sensors have been mounted on the top of the dewar.

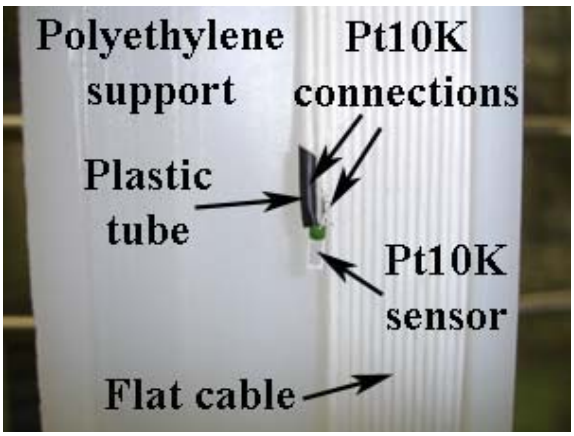

Figure 3.14: View of a Pt10K sensor welded .

3.1.4 Electronics for Pt10K sensors

The analog circuit of the electronics used for the temperature sensors was designed by ETHZ and assembled at our laboratory in Granada (see figure 3.15). We have used a soldering station METCAL [52], model MX-500P-21.

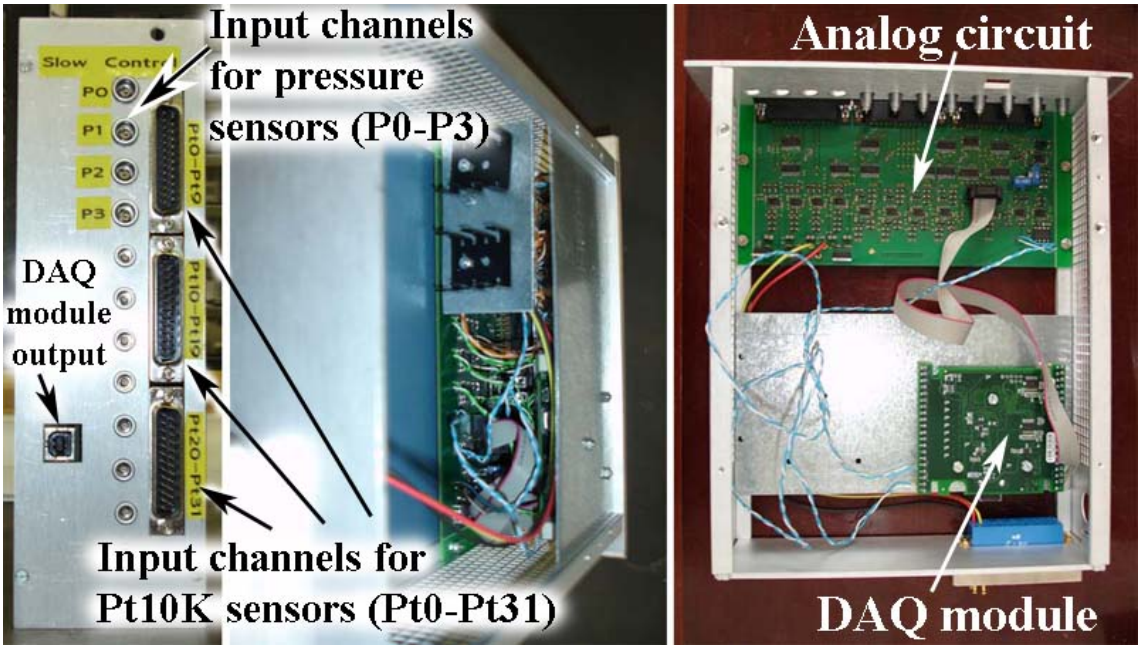

Figure 3.15: Electronic circuits for temperature sensors, assembled in Granada laboratory. The electronic plate inside the box includes the electronics used for both, temperature and pressure gauges.

The electronics used for operating the temperature sensors is as follows. As we previously mentioned, we use a Pt10K like temperature sensor, so this involves a variable resistance that is a function of the temperature. Figure 3.16 shows the electronic design for circuit 1. This circuit 1 supplies a constant current of 100 μA. This current flows through the Pt10K and we measure the voltage drop across the temperature sensor. This voltage is one of the input of a CMOS analog multiplexer, type DG408. This multiplexer has 3 bits (A_0, A_1, A_2) that we use to select the Pt10K that we want to measure. The output of the multiplexer will be used as the input for another circuit of the electronics, namely circuit 2 (see figure 3.17). Circuit 2 is a voltage-voltage converter (from the input voltage to a voltage signal between $\pm$5V). We have two different circuits of this type. One of them (channel CH1) is more precise at LAr temperature, so we use this voltage output as input for an A/D converter, type USB-1208LS. It is a USB-based DAQ module with 8 channels of 12-bit analog input, from Measurement Computing [53]. Finally, the output signal from this DAQ module is read by our LabView [54] program for slow control, installed in a dedicated computer.

3.1.5 Software for Pt10K sensors

We have developed a LabView program to monitor the Pt10K measurements. This program reads ADC counts from the DAQ module of the electronics. In a first step, this program calculates the

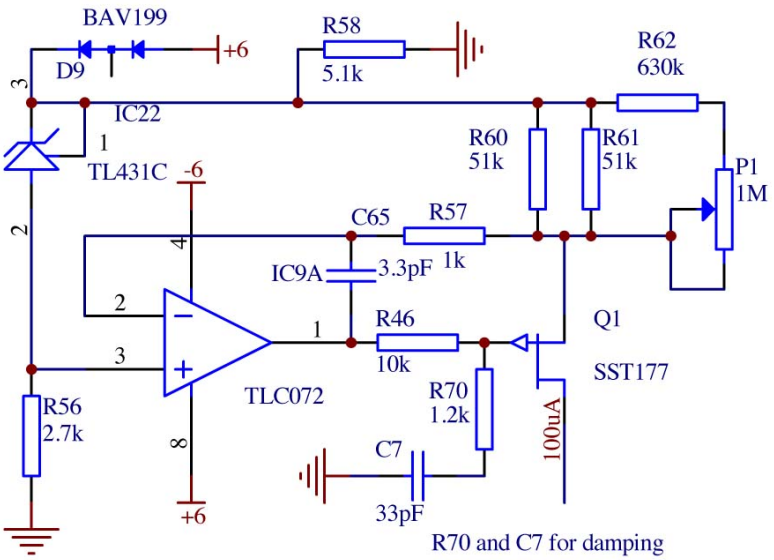

Figure 3.16: Electronic design for temperature sensors: circuit 1 (see text for details).

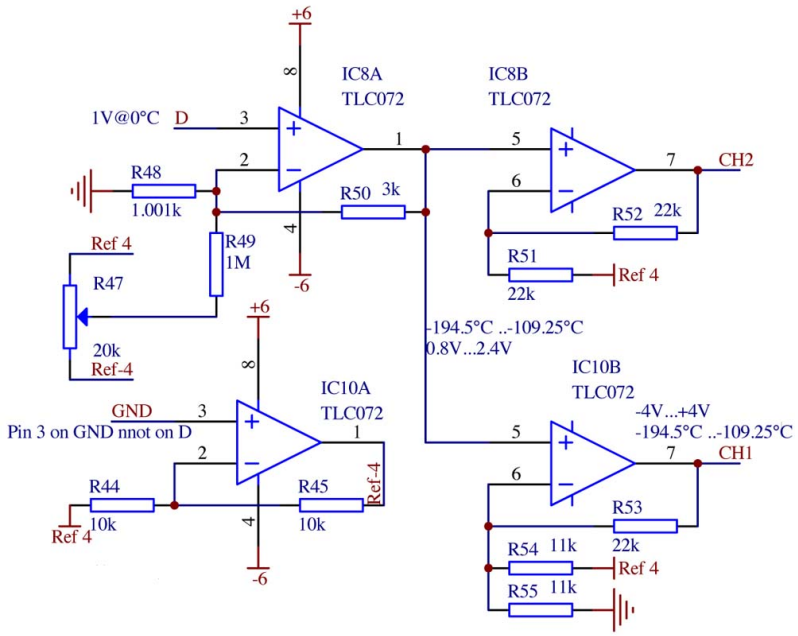

Figure 3.17: Electronic design for temperature sensors: circuit 2 (see text for details).

resistance from the ADC counts. For this purpose, we use the following expression:

$$Resistance(\Omega) = V_{in}/I \tag{3.4}$$

where I = 99.87±0.01 μA (experimental measurement taken with a Fluke-189 [55]).

On the other hand, we calculate V_{in} from an fitted polynomial:

$$V_{in}(V) = (V_{out} \times 0.1249) + 0.5003 \tag{3.5}$$

And V_{out} from the transfer equation:

$$V_{out}(V) = (ADCcount \times 0.0024) - 5 \tag{3.6}$$

Once we know the measured resistance of the Pt10K, we use the fitted polynomial previously obtained in the calibration of these sensors in order to get the temperature value (equation 3.3 in section 3.1.2).

The monitoring for ten Pt10K sensors is shown in figure 3.18. Within the LabView program we have implemented three windows, one for each batch of temperature sensors (Pt0-Pt9, Pt10-Pt19 and Pt20-Pt31). We display the temperature in degrees Kelvin next to the position of each sensor inside the dewar and a graph with the measurements of all sensors in the batch, in real time, using different colour lines for each sensor. These values are instantaneous measurements of the temperature. In addition, the ADC counts are saved in a database every 20 s (we can modify this time at will).

3.2 LAr level measurement

We must measure the level of LAr inside the ArDM dewar to monitor the quantity of liquid poured during the filling and to monitor the level during the data taking phase. In this section, we describe the level gauges used in our experiment, their assembly, calibration at LAr temperature and precision. We also mention some details about the electronics used for theses gauges and the software that we have developed to monitor the level measurements.

3.2.1 Level gauge

Level meters measure the LAr level inside the vessel. These sensors are capacitors partially immersed in the liquid. Since the dielectric constant of liquid and gas argon are different, the capacity changes linearly with the area immersed in the liquid. The dielectric constant of LAr is 1.520 and for the gas it can be considered as 1. This means that a variation of 52% for LAr is expected between the empty and the filled states.

There are two different types of capacity meters:

- A cylindrical capacitor which has the advantage to be insensitive to the changes in the temperature (mechanical dilatation), but has normally a small capacity, i.e. is less sensitive to level changes.
- A plane capacitor which can be constructed with multiple plates, increasing the capacity and thus the sensitivity.

The ArDM experiment uses plane capacitors, since it is crucial to know very precisely the LAr level. The reason is that *the distance between the LEM and the LAr level must be only 5 mm*, so we have to stop the filling at the right position in order to avoid dangerous discharges. For this

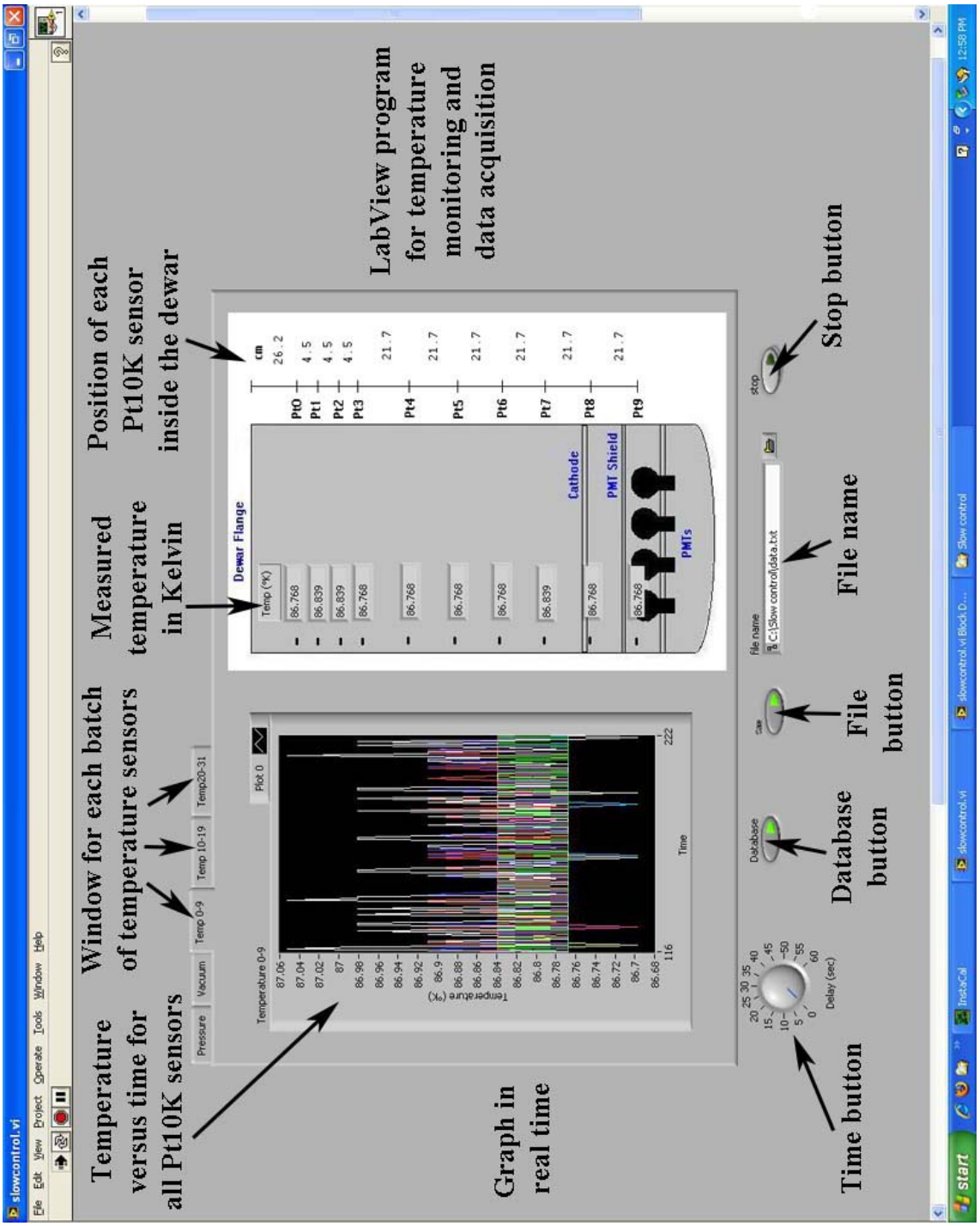

Figure 3.18: Snapshot of the LabView program for temperature monitoring and data acquisition, during a test in LAr. It has been developed by Granada group.

purpose, we install four plane capacitors on the LEM support, near the top flange of the dewar. We use *four level meters* because we need to determine the relative position of the LEM with respect to the surface of LAr, since we want the LEM to be as parallel as possible to LAr surface. In case the LEM is not parallel, we can fix it by moving the experimental holder.

In addition, during the filling, the Pt10K sensors located in a vertical column are used as discrete level meters, since they cover the whole range of interest, from the bottom (PMT surface position) to the top of the argon vessel (LEM position).

3.2.2 Assembly of capacity level meters

We have assembled the four plane capacitors for the ArDM experiment at the Granada laboratory. They consist of ten invar plates with a size of 50×50 mm^2 and two pieces of MACOR of 56×30 mm^2 (see figure 3.19). We mount the metallic plates with a separation of 1.4 mm between consecutive layers, using the MACOR pieces as mechanical support (see figure 3.20). We use plates of nickel iron alloy (invar) because this material has the lowest coefficient of thermal expansion among all metals, about $10^{-6}\,^{\circ}\mathrm{C}^{-1}$, and it is easy to weld. Likewise, we use MACOR as support because this ceramic has a low coefficient of thermal expansion too and is an excellent electrical insulator.

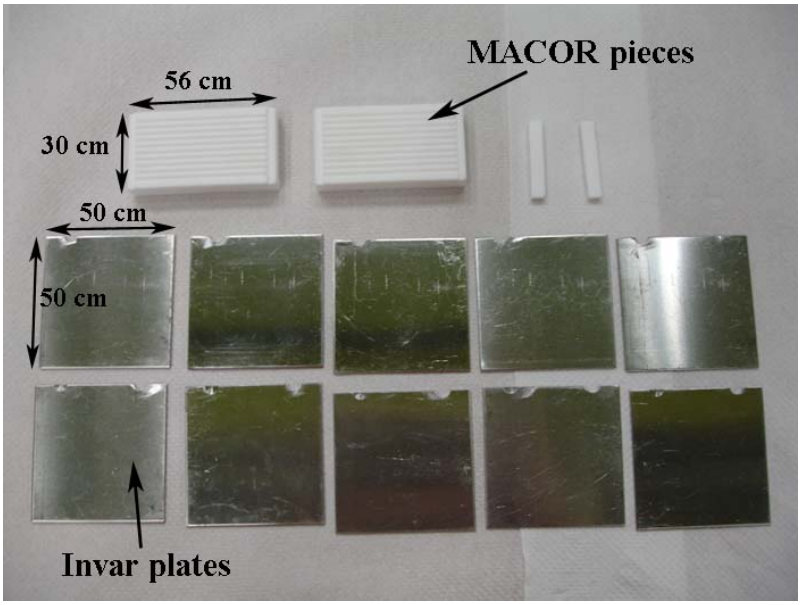

Figure 3.19: Materials used to mount a level meter.

In figure 3.21 we show the feedthrough[5] used for two of the level meters. Since we need four level meters, two of these feedthroughs have been already installed. The coaxial cable used to transfer the level meter signals has a polyimide insulation that do not spoil argon purity. The final installation of the level meters will take place once the LEM is ready for mounting inside the detector.

[5]BNC coaxial feedthrough, 4 pins on a DN40CF flange, from CABURN.

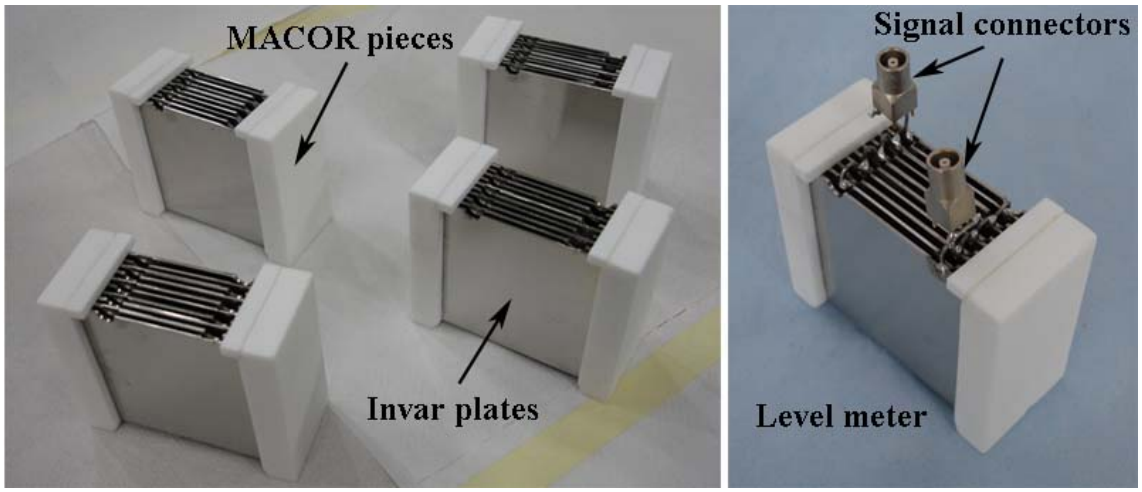

Figure 3.20: Left: Four assembled level meters. Right: Plane capacitor used as level meter. The connectors for transferring the signal are visible.

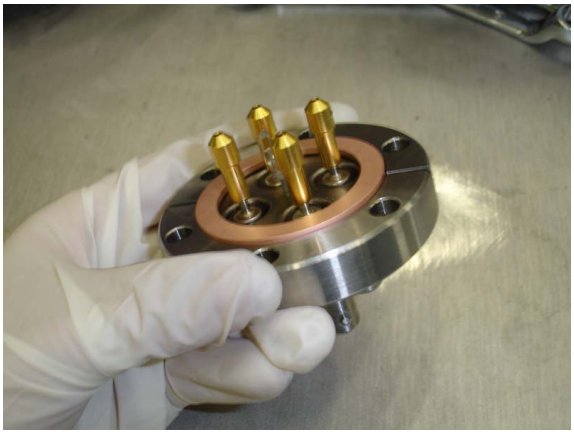

Figure 3.21: Feedthrough used for two of the level meters (each level meter uses two pins).

3.2.3 Calibration of level meters at LAr temperature

We tested the four level meters in LAr several times to study their precision and measurement reproducibility. In figure 3.22 we show the setup used for one of the tests. We placed a level meter inside a small cylindrical vessel (see figure 3.23) and we carried out the following procedure:

1. Pump vacuum inside the vessel.
2. Fill with LAr until the level meter is completely immersed.
3. Let argon to evaporate.

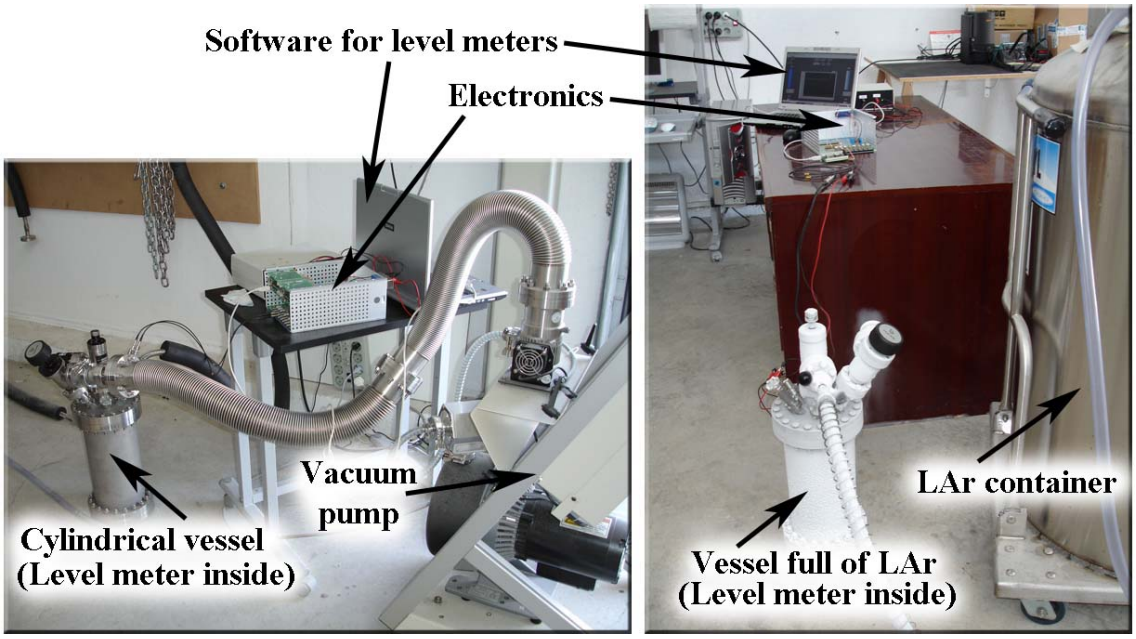

Figure 3.22: Setup used for level meter tests (the level meter is inside the cylindrical vessel). Left: Vacuum pumping. Right: Vessel full of LAr.

We repeat these steps for each of the four level meters, taking capacity measurements every 30 s (see figure 3.24). In addition, several tests are carry out for each level meter to study the reproducibility.

From the electronic circuits of the level meters, we read the ADC counts using our LabView program. The experimental capacity from the ADC counts is given by equation 3.7 (see section 3.2.4).

$$C_x = \frac{4 \times R_2}{R_1 \times R_3} \frac{1}{f} = \frac{1}{10\ \mathrm{M\Omega} \times f} \tag{3.7}$$

where:
C_x = variable capacity (level meter),
R_1 = 4.4 KΩ,
R_2 = 1.1 KΩ,
R_3 = 10 MΩ,

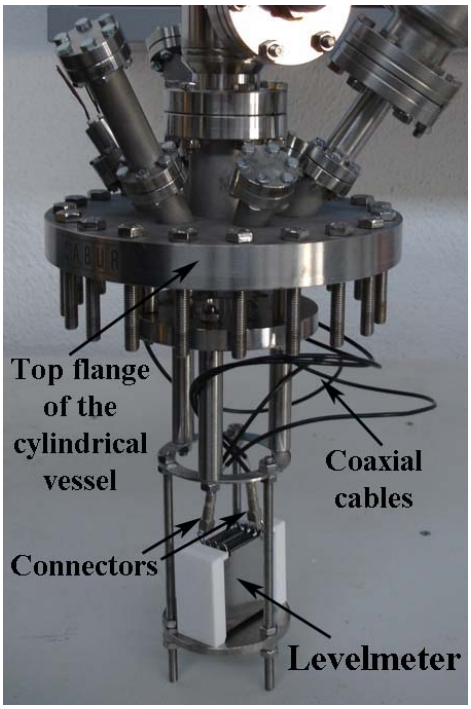

Figure 3.23: Level meter placed inside the cylindrical vessel.

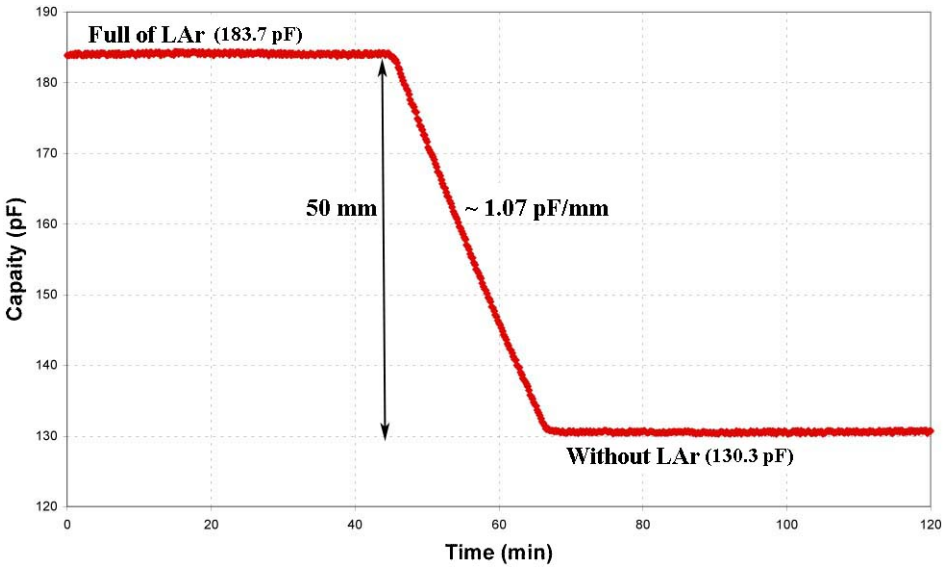

Figure 3.24: Result of a test for a level meter. We represent capacity versus time. At the beginning, the level meter is completely immersed in LAr. The level decreases by evaporation until no liquid is left. Capacity measurements have been taken every 30s.

f = frequency (ADC counts per second).

Once we have measured the capacity, we calculate the LAr level for a capacity meter using the fitted function (see equation 3.8). As we know the location of the LEM inside the inner vessel and the level meter position, we also have the relative distance between the LEM and the LAr surface.

$$\text{LAr level (mm)} = A \times \text{Capacity (pF)} + B \tag{3.8}$$

Where parameters A and B, for each level meter, are shown in table 3.3.

	Level meter 1	Level meter 2	Level meter 3	Level meter 4
A (mm/pF)	$(94012\pm9)10^{-5}$	$(9368\pm11)10^{-4}$	$(9205\pm10)10^{-5}$	$(9456\pm2)10^{-4}$
B (mm)	-123.714±0.014	-122.09±0.17	-117.64±0.16	-123.43±0.03

Table 3.3: Fitted parameters for each level meter. They are used to express LAr level as a function of capacity.

We repeated the test several times for each level meter. After all the tests, we obtained the average capacity when the vessel is full of LAr and empty, the sensitivity to LAr level changes, the precision and the reproducibility. All these results are summarised in table 3.4 for the 4 level meters used.

	Level meter 1	Level meter 2	Level meter 3	Level meter 4
Capacity (pF) when full of LAr	184.78±0.03	183.71±0.04	182.13±0.05	183.40±0.05
Capacity (pF) when empty	131.59±0.03	130.34±0.04	127.81±0.04	130.52±0.03
Sensitivity (pF/mm)	1.064±0.002	1.067±0.002	1.086±0.003	1.058±0.002
Precision (mm)	0.163±0.014	0.181±0.017	0.111±0.010	0.210±0.018
Reproducibility (%)	$(23\pm4)10^{-4}$	$(505\pm5)10^{-4}$	$(511\pm6)10^{-4}$	$(113\pm5)10^{-4}$

Table 3.4: Results of tests for level meters.

Level meters have a sensitivity to LAr level changes of about $1.06-1.09$ pF/mm. **The reached precision is very good, about 0.2 mm**. This is enough to fulfill our requirements (remember that the distance between the LEM and LAr level is 5 mm). In addition, the reproducibility is good too, since the differences among tests for the same level meter are less than 0.1%.

3.2.4 Electronics for level meters

Figure 3.25 shows the electronic scheme used for the capacity meter. From this scheme, we deduce the equation 3.7 mentioned in section 3.2.3. A triangular shape function is injected through the sensor (capacity C_x). Then, the rectangular-shaped current is amplified and measured as an indication of the capacity. In particular, we use an operational amplifier type TLC072. Moreover, this method has the advantage to be insensitive to the capacity of the coaxial cables, which have typically 100 pF/m.

The analog output is sampled by a DAQ device for the level meter. We have used a USB-1024LS module, from Measurement Computing. It is a USB-based, 24 bit digital I/O module. Since we have four level meters, we use four DAQ USB modules in order to work with all level meters at the same time. Figure 3.26 shows the electronic box that we used for the four level meters. The

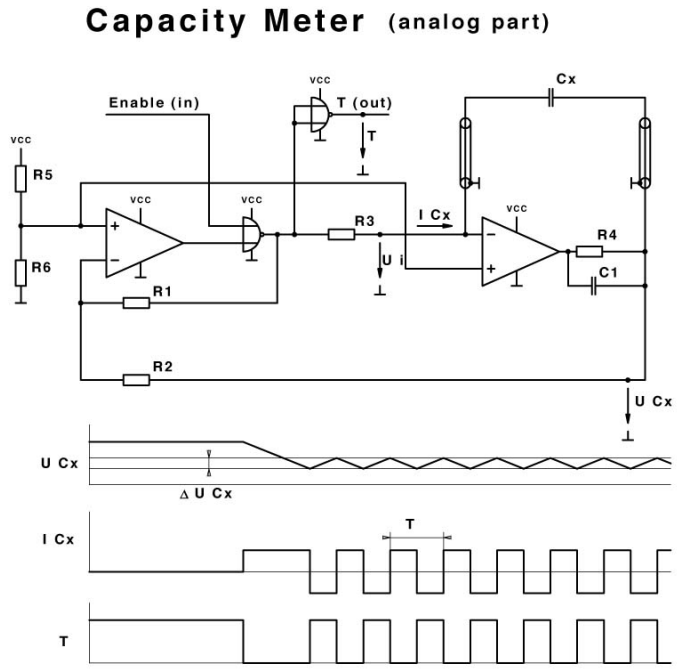

Figure 3.25: Electronic scheme: Analog part for a capacity meter.

output signals from the DAQ modules are read by our LabView program, installed in a dedicated computer.

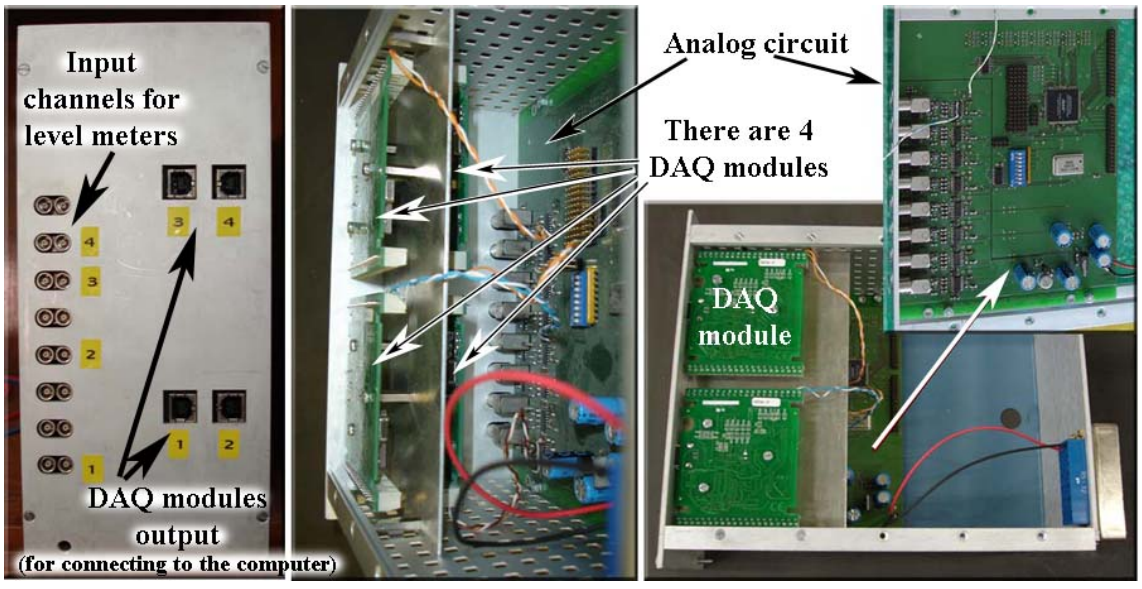

Figure 3.26: Electronic box used for level meters.

3.2.5 Software for level meters

We have developed a LabView program to monitor the measurements of the level meters and to save them into a database. This program reads pulses from the counters in the four DAQ modules. Besides we have implemented equations 3.7 and 3.8 in the software in order to obtain the distance between the LAr level and the LEM from the pulses. These pulses are read every 30 s, so the measurements of LAr level are averages of this time.

Monitoring of the four level meters is shown in figure 3.27. In the graph, we simultaneously represent the LAr level versus time for the four level meters, using different colour lines. We also display the numerical value of the LAr level in mm and four cylinders showing the level for each capacity meter. The cylinders show the volume of level meter full of LAr (grey is empty and blue is full of LAr). Finally, for the sake of improving the security, we add four displays of the range of each level meter with an arrow that points to red level if the LAr amount approaches a dangerous condition.

3.3 Pressure measurement

In our experiment, we use four pressure gauges to measure the pressure in the vessels containing LAr and LN_2. We have already installed two of them in the LAr vessel and the other two sensors will be installed inside the cryogenic system. Using these devices, we can constantly monitor the pressure in the slow-control dedicated computer.

3.3.1 Pressure gauge and its calibration

We use four piezoelectric pressure sensors from Keller Druckmesstechnik [56], type 21S (see figure 3.28). They have been calibrated by the manufacturer and the total accuracy is ±0.5% FS (Full Scale), that is enough for our needs. The output signal of these sensors is a current in the range from 4 to 20 mA, which corresponds to a pressure range from 0 to 2 bars. In figure 3.29 we show the two sensors that we have already installed on the top flange of the LAr vessel. Hence, we use two pressure sensors working in LAr in order to have a spare sensor, in case that one of them breaks down.

We have made some tests with the pressure gauges to assess they work properly and the precision they offer when including our electronic circuits. In particular, to obtain an expression which converts ADC counts into pressure, we make the following test with the electronics. We supply a current of 4 (20) mA in the input of the electronic circuits for pressure gauges and we read the corresponding ADC counts in the output, using a LabView program. Taking into account that 4 (20) mA correspond to 0 (2) bar for these sensors, we calculate the pressure value. As the electronics has four input channels for pressure sensors, we made this test for each channel and the ADC counts obtained were the same for all of them. The result of the test is summarized in table 3.5.

ADC counts	Current (mA)	Pressure (bar)
412	4	0
3686	20	2

Table 3.5: Results of the electronic test for pressure sensors. The obtained values of ADC counts are the same for the four input channels.

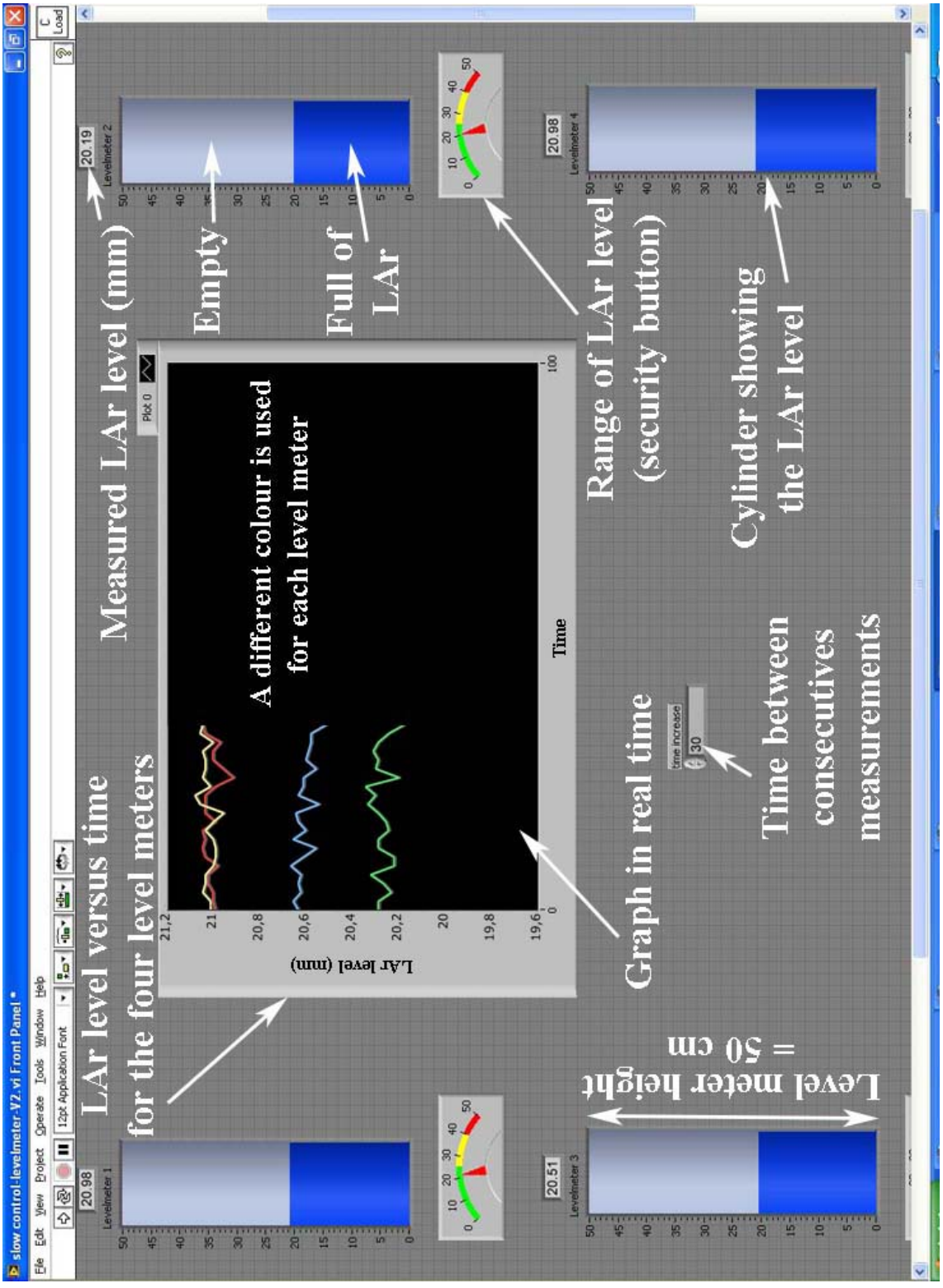

Figure 3.27: LabView program used to monitor the measurements of the four level meters. It has been developed by Granada group.

Figure 3.28: Pressure gauge used in ArDM experiment.

Figure 3.29: Pressure sensors installed on the top flange of the dewar.

Using the values of table 3.5, we obtain the expression for the pressure as a function of the ADC counts (see equation 3.9). This equation is implemented in the LabView program to get the pressure values.

$$\text{Pressure (bar)} = (\text{ADC counts} \times 0.0006) - 0.2517 \tag{3.9}$$

In addition, we made some tests at room temperature inside the dewar, taking data for two different pressure sensors every 20 s for about six hours. The data were taking in two different days and for the four pressure input channels of the electronics. After we analyzed the data, we get that the RMS is about 15 mbar. That is a good enough precision (see figure 3.30). Since the pressure measurements are instantaneous values, we implemented a low-pass filter in the LabView program to reduce the fluctuations.

3.3.2 Electronic circuits for pressure gauges

Figure 3.31 shows the electronic scheme for pressure gauges. This circuit is a converter from current to voltage, that uses an operational amplifier type TLC072. Thus, we convert the current given by the pressure sensor (input of the circuit) from a current range of $4 - 20$ mA to a voltage range of ± 5 V. This voltage is used as input for a CMOS analog multiplexer, type DG408. The four signals of the different pressure sensors are inputs for this multiplexer and we can select the one we want as output using 3 bits (A_0, A_1, A_2). The output of this multiplexer which corresponds to pressure, namely channel CH0, is used as input for an A/D converter USB-1208LS (USB-based DAQ module with 8 channels of 12 bit analog input, from Measurement Computing). Finally, the output signal from this DAQ module is read by a LabView program.

3.3.3 Software for pressure gauges

We have developed a LabView program to monitor the pressure measurements. This program reads ADC counts from the DAQ module and converts them to pressure values using equation 3.9. In the program window, we display simultaneously the measurements of each pressure sensor in the same graph, in real time, using different colours. In addition, ADC counts and pressure values in bars are displayed as well. As in the case of temperature sensors, ADC counts for pressure gauges are saved in a database every 20 s.

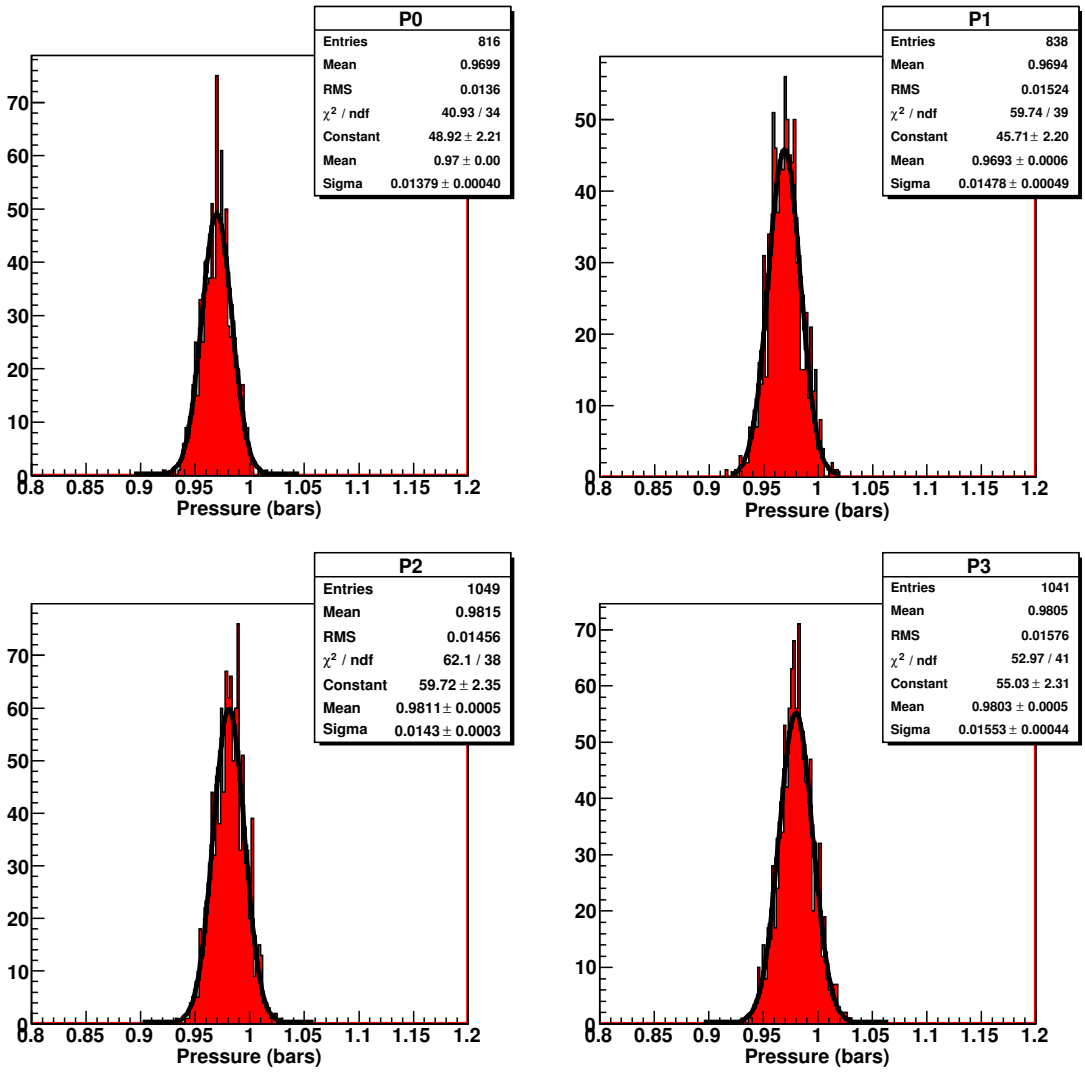

Figure 3.30: Histograms of the input channels of the electronics for the four pressure sensors: channel P0 (top left), channel P1 (top right), channel P2 (bottom left) and channel P3 (bottom right). Data for channels P0 and P1 were taken in a different day to those corresponding to channels P2 and P3.

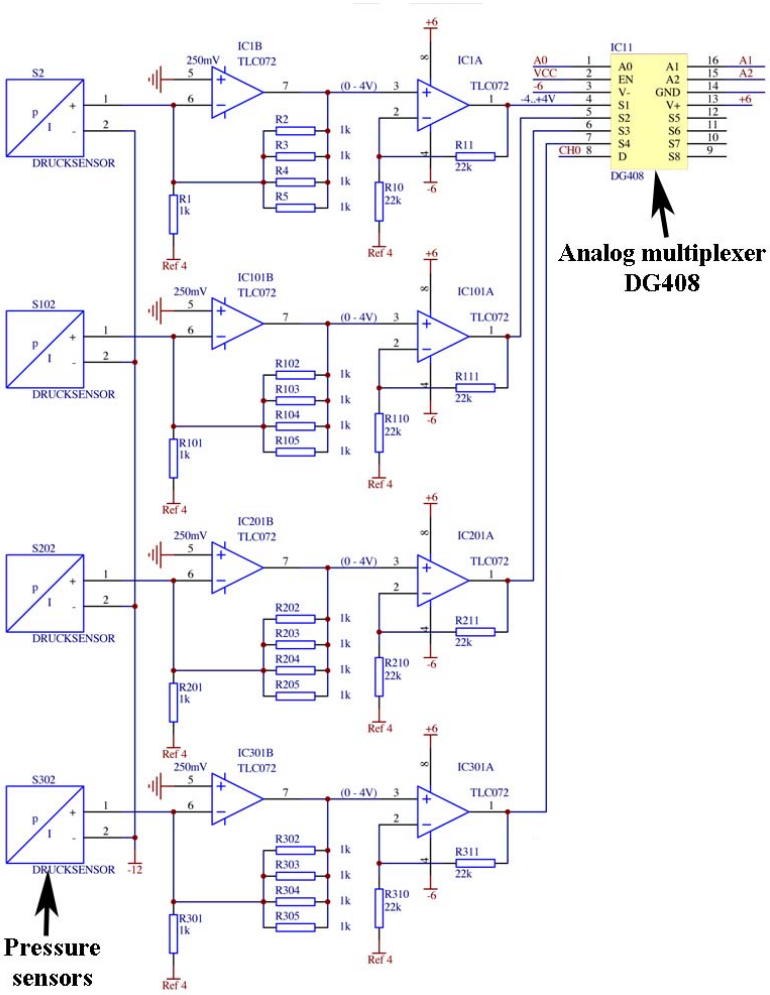

Figure 3.31: Electronic scheme for pressure sensors.

Chapter 4

Physics performance of the ArDM experiment

In our direct search for dark matter, the background sources relevant to our one tonne LAr detector consist mainly of neutrons produced in cosmic muon interactions with surrounding material and neutrons caused by radioactivity in detector components and in surrounding rock, as well as the internal ^{39}Ar background. These background particles could produce nuclear and electron recoils inside the detector. Hence, we have studied them with a detailed GEANT4 simulation of the ArDM detector (see chapter 2 for simulation details). In our case, these backgrounds are addressed with the design of an appropriate shielding as well as with different background rejection potentialities. Among them our experiment relies on event topology recognition, event location, density ionization discrimination and pulse shape discrimination.

In this chapter, we describe the results of our Monte Carlo studies carried out to assess the impact of different backgrounds in the ArDM experiment and the capability of discrimination between them and WIMP signals.

4.1 ^{39}Ar electron background

Commercially available argon is procured by liquefaction of air and contains radioactive isotopes. In particular, an important source of background comes from the presence of radioactive ^{39}Ar. This isotope decays via β-desintegration into ^{39}K with a half-life of 269 years and Q=565 keV (see figure 4.1). Besides, the concentration of ^{39}Ar in atmospheric argon is $(7.9 \pm 0.3) \cdot 10^{-16}$ g/g [57], causing a decay rate of 1 kHz in one tonne of argon [58]. On the other hand, γs from U/Th of the detector components produce an interaction rate which is three orders of magnitude smaller.

Regarding the possibility of misidentifying ^{39}Ar signals as WIMPs, we should note that β particles mainly interact with atomic electrons, while nuclear recoils deposit their energy through transfers to screened nuclei [59, 60]. This affects the charge generated by an event (for the same energy is around three times bigger for electrons), the charge to light ratio, which is bigger for electrons, and the ratio between the fast and the slow components of the scintillation light of LAr (pulse shape discrimination).

Therefore, the rejection of electrons and γ events is facilitated by:

- Light/charge ratio discrimination [61], that uses the fact that the ionization yield of nuclear recoils is highly quenched compared to that of electron/γ, while the scintillation yield is

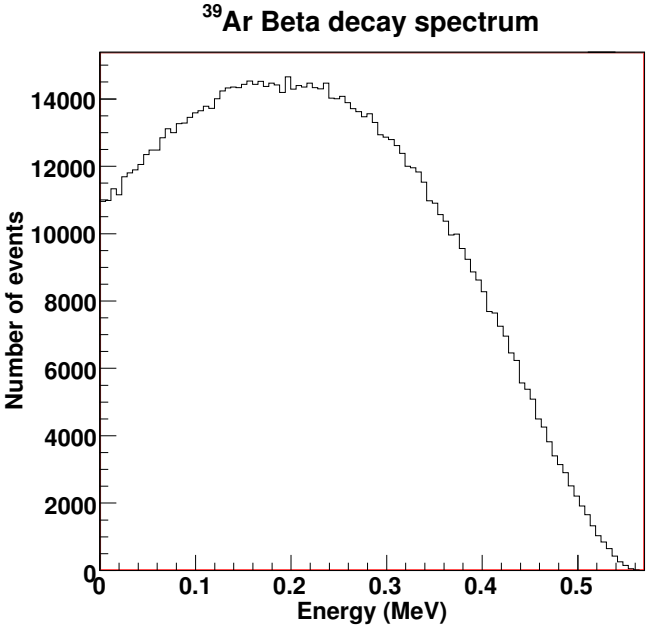

Figure 4.1: ^{39}Ar beta decay spectrum.

similar.

- Pulse shape discrimination [62], whose analysis relies on different populations of the fast and slow components of scintillation.

In order to overcome the internal ^{39}Ar background, a combined rejection power of about 10^{-8} (depending on the WIMP-nucleon cross section) is required, so the light/charge ratio and the scintillation light time distribution must be measured precisely enough.

In addition, an alternative way to reduce the ^{39}Ar contamination is to obtain ^{39}Ar-depleted targets by extracting argon from underground gas wells rather than from the atmosphere [63]. Its ^{39}Ar activity has been recently measured for the first time and shown to be $< 5\%$ of the one present in natural argon. However this background source does not only have negative effects since it is evenly distributed inside the target: it provides precise calibration and monitoring of the detector response as a function of time and position.

4.1.1 Trigger studies

To define precisely what an "event" is, we have carried out previous to our physics analyses, some studies to define a good light trigger for the PMTs. The photomultiplier tube is a photodetector that has an exceptionally fast time response. Then, in a first step, we give a brief description about the PMT working principle and its timing properties.

Figure 4.2 shows the basic structure of a PMT and the basic processes that take place when a PMT is illuminated [41]. An incident photon passes through the *window* of the PMT and reaches the *photocathode* (sensitive part of the PMT), where it may produce an electron. This *photoelectron* is focused by the *focusing electrodes* towards the first dynode and then new electrons are generated in the *dynode chain*, until the *anode* is reached and the final signal is collected.

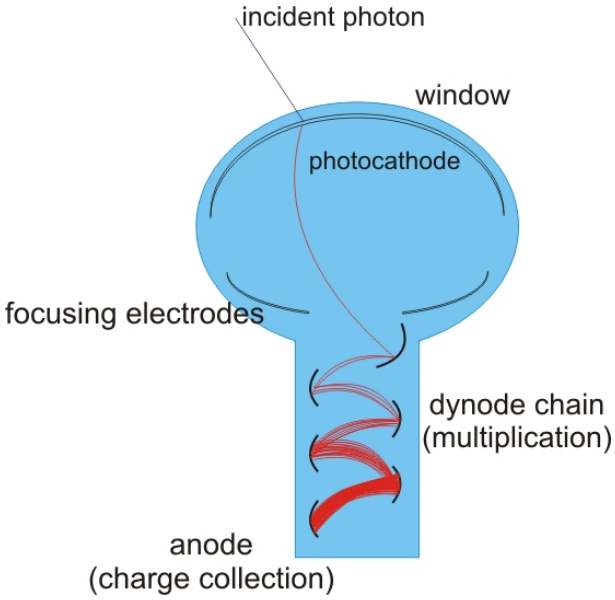

Figure 4.2: Schematic of a PMT and its working principle.

The time response of a PMT is primarily determined by the transit time required for the photoelectron emitted from the photocathode to reach the anode after being multiplied. Figure 4.3 shows the basic parameters that define a PMT time response:

- Transit time (TT): time for the photoelectrons to go from the photocathode to the anode. Typical values are from 10 to 100 ns.
- Rise time and fall time: Times for the output pulse to increase from 10 to 90% and to decrease from 90 to 10% respectively. Typical values are of a few ns.
- Transit time spread (TTS): fluctuation in transit time for photoelectron pulses.

These parameters depend on the dynode type and the supplied voltage.

In figure 4.4 we show an actual output waveform obtained from a photomultiplier tube tested at the Granada lab [22]. In general, the fall time is two or three times longer than the rise time. This means that when measuring repetitive pulses, care must be taken so that each output pulse does not overlap. The FWHM (full width at half maximum) of the output pulse will usually be about 2.5 times the rise time. For example, in the case of a single photoelectron a FWHM of 4 ns has been measured for a PMT model Hamamatsu R-5912-MOD (the one used in ArDM experiment). In dark matter and neutrino experiments the time resolution typically is of a few tens of nanoseconds. Hence, we have conservatively used 50 ns as trigger window in our Monte Carlo simulation studies.

We have studied the charge detected by the PMTs to be sure that they are working in the **linearity** region. The response of a PMT should be proportional to the incident light. However, this only happens up to certain light illumination levels. Deviations from ideal behavior are primarily caused by anode linearity characteristics, that only depend on the current value if the voltage is constant. For pulsed sources, anode linearity is mainly limited by space charge effects,

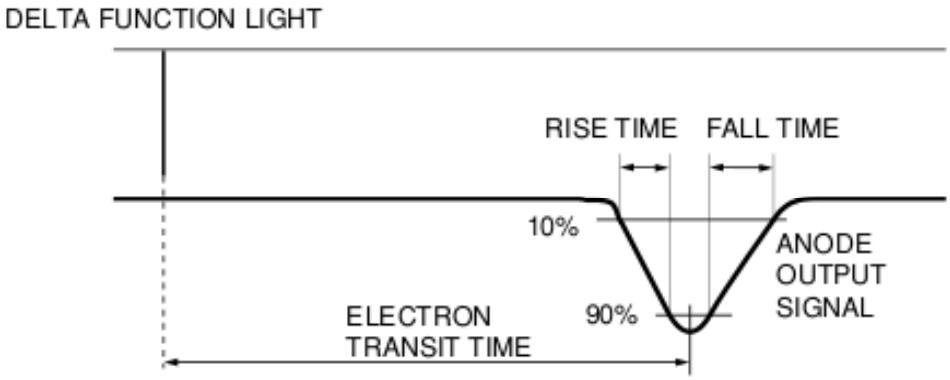

Figure 4.3: Schematic of a PMT time response.

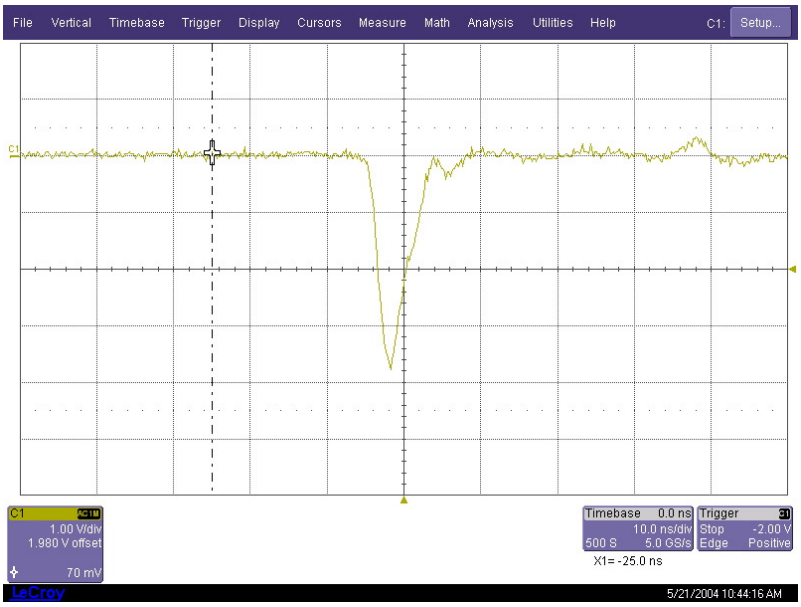

Figure 4.4: Actual shape of the PMT response as captured in the oscilloscope (2 V/division and 10 ns/division for Y and X axis respectively).

due to the magnitude of the signal current: when an intense light pulse enters a PMT a large current flows in the latter dynode stages, increasing the space charge density and causing current saturation. In general, linearity improves by increasing the supply voltage and thus the electric field between dynodes [40].

Figure 4.5 shows an example of simulated ^{39}Ar background event while figure 4.6 shows an example of a simulated WIMP-like interaction. We note that the number of detected photoelectrons by PMTs for ^{39}Ar background is higher than for WIMP-like events.

In figures 4.7 and 4.8 we show the maximum number of photoelectrons detected in a single PMT, as well as the frequency for the detected photoelectrons in a PMT placed at detector centre

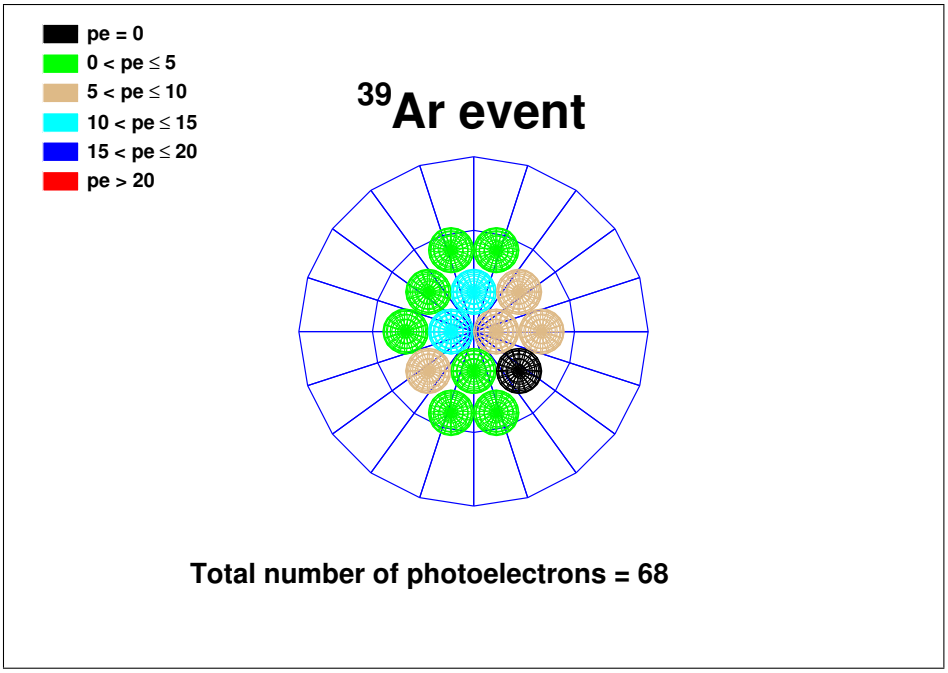

Figure 4.5: Example of ^{39}Ar background event.

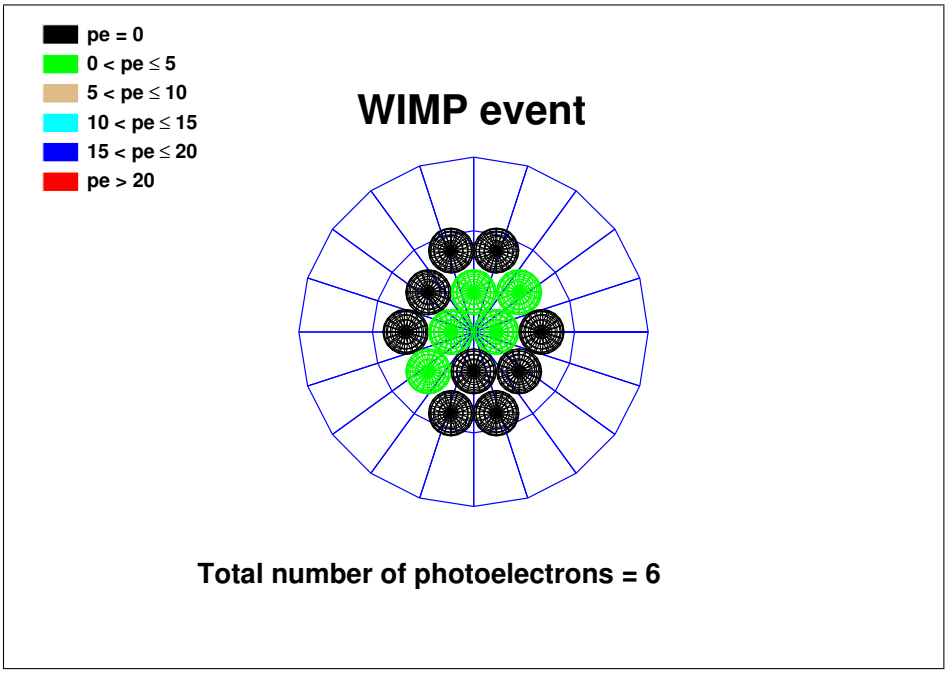

Figure 4.6: Example of WIMP-like event.

for both ^{39}Ar and WIMP interactions, respectively. The number of detected photoelectrons in a same PMT is low, so the PMTs do not saturate and safely work in the linearity region.

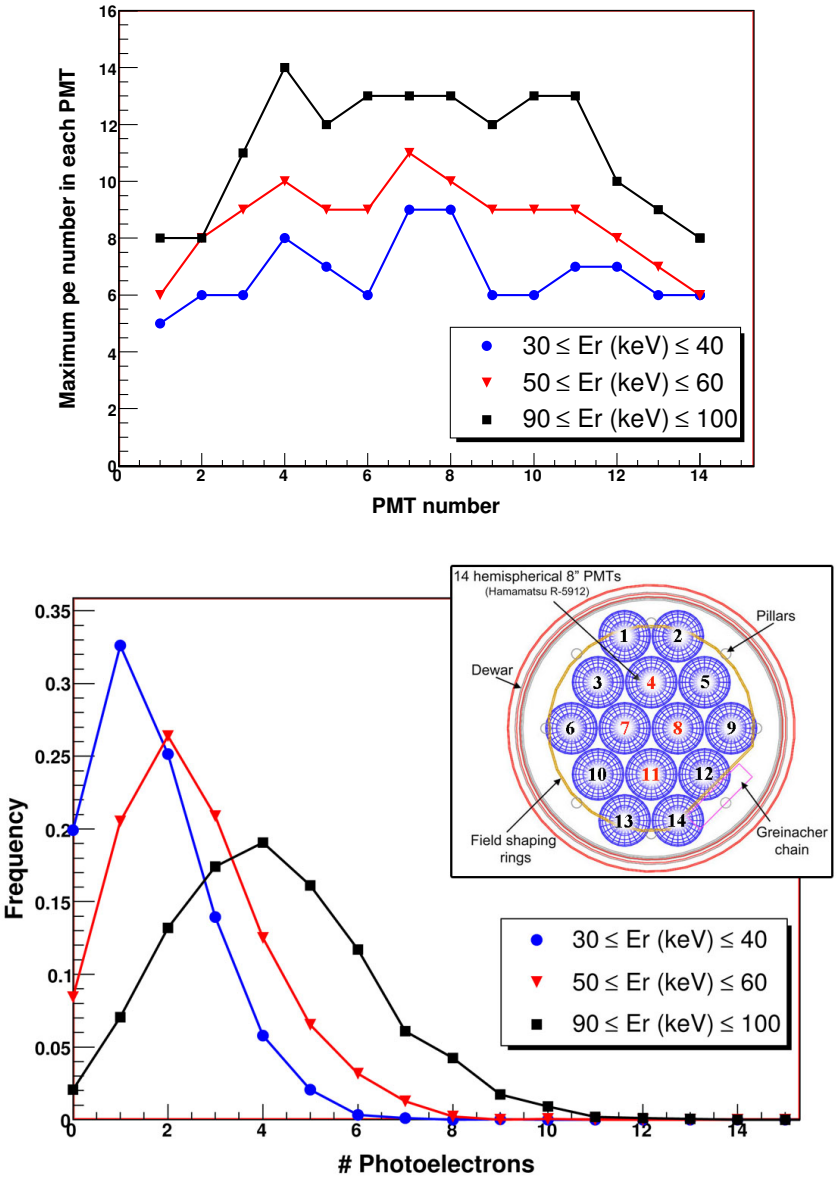

Figure 4.7: Study of PMT detected charge for ^{39}Ar background events (for three different intervals of recoil energy). Top: Maximum number of photoelectron detected in each PMT. PMTs labelled as number 4, 7, 8 and 11 are placed at detector centre. Bottom: Frequency of detected photoelectrons in a PMT placed at the detector centre (a top view of PMT positions is included).

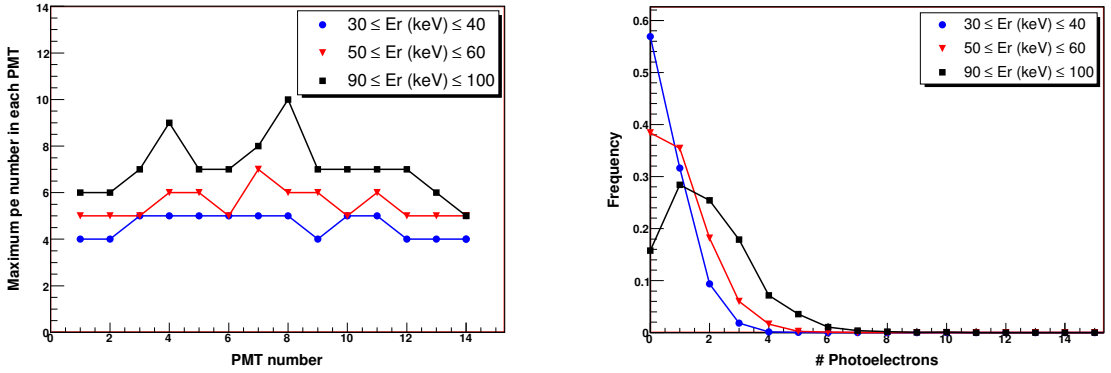

Figure 4.8: Study of PMT detected charge for WIMP-like events (for three different intervals of recoil energy). Left: Maximum number of photoelectron detected in each PMT. Right: Frequency of detected photoelectrons in a PMT placed at the detector centre. We note that detected photoelectrons are less in case of WIMP-like events than for ^{39}Ar background.

Finally, we have studied the result of applying the following trigger conditions (using a resolution time of 50 ns):

- 1 photoelectron in 2 different PMTs.
- 1 photoelectron in 3 different PMTs.
- 1 photoelectron in 4 different PMTs.
- 2 photoelectron in 2 different PMTs.
- 3 photoelectron in 2 different PMTs.
- 3 photoelectron in 1 PMT and 2 photoelectrons in 2 different PMTs.

Figure 4.9 shows the results for WIMP-like events. Good choices for our experiment are the second and third options: at least 1 photoelectron in 3 or 4 different PMTs. Their efficiencies amount on average to 89% and 77%, respectively. The choice of 1 photoelectron in 4 different PMTs has been already used as trigger condition for the measurements carried out in gaseous argon during the first technical run of ArDM detector (see chapter 2).

4.1.2 Detected charge and photoelectrons for ^{39}Ar background and WIMP events

We use our detailed GEANT4 simulation of the ArDM detector (see chapter 2) to study the ^{39}Ar background. To this end, we generate nuclear recoils of argon (WIMP-like interactions) and electron recoils (^{39}Ar decays), resulting in ionization charge and scintillation photons which are propagated inside our LAr detector. Since the behaviour of all the detector components (including our LEM and PMTs) are modelled inside the simulation, we are able to study the detected charge and photoelectrons for both types of events (WIMP-like interactions and ^{39}Ar decays). Figure 4.10 shows the recoil energy spectrum for ^{39}Ar background and WIMP events.

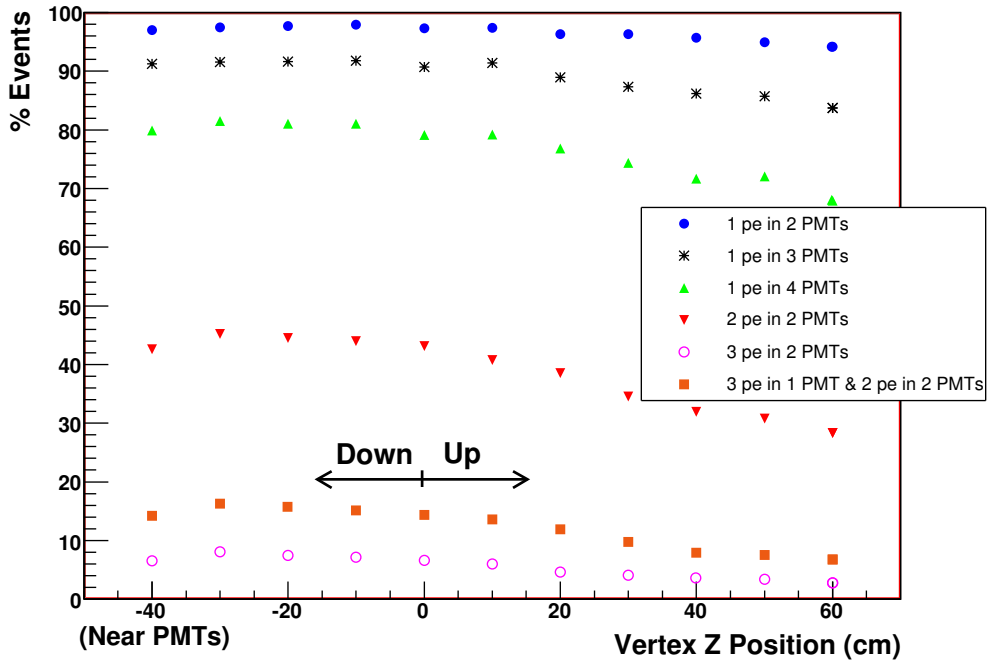

Figure 4.9: Efficiency for signal detection using different light triggers. Percentage of events causing a trigger versus event vertex position is shown.

To model the recombination process in our Monte Carlo, we assume the box model of Thomas and Imel [64, 65]. Hence, the ionization charge and scintillation photon yields for nuclear recoils are given by the following expressions:

- For ionization electrons:

$$Q(\varepsilon) = \frac{E_r}{W_0} A_I \left(\frac{E_r}{1\ keV} \right)^{\alpha_I} \frac{1}{\xi} ln(1+\xi) \tag{4.1}$$

where:
E_r = true nuclear recoil energy,
ε = electric field (= 4 kV/cm in ArDM experiment),
$\xi = \frac{C_{Ar}}{\varepsilon}$,
C_{Ar} = 1856 cm/kV,
A_I = 0.1406,
α_I = 0.228,
W_0 = 23.6 eV (minimum ionization value for fast particles).

- For scintillation photons:

$$L(\varepsilon) = \frac{E_r}{W_\gamma} A_\gamma (\frac{E_r}{1\ keV})^{\alpha_\gamma} - Q(\varepsilon) \tag{4.2}$$

where:
A_γ = 0.0663,

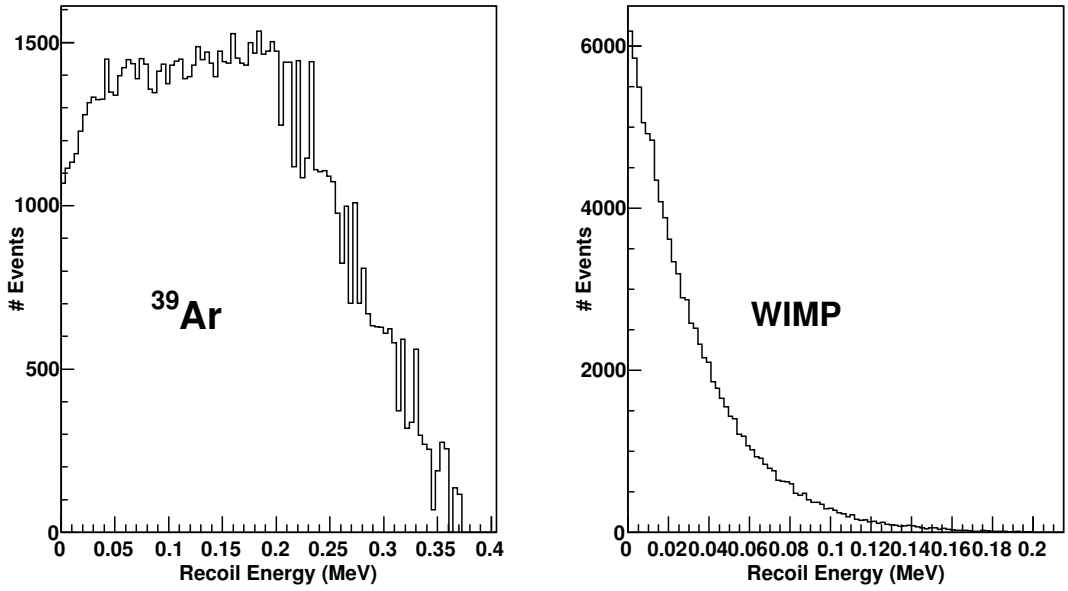

Figure 4.10: Left: Electron recoil energy spectrum (^{39}Ar). Right: Nuclear recoil energy spectrum (WIMPs).

$\alpha_\gamma = 0.228$,
$W_\gamma = 19.1$ eV.

These values have been obtained by WARP after a fit to data following the Lindhard theory [66, 59, 60]. Note that quenching for nuclear recoils has been considered.

In figure 4.11, we show the electron and photon yields for ^{39}Ar background and WIMP events. Yield bands are spread due to fluctuations in charge and light production. There are considerable differences in the range of vertical axis between ^{39}Ar and WIMP events, most of them in the case of electron yield. Both yields are much higher for ^{39}Ar background than for WIMP events.

Now, we study the **detected charge** for ^{39}Ar background and WIMP events. To this end, we have taken into account in the Monte Carlo:

- An electric drift field of 4 kV/cm.
- Electron attenuation.
- LEM gain.

Electron attenuation has been implemented in our simulation as an exponential function of the drift time over the drift electron lifetime (equation 4.3). We have assumed a drift velocity of free electrons in LAr of 0.34 cm/μs [26] and a drift electron lifetime of 1.4 ms [27].

$$\text{Electron attenuation} = e^{\left(-\frac{\text{drift time}}{\text{drift lifetime}}\right)} \tag{4.3}$$

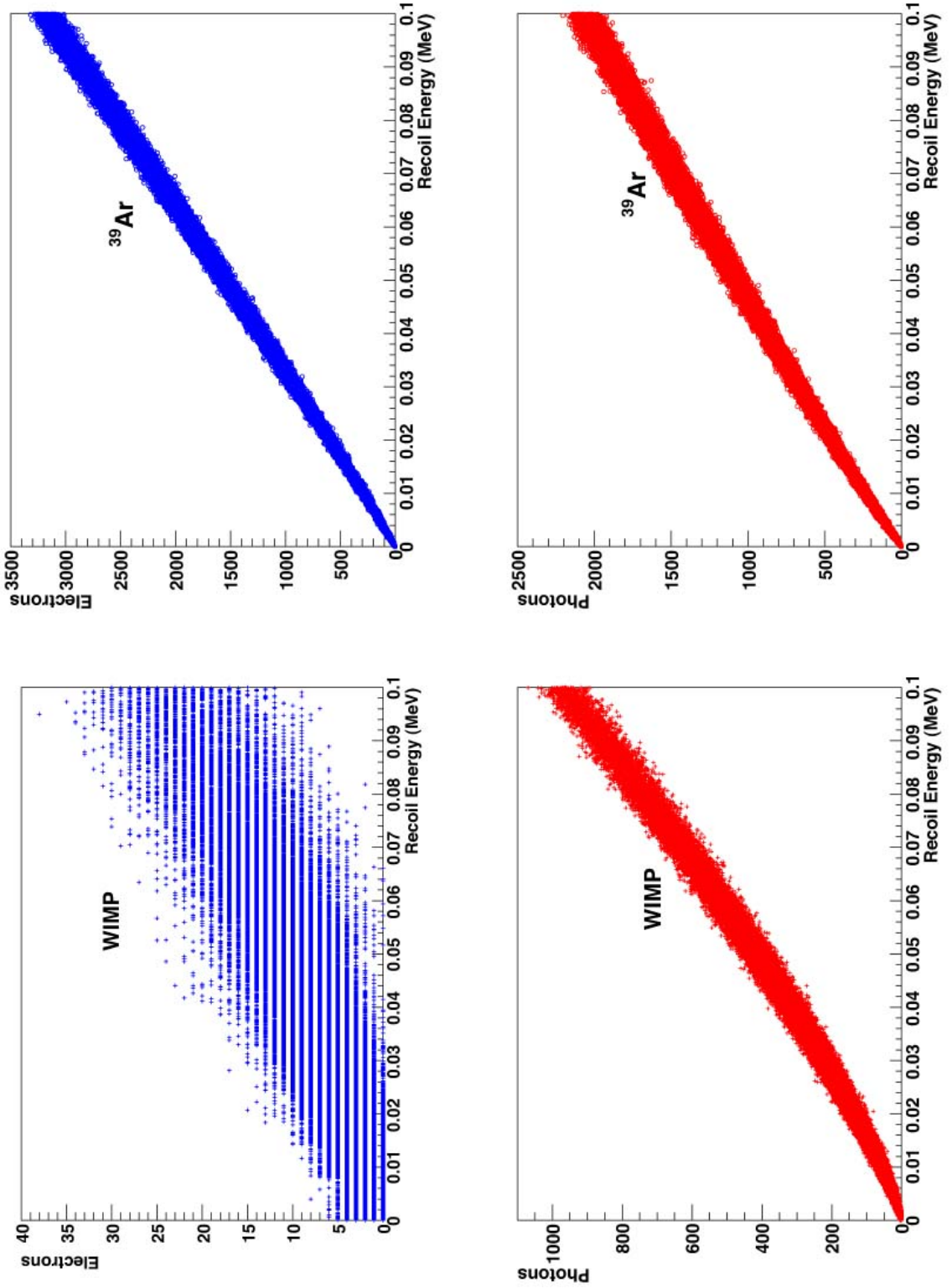

Figure 4.11: Ionization charge and scintillation photon yields for ^{39}Ar background (top) and WIMP events (bottom).

On the other hand, to simulate the LEM gain, we have used an exponential distribution with an average gain of 10^4 (see figure 4.12). Using these considerations we obtain the detected charge, which is shown in figure 4.13 for ^{39}Ar background and WIMP events.

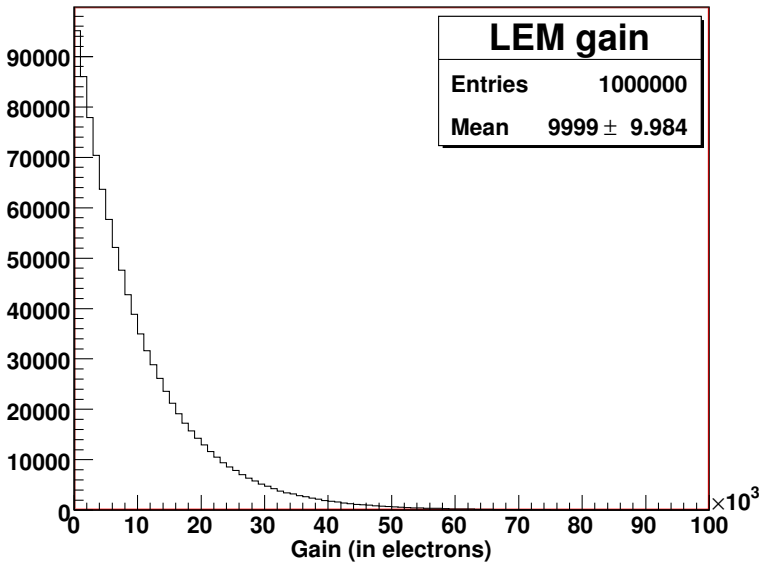

Figure 4.12: Simulated LEM gain.

As we mentioned previously, we are interested in detecting both ionization charge and scintillation photons. Therefore our attention focuses on an **efficient detection of light**. The implementation of the behaviour of our PMTs (quantum efficiency) in LAr is detailed in chapter 2. Scintillation photons from the electron and nuclear recoils are tracked along the detector using our GEANT4 simulation, so we know the number of photoelectrons detected by the PMTs. In figure 4.14 we represent the detected photoelectrons versus recoil energy for ^{39}Ar background and WIMP events. From these Monte Carlo studies, we obtain a *light yield for ^{39}Ar background of 0.7 pe/keV* (that agrees with the one predicted in chapter 2 for measurements in LAr).

4.1.3 Light/charge ratio discrimination

Once we obtain the detected charge and photoelectrons, we calculate the light/charge ratio, since the difference in light/charge ratios between ^{39}Ar background and WIMP events facilitates background rejection.

We conservatively assume that, due to instrumental limitations, we cannot detect signals below 30 keV of true recoil energy in case we use an argon target. On the other hand, we will assume a maximum recoil energy for WIMP-like events of 100 keV for the argon target.

Figure 4.15 shows the comparison of light/charge ratio versus the recoil energy for ^{39}Ar background (blue circles) and WIMP events (red crosses). Both signal bands are spread due to fluctuations in charge and light production, charge attenuation and LEM gain. There is a considerable separation between both types of events. To optimize our WIMP selection efficiency, we define an acceptance window using the following cuts:

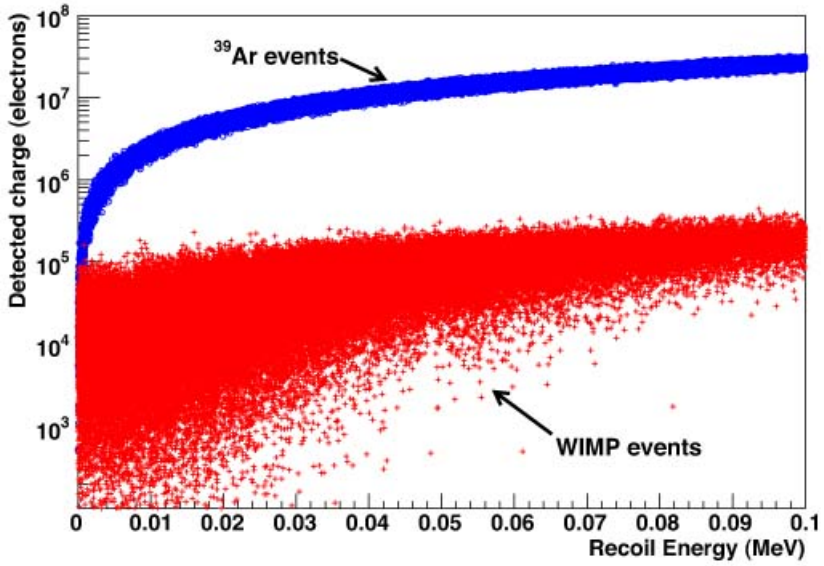

Figure 4.13: Detected charge versus recoil energy for ^{39}Ar background (blue circles) and WIMP events (red crosses).

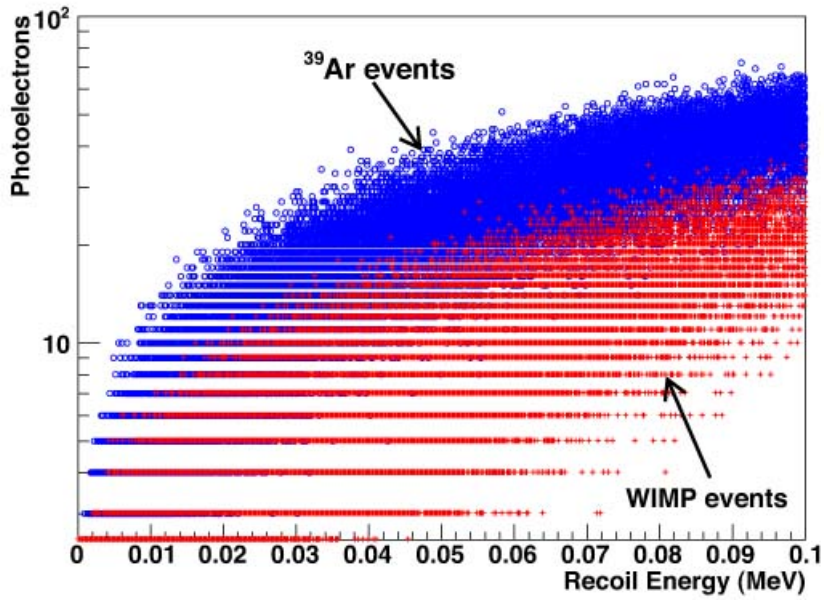

Figure 4.14: Photoelectrons versus recoil energy for ^{39}Ar background (blue circles) and WIMP events (red crosses).

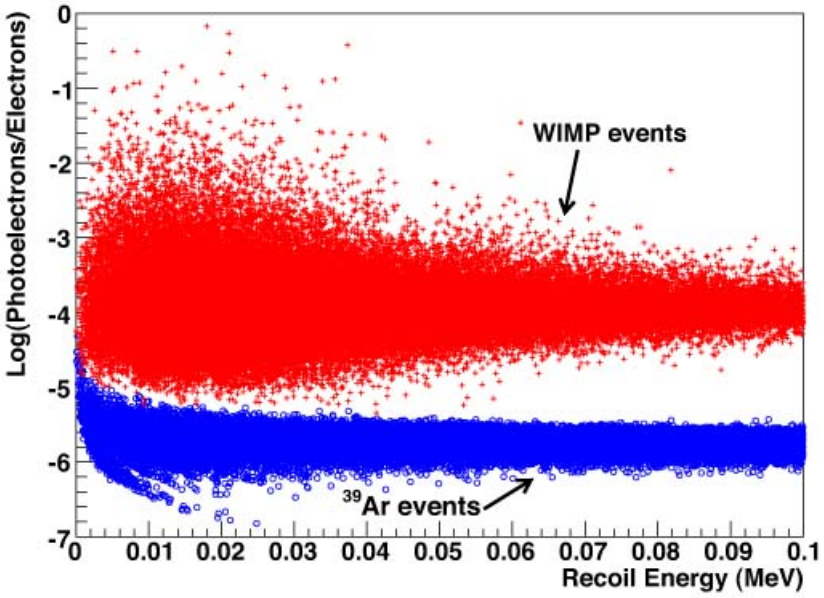

Figure 4.15: Light/charge ratio versus recoil energy in keV for ^{39}Ar background (blue circles) and WIMP events (red crosses).

- A recoil energy threshold: 30 keV $\leq$ Recoil energy
- A maximum recoil energy: 100 keV $\geq$ Recoil energy
- A cut in the light/charge ratio: $\frac{\text{light (pe)}}{\text{charge (electrons)}} \geq 10^{-4}$

Using these cuts we obtain a nuclear recoil acceptance of 53% for WIMP-like events, while for ^{39}Ar background the fraction of events within the acceptance window is negligible (this fraction of nuclear recoil acceptance is similar to those given in other experiments [67, 19]).

4.1.4 Pulse shape discrimination

In reference [22], a description of the scintillation light in LAr is given. The origin of the luminiscence is attributed to low excited molecular states, namely a singlet $^1\Sigma$ and a triplet $^3\Sigma$ states. Their decay times are widely different, respectively $\tau_s = 7.0 \pm 1.0$ ns for $^1\Sigma$ and $\tau_t = 1600 \pm 100$ ns for $^3\Sigma$ [68, 69]. Therefore, pulse shape discrimination is specially suited for further background rejection, since the separation between τ_s and τ_t can be measured.

Concerning the luminescence intensity for singlet (I_s) and triplet (I_t) states, the density of ionization strongly influences the intensity ratios I_s/I_t of the singlet and the triplet states. The results of Doke et al. [68] indicate $I_s/I_t = 0.3$ for electrons, $I_s/I_t = 1.3$ for α-particles and $I_s/I_t = 3.0$ for fission fragments, and presumably for WIMPs. Hence, the fast component is of limited size for minimum ionizing electrons and very dominant (a factor 10 larger) for heavy ionizing events. In figure 4.16 we shows the simulated ratios of fast over slow light component, that are in perfect agreement with those of Doke et al. The fraction of $I_s/(I_t + I_s)$ for scintillation light

have been implemented according to a binomial distribution whose average values are respectively 0.23 and 0.75 for electron and for nuclear recoils (these values have been confirmed by the WARP collaboration [36]).

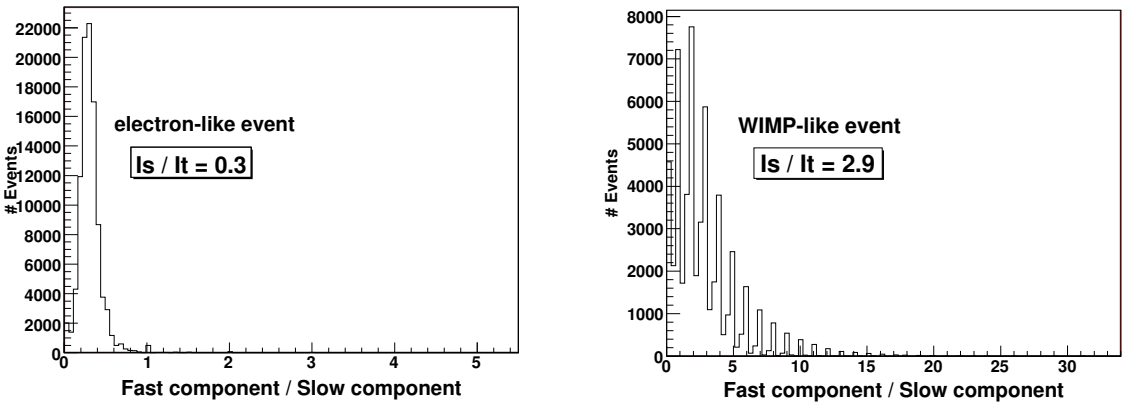

Figure 4.16: Ratio of fast over slow component of scintillation light for ^{39}Ar background (left) and WIMP-like events (right).

The difference in pulse shapes can be used to discriminate between the pulses generated by different kinds of particles species, in our case electron and WIMP-like events. A common method to do this is the so called "fast to total" algorithm, where a discrimination parameter D is derived for each single pulse, defined as the intensity in a short time window δt (for example, <400 ns) at the beginning of the pulse divided by its total intensity. Using this method, for a nuclear recoil acceptance of 53%, the rejection power against backgrounds caused by electromagnetic particles is $\sim 5 \times 10^{-7}$ for each individual target (similar to the one given in [67]).

In summary, in the ArDM experiment, we can use light/charge discrimination as well as pulse shape discrimination to reject ^{39}Ar background. These two independent approaches ought to be essentially uncorrelated. Hence, we predict a rejection power factor of about 10^{-9} between 30 and 100 keV. That is enough to ensure the rejection factor of 3.5 $\times$ 10^{-8} needed in order to suppress very efficiently the ^{39}Ar contamination.

The expected signal event rate for a recoil energy threshold of 30 keV, WIMP mass of 100 GeV and WIMP-nucleon cross-section of $\sim 10^{-43}$ cm^2 is about 10 events per day per tonne. If we take into account the cuts described in subsection 4.1.3 in the recoil energy and light/charge ratio and we choose the trigger logic offering an efficiency of 77%, we expect a rate of about 1224 WIMP events per year per tonne.

4.2 Neutron background

Neutron radiation is the most important background, because neutron events produce similar signatures inside the detector compared to WIMP events (we consider that, for our energy range of interest, events produced by neutrinos are negligible [66]). WIMPs, due to their weak coupling, do not undergo multiple interactions in the detector, then only the single scattering of a low energy neutron would be indistinguishable from expected WIMP signals.

In this section we describe the simulations developed to study the neutron background. In case of neutrons interacting via elastic scattering with argon nuclei, the imparted recoil energy on the nucleus caused by a neutron with energy E_n and a scattering angle θ is

$$E_R \simeq 2E_n \frac{M_n M_{Ar}}{(M_n + M_{Ar})^2}(1 - cos\theta). \tag{4.4}$$

We consider a fiducial region in the centre of the inner detector vessel delimited by a radius of 32 cm and a height of 100 cm, which spreads from 10 cm above the cathode (bottom) to 10 cm below the top level of LAr. This cut leaves a LAr volume of about 450 kg. Interactions occurring near the vessel walls mostly due to gamma and alpha particles are efficiently rejected by this cut.

In our neutron studies, we have taken into account a time resolution of 50 ns. Hence, all deposited energy in LAr during this time is assumed to be one interaction. If the energy deposition is above 30 keV, we consider that the interaction is *visible* (that means we can detect the interaction via our PMTs and LEM devices). We distinguish between single and multiple recoil events depending on the number of neutron interactions inside the LAr detector.

- **Single recoil event**: It has one interaction, located inside the detector fiducial region, and energy deposition in the range from 30 to 100 keV. This type of events behave like WIMP interactions and therefore are the ones contributing to the background rate. Single recoil percentage rate is defined as:

$$\text{Rate}_{\text{single}}(\%) = \frac{\text{number of single recoil events}}{\text{total number of events}} \times 100. \tag{4.5}$$

- **Multiple recoil event**: It has more than one interaction with an energy deposition above 30 keV and located in the LAr volume spanning inside the field shaping rings. Multiple recoil percentage rate is defined as:

$$\text{Rate}_{\text{multiple}}(\%) = \frac{\text{number of multiple recoil events}}{\text{number of events with at least one interaction}} \times 100. \tag{4.6}$$

The ArDM setup will be tentatively placed in the Canfranc Underground Laboratory [70], located in the Spanish Pyrenees at a depth of about 2500 meters water equivalent (m.w.e.). In such a deep underground location, the neutron sources present are:

- Neutrons produced in cosmic-ray muon interactions, called hereafter "muon-induced neutrons".
- Neutrons caused by radioactivity in surrounding rock.
- Neutrons caused by radioactivity in detector components.

The first ones are induced by the high energy through-passing muons in the rock and elements surrounding the detector, while the other induced neutrons come from local radioactivity and they are caused by U/Th traces in the rock and the detector components. They are produced in spontaneous fission of ^{238}U or via (α,n) reactions initiated by α's from decays of radioactive isotopes in U/Th chains. The decay chains of ^{238}U and ^{232}Th contain α decays with α energies of 3.5 to 11 MeV. These α undergo (α,n) reactions, thereby producing neutrons with energies in the MeV range (a very soft spectrum). However, the energy spectrum of muon-induced neutrons is harder, extending to GeV scale, so these neutrons can reach the detector from large distances. They produce higher energy recoils and can easily penetrate through the shielding.

Based on Monte Carlo simulations we have studied the contribution of each neutron source to the expected background rate. Energy spectra, flux, place of the origin and suppression methods are different for each case. Thus, neutrons from the three sources of background mentioned above have been simulated with the proper energy spectrum and fully propagated through a detailed geometry of the detector. In what follows, energy spectra and background rates, as well as the shielding performance and rejection performance of the detector are described.

4.2.1 Muon-induced neutrons

Muon-induced neutrons arise from cosmic muon interactions with surrounding rock. Shielding and detector components can also act as a target for muons, however the expected production rates are low. Highly energetic muons are able to penetrate deep underground. Neutrons are produced by spallation or photonuclear processes in the walls of the experimental hall, or by secondary interactions of muon-induced hadronic showers. In particular, fast neutrons from cosmic ray muon interactions represent an important background for dark matter searches, since they will not be efficiently moderated by a hydrocarbon shielding and can penetrate inside the detector fiducial region.

The total muon-induced neutron flux ϕ_n as a function of the depth for a site with a flat rock overburden can be estimated as [71]:

$$\phi_n = P_0 \left(\frac{P_1}{h} \right) e^{-h/P_1} \tag{4.7}$$

where h is the vertical depth in kilometers water equivalent (km.w.e.), $P_0 = 4.0 \times 10^{-7}$ cm^{-2} s^{-1} and $P_1 = 0.86$ km.w.e.

If we consider a location such as the Canfranc underground laboratory with a depth of ~ 2500 m.w.e., the total neutron flux is 7.52×10^{-9} cm^{-2} s^{-1}. The neutron energy spectrum is given by [72]:

$$\frac{dN}{dE_n} = A \left(\frac{e^{-7E_n}}{E_n} + B(E_\mu) e^{-2E_n} \right) \tag{4.8}$$

A is a normalization constant and $B(E_\mu) = 0.52 - 0.58e^{-0.0099E_\mu}$, and the muon energy spectrum can be estimated with the following equation [71]:

$$\frac{dN}{dE_\mu} = Ce^{-bh(\gamma_\mu - 1)} \cdot \left(E_\mu + \epsilon_\mu (1 - e^{-bh}) \right)^{-\gamma_\mu} \tag{4.9}$$

where C is a normalization constant, E_μ is the muon energy in GeV, $b = 0.4$/km.w.e, $\gamma_\mu = 3.77$ and $\epsilon_\mu = 693$ GeV. The previous equations give rise to the energy spectrum displayed in figure 4.17.

The angular neutron distribution can be expressed as [72]:

$$\frac{dN}{dcos\theta} = \frac{A}{(1 - cos\theta)^{0.6} + B(E_\mu)} \tag{4.10}$$

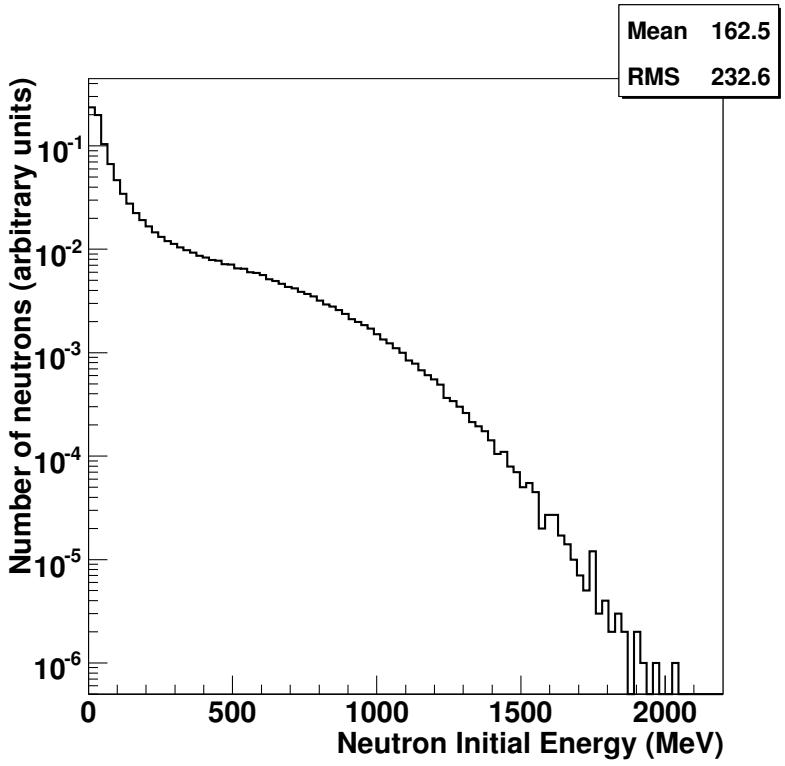

Figure 4.17: Energy spectrum of neutrons produced by muons interacting in the surrounding rock

with $B(E_\mu) = 0.699 E_\mu^{-0.136}$.

The ArDM detector dewar is covered with a hydrocarbon shield (see section 4.2.2). Hence, in order to simulate the fast neutron background, we generate them from the top surface of the shield with the specified angular and energy distributions. We have studied the background rate due to these neutrons using a simulated sample that amounts to 100 years of data taking. We have rejected multiple recoil interactions and assumed that only single recoil events contribute to the overall background rate. These events have just one interaction with energy deposition in the range from 30 to 100 keV and located inside the fiducial region. The result is a **background rate of about 2 neutrons/year arising from muon-induced neutrons** for a LAr exposure volume of 450 kg (we consider one year as 10^7 s). However, in our assumption we are conservative since we have not taken into account that very often events induced by these neutrons can be tagged using an active veto system and information about the time correlation with the passing muon.

4.2.2 Neutrons from radioactivity in surrounding rock

The minerals constituting the rock overburden in an underground laboratory contain small amounts of U and Th, causing neutron radiation. The level of the contamination strongly depends on the location and the elemental composition of the rock. The overall flux of neutrons from the surrounding rock is expected to be the most dominant, about three orders of magnitude higher than muon-induced neutron flux. As we previously mentioned, natural radioactivity can produce neutrons either directly from spontaneous fissions or by means of emitted alphas through (α, n)

reactions. Furthermore, the number of neutrons arising from these two processes is typically of the same order of magnitude. To compute the spectrum and the rate of those neutrons, the program SOURCES-4C [73] has been used. The thorium and uranium contamination has been taken as the average of those given in reference [74], namely 18.8 Bq/kg for ^{238}U and 42 Bq/kg for ^{232}Th. Secular equilibrium among them is considered. Accordingly, the computed rates for neutron production amount to 8.44×10^{-8} s^{-1}cm^{-3} from (α, n) reactions and to 7.38×10^{-8} s^{-1}cm^{-3} from spontaneous fission. Neutrons have been generated according to the energy spectrum shown in figure 4.18 and propagated through the rock using the GEANT4 simulation code and the prescriptions given in [75]. As a result we get the neutron spectrum in the walls of the laboratory. In addition, we obtain that only neutrons from the closest 2 m of rock are able to reach the tunnel. To get the final number of neutrons impinging in the detector outer walls and their energy, we have simulated a cavern of $15 \times 12 \times 40$ m^3, similar in dimensions to the experimental main hall at Canfranc underground laboratory.

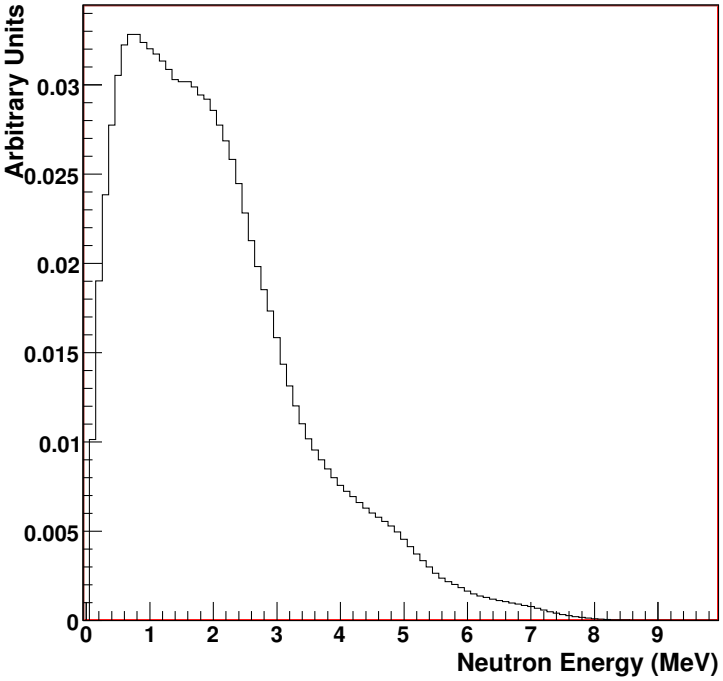

Figure 4.18: Energy spectrum of neutrons produced in the rock by natural radioactivity.

The typical material used as shield against these ambient neutrons is CH_2, so a neutron moderator of 60 cm polyethylene is placed outside the dewar to reduce effectively this background. This hydrocarbon shield absorbs the neutrons that reach the detector. Therefore, those that produce energy deposits in the same range as WIMP interactions are negligible. Actually, **the contribution to the total background rate due to neutrons caused by radioactivity in surrounding rock is <0.1 neutrons/year**.

4.2.3 Neutrons from radioactivity in detector components

One of the most important sources of background comes from neutrons produced by radioactive contamination of the material constituting the detector itself. This type of background is considered to be the most difficult to reject as it cannot be suppressed by any shielding. In the ArDM experiment, the main detector components contributing to the neutron background rate are:

- Stainless steel dewar.
- PMTs, due to their borosilicate glass window.
- Polyethylene pillars.
- LEM, made of low background material as vespel (polyimide-based polymer) or PEEK (polyetheretherketone).

As in the case of neutrons produced by radioactivity in rock, for the computation of the spectra and the number of emitted neutrons in the detector component materials, the simulation program SOURCES-4C have been used. The code was extended to α energies above 6 MeV following [75]. The resulting neutron production rates and the precise asumptions for component masses and contaminations are summarized in table 4.1 [76].

Component	Mass (kg)	ppb U	ppb Th	Background rate (neutrons/year)
Dewar (steel)	1000	0.6	0.7	380
LEM (low bg.)	4	< 2	< 2	40
PMTs (low bg.)	9.8 (14 tubes)	30	30	1400
Pillars (PE)	13 (8 pillars)	20	20	310

Table 4.1: Assumptions for detector components and estimated neutron production based on a SOURCES-4C simulation.

The biggest contribution comes from photomultiplier tubes located on the bottom of the detector, since they contain glass (glasses and minerals have a higher contamination of U/Th than metallic materials). Although main manufacturers continue to optimize the choice of materials used in PMT construction to reduce their radioactivity levels, typical contamination values for U and Th range from a few tens to several hundreds of parts per billion. Among the wide variety of tubes available in the market, in ArDM experiment we have chosen a model especially designed for low background applications: Hamamatsu R-5912-MOD (see chapter 2 for details). We have also considered to use a low background material for the LEM to minimize its neutron production rate.

The energy spectra of neutrons coming from U and Th decay chains has two contributions: one from spontaneous fission and another from (α,n) reactions. The spontaneous fission spectrum is described by $dN/dE \propto \sqrt{E}\, exp(-E/1.29)$. About 2 neutrons are emitted per spontaneous fission. The spectrum of neutrons coming from (α,n) reactions is more involved, since the (α,n) cross section is material-dependent. Therefore, there are large differences in shape of spectra and average neutron energies for the different detector materials. In these studies neutrons have been generated in a certain part of the detector: from walls, pillars, LEM or PMTs. The resulting energy spectra for stainless steel (dewar) and borosilicate glass (PMTs) are shown in figure 4.19.

We have studied the neutron background rate due to detector components using a simulated sample that amounts to more than 100 years of data taking. The results of single and multiple

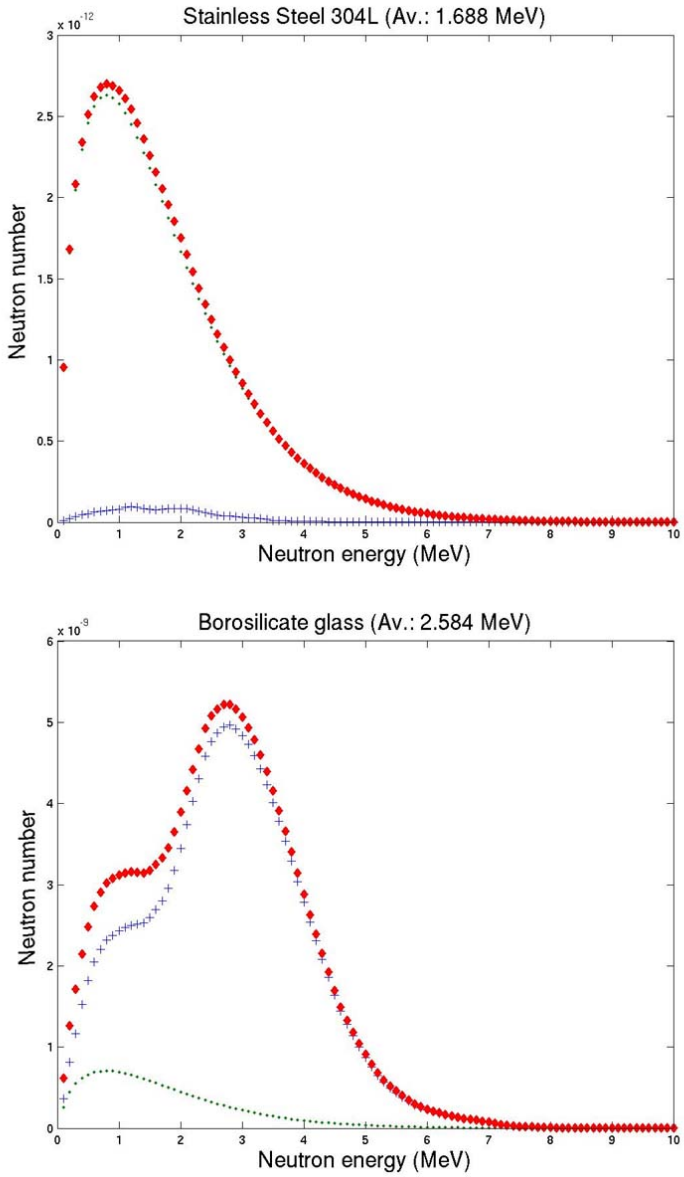

Figure 4.19: Simulated neutron energy spectra for the dewar (top) and PMTs (bottom). The dotted line is the contribution from spontaneuos fission, the crossed line is the contribution from (α,n) reactions and the circled line is the sum of the two.

recoils percentages (see section 4.2 for definitions), as well as the background rate normalized to one year of operation are shown in table 4.2. Between $20 - 35\%$ of the neutrons entering the fiducial volume can be rejected because of multiple scattering. The number of neutron scatters depends on the size of the fiducial volume, the distance of the neutron emitting components to the

fiducial volume and on the energy threshold. Assuming that a WIMP-like event is a single recoil with an energy between 30 keV and 100 keV in the detector fiducial volume, approximately less than 1% of the neutrons from detector components produce WIMP-like events. Therefore, **the overall contribution to the background rate due to neutrons coming from detector components is about 9.5 neutrons/year** for a LAr exposure volume of 450 kg.

Component	Single recoil (%)	Multiple recoil (%)	Background rate (neutrons/year)
Dewar	0.7	35	3
LEM	1.2	23	0.5
PMTs	0.2	25	3
Pillars	0.8	20	3

Table 4.2: Percentage of single and multiple neutron interactions, as well as neutron background rate from detector component normalized to one year of data taking and for a LAr exposure volume of 450 kg.

4.3 Experimental sensitivity

The physical magnitude measured by a dark matter experiment, in case no signal is observed, is a limit to the rate of dark matter interactions inside the detector, which is later transformed in a combination of masses and cross sections to produce an exclusion plot. The limit that can be set to this rate depends on the exposition time and mass, and on the expected amount of background events. Up to date, no direct [15, 16, 17, 18, 19] or indirect detection methods [77, 78] have found a signal that can be attributed to a WIMP, let alone the claim done by the DAMA/LIBRA collaboration [14]. In this section, we compute the exclusion plot the ArDM experiment will obtain in case no statistically significant WIMP signal is observed.

We have carried out a careful simulation of the potential background sources: the intrinsic ^{39}Ar background, as well as the neutron background produced by cosmic muon interactions and by radioactivity in surrounding rock and detector components. According to our simulations, we widely reach the rejection factor needed to suppress the contamination of ^{39}Ar and the total expected number of neutron-induced contamination in ArDM experiment is 11.5 events per year of data taking for a LAr exposure volume of 450 kg. Hence, it is about 26 events per year if we normalized to one tonne of LAr. This neutron background rate is obtained after a simple selection based on the nuclear recoil energy. For an exposure of one tonne $\times$ year we can reach sensitivities [79] for the WIMP-nucleon spin-independent cross section of $3.3(1.2) \times 10^{-9}$ pb for a WIMP mass of 30(100) GeV/c^2 (see figure 4.20). This represents an order of magnitude improvement with respect to current best limits, that exclude (at 90% C.L.) cross sections above $4.5(8.8) \times 10^{-8}$ pb for a WIMP mass of 30(100) GeV/c^2 [19]. To compute this limit we have assumed a standard dark matter galactic halo [13], an energy resolution that amounts to 25% for the energy range of interest and 53% nuclear recoil acceptance.

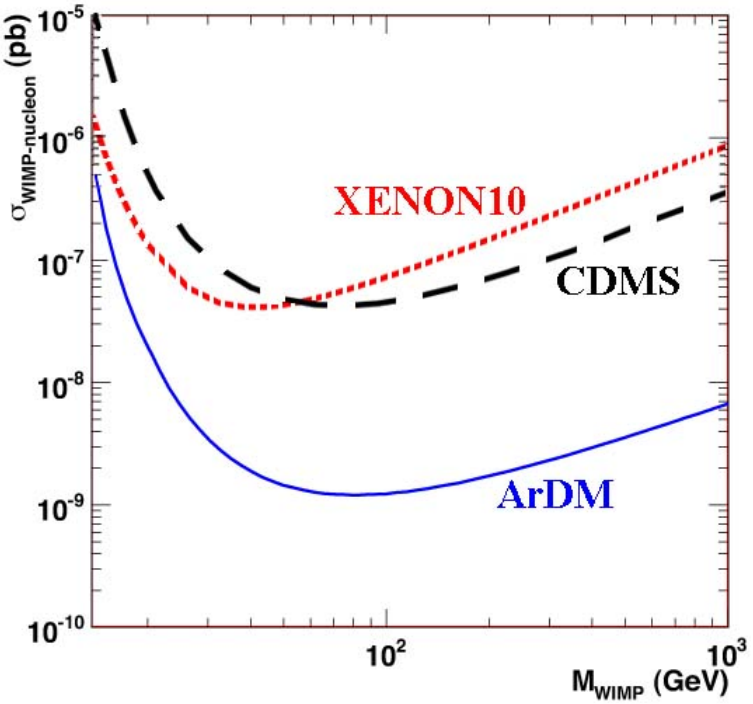

Figure 4.20: Achievable sensitivity for ArDM (solid line). The curve has been computed assuming a LAr exposure of one tonne × year and 53% nuclear recoil acceptance. The tool from reference [80] has been used. We also show current best limits from XENON10 and CDMS experiments.

Chapter 5

Physics performance of a segmented noble-liquid target immersed in a Gd-doped water veto

Nowadays, there is an intense and challenging experimental activity devoted to WIMP detection (see chapter 1). To improve current sensitivities and explore in depth the parameter space of the most favoured dark matter models, there is an indisputable need for more massive detectors with enhanced background rejection capabilities. The use of liquefied noble gasses, as target for WIMP interactions, ranks among the most promising detection techniques [81, 82, 83]. This technology is easily scalable and allows, as shown in previous chapters, to build detectors in the range of few tonnes of fiducial mass [84].

So far we have described the physics performance of one of such detectors: the ArDM experiment. In what follows, we will concentrate on evaluating the physics potential of a different experimental set-up. In this case, an effort has been made to design an experiment that allows to reduce as much as possible the background caused by neutron interactions inside the active target [2]. To enhance direct WIMP search sensitivities, we study the performance of a hybrid detection technique: cylinders filled with liquefied noble gasses, acting as targets, are immersed inside a tank of Gd-doped ultra-pure water that provides an active and efficient veto against neutrons.

5.1 The hybrid detector

Liquid noble elements, used as sensitive medium for direct dark matter searches, are a promising alternative to ionization, solid scintillation and milli-Kelvin cryogenic detectors. As previously discussed, when a WIMP particle scatters off a noble element, scintillation photons and ionization electrons are produced due to the interactions of the recoiling nucleus with the neighbouring atoms. The simultaneous detection of primary scintillation photons and ionization charge (or the secondary photons produced when this charge is extracted from the liquid to the gas phase) is a powerful discriminator against backgrounds. Pulse shape provides an additional tool to identify true signals: depending on the nature of the interacting particle, the scintillation light shows a different time dependence [68]. In addition, thanks to the high level of purity achieved, these detectors can

drift ionization charges for several meters, hence it is conceivable to reach masses of the order of several tonnes. Nowadays XENON, ZEPLIN, XMASS-DM, WARP and ArDM collaborations use liquid argon or xenon targets to look for WIMPs. Similar detectors can be used to detect the yet unobserved coherent neutrino-nucleus elastic scattering (see chapter 6).

Assuming a one tonne detector, we expect an event rate of O(1000) events per day for a WIMP-nucleus cross section of 10^{-6} pb, before cuts. For 10^{-10} pb, O(10) events per year of operation will occur. To explore such small cross sections, backgrounds should be reduced to very challenging levels (about 1 event per ton per year). In case the detector is filled with argon, the ^{39}Ar isotope, which is a beta emitter, is a serious source of concern (its activity is approximately 1 Bq per kg of natural argon [58]). However, the most important source of background is due to neutrons produced in detector components or in the rock of the underground cavern. A large fraction of these external neutrons can be rejected using external hydrocarbon shields, active vetoes or a combination of the two [85]. High-energy neutrons induced by muon interactions in the rock are a more serious concern. Recently, an innovative neutron multiplicity meter, very similar in concept to the detector discussed in this chapter, has been proposed to monitor this neutron flux [86]. The flux of internal neutrons can be highly reduced using low activity materials for the inner parts of the detector (see chapter 4). However, it is unavoidable that some of them interact with target nuclei mimicking a WIMP signal.

Detectors with a large fiducial volume (like ArDM detector, discussed on chapters 2 to 4) offer the advantage of an increased probability for neutrons to interact several times, before they exit the target. For WIMPs this is highly unlikely given the small cross sections involved. This fact can be used to further reduce neutron backgrounds. Here, we explore the opposite approach: to reduce the neutron contamination, we use targets of reduced dimensions in order to avoid as much as possible neutron capture inside the target. In what follows, we study the physics performance of a hybrid detector: it consists, on one hand, of an external active veto of ultra-pure water doped with gadolinium, in order to enhance neutron capture and its posterior identification [87]. Immersed on this veto, there are cells filled with a noble element, acting as target, and whose dimensions have been reduced in order to decrease as much as possible the chance that a neutron scatters twice or gets absorbed within it. If energy deposits occur, within a certain time window, both in the cell and water, the event is tagged as neutron-like provided the external veto records the typical 8 MeV gamma cascade from neutron capture on gadolinium.

5.1.1 Noble liquid target

We have carried out a full simulation of the detector using GEANT4 [88] (see figure 5.1). The target is made of 100 low-background metal cylinders (each 40 cm high and 30 cm in diameter). The internal volume, that can be filled with a noble liquid, has 30 cm drift distance and 24 cm in diameter. For our physics studies, the fiducial region corresponds to a cylinder of 6 cm radius and 25 cm high. The fiducial mass amounts up to 0.8 tonnes in case the target is filled with liquid xenon (LXe) and 0.4 tonnes in case liquid argon (LAr) is used. Our device can detect simultaneously the ionization charge and the scintillation light resulting from the scattering of incoming particles off xenon or argon nuclei. Light is read by means of PMTs placed at the target bottom. Ionization electrons are drifted to the liquid surface where they are converted into secondary scintillation light that is read by PMTs on top of the cylinders. Charge amplification devices (i.e., GEM, LEM, Micromegas [89, 90, 91]) are a possible alternative for charge readout.

This configuration of independent cylinders, apart from the fact of being easily scalable, offers a clear experimental advantage: data taking can proceed with two different targets simultaneously. Cylinders can be filled with argon and xenon, for example. In case a WIMP signal is observed with enough statistical relevance, we can confirm in a single experiment that the event rate and

the recoil spectral shape follow the expected dependence on A^2.

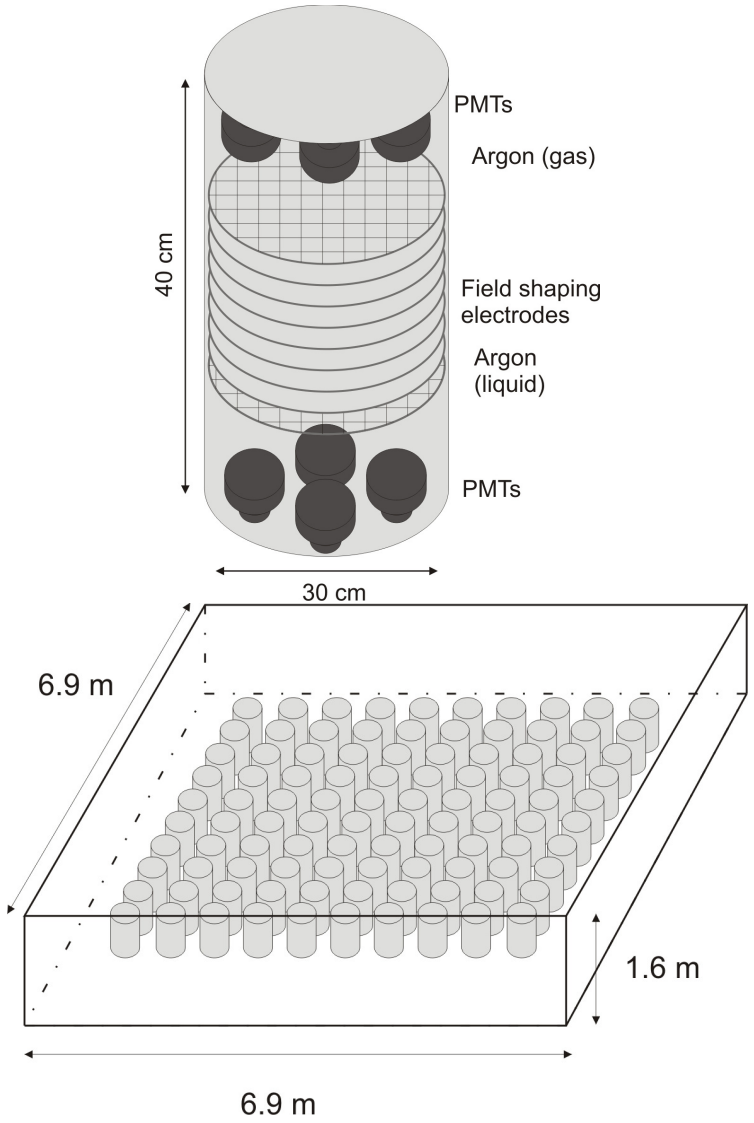

Figure 5.1: Artist's view of the detector: (Top) A target cell. It is instrumented with eight 6 cm-diameter photomultipliers. (Bottom) Noble liquid target plus active veto.

5.1.2 Active neutron shield

The active target is immersed in a water tank (1.6 m height, 6.9 m width and 6.9 m long), made of copper or other low background material. The distance between cylinders is 30 cm. The distance to the veto walls is 60 cm. This distance has been optimized to allow an efficient neutron capture by gadolinium. The veto contains 70 tonnes of ultra-pure water, once we subtract the volume taken by the sensitive targets and the ancillary system. 1500 9" PMTs (40% photo-coverage), mounted

on the water-tank walls, are used to detect the photons produced by neutron capture on Gd. They will detect the light produced by penetrating cosmic muons, as well, thus providing an efficient veto against this kind of events.

Following the approach discussed in [87], we have doped in our simulation the water-filled parallelepiped with highly-soluble gadolinium trichloride ($GdCl_3$). To avoid the absorption of photons by the cylindrical targets and the supporting system associated to them, we propose a solution similar to the one used in the Pierre Auger Observatory [92], namely to cover their external walls with Tyvek (a material that shows a reflectivity higher than 90% to Cherenkov light [93]). A particular source of concern is the radio-purity of the additive. According to the estimations given in [87] and [94], the potential background caused by it, especially the alpha particle decays of ^{152}Gd, is much smaller than what is expected from the sources considered in section 5.2. The amount of gadolinium has being chosen in order to minimize the number of neutrons captured by hydrogen nuclei, since we consider the 2.2 MeV gammas coming from this reaction are extremely hard to detect with the outer veto. A dedicated GEANT4 simulation has been carried out to study which is the optimal Gd concentration. A 1 meter radius sphere filled with Gd-doped water has been simulated and neutrons with energies up to 10 MeV have been shot from the center. Figure 5.2 shows the obtained results.

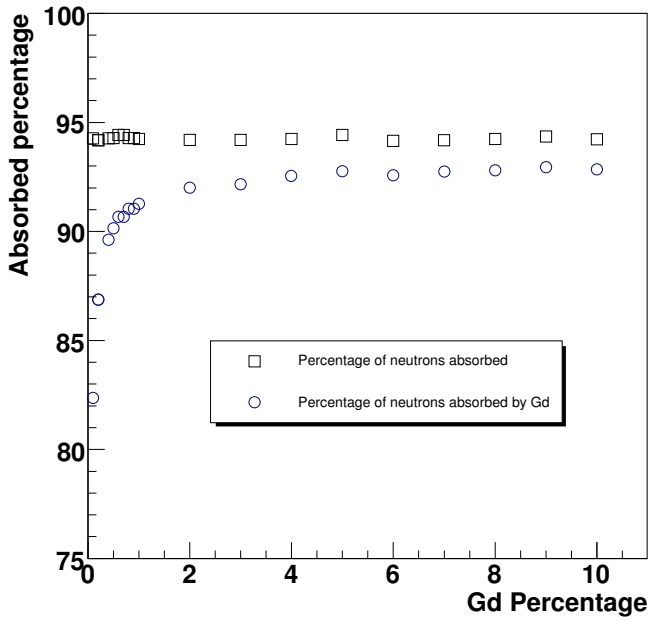

Figure 5.2: Number of absorbed particles as a function of the Gd concentration

We observe that while the total number of absorbed particles does not change with Gd concentration, the proportion of Gd-absorbed particles does, saturating at a value $\sim 2\%$. Hence, we will use for our calculations a 2% admixture by mass of $GdCl_3$.

To evaluate the veto efficiency, we track the gammas produced in the 8 MeV cascade following neutron capture by Gd. The detectable signal corresponds to Compton electrons above Cherenkov threshold. More than 90% of these electrons have energies above 3 MeV, with a mean value of about

5 MeV [94]. Nearly 50% of the Cherenkov photons are detected and only 3% of them are absorbed by the targets and their associated ancillary system. Considering a global detection efficiency of 15% for the simulated PMTs, we obtain a light yield of 6 photo-electrons/MeV. Assuming a detection threshold of 3 MeV, our trigger efficiency is >95% for this energy and reaches $\sim$ 100% at 4 MeV [95]. The overall detection efficiency for the 8 MeV gamma cascade is >90% and the energy resolution is assumed to be 20%.

5.2 Physics performance

The estimation of the overall background event rate must take into account both internal and external sources of gamma rays and neutrons. We conservatively assume that, due to instrumental limitations, we cannot detect signals below 15 (30) keV of true recoil energy in case we use a xenon (argon) target. On the other hand, we will assume a maximum true recoil energy for WIMP like events of 50 (100) keV for the xenon (argon) target. We note that it has been recently suggested that neutrinos can be a source of background for the next generation of direct-search dark matter experiments [96]. In that work, the possibility of observing neutrino nucleus coherent scattering in dark matter detectors is analyzed. They represent an irreducible source of background as they can not be shielded. For recoil energies above 1 keV, the only contribution comes from ^{8}B solar neutrinos, and the rates above 2 keV are of 15 (231) interactions per tonne $\times$ year for an xenon (argon) target. The spectrum of the produced nuclear recoils decreases with energy. Hence, as discussed in the paper, the only way to avoid this background is to set a lower limit on the energy of the events such that a negligible number of neutrino events remain. However, for the case of xenon (argon) the previous limit we imposed on the minimum energy, >10 keV (>30 keV) is already far above the one needed to render negligible the background due to the neutrino events.

5.2.1 Contamination from radioactive nuclei, xenon and argon isotopes

For a detector made of argon, an important source of background comes from the presence of radioactive ^{39}Ar, as we have already discussed in chapter 4. This is a beta emitter with an activity of about 1 Bq per kg of natural argon [58], which for a single-volume 1 tonne detector translates into a 1 kHz rate. In this case, since the target is divided into hundred independent units, the event rate due to ^{39}Ar decays does not represent an issue for the design of the data-acquisition system. In addition, the probability to have a ^{39}Ar decay overlapping with a different sort of interaction is smaller than in the case of a single-volume large-size detector due to the smaller drift times involved.

According to our simulations, the background due to radioactive nuclei can be reduced to a level well below the one expected from neutrons using the ratio of measured scintillation light over ionization and pulse shape discrimination [97, 18]. For a nuclear recoil acceptance of 50%, the rejection power against backgrounds caused by electromagnetic particles is $\sim 5 \cdot 10^{-7}$ for each individual target. This rejection power agrees with the results quoted in [18] and [67]. A further reduction of this kind of background will come from the use of underground-extracted argon. Its ^{39}Ar activity has been recently measured for the first time and shown to be <5% of the one present in natural argon [63]. These reasons lead us to not consider further this sort of background.

In case the detector is filled with xenon, ^{136}Xe is the most important radioactive isotope. It decays through double beta decay and therefore, given the small probability of the process, the resulting count rate, in the energy band of interest, is negligible compared to other sources of background, even before any rejection cut is applied.

Krypton and radon are two radioactive nuclides present in commercially available noble gasses and therefore a potential source of background as well. The highest contamination comes from ^{85}Kr, which β–decays with an endpoint energy of 678 keV. However, impurities of Kr below 1 ppb can be reached [98], making negligible the contamination produced by those radioactive decays.

5.2.2 Neutrons from detector components

One of the most important sources of background comes from neutrons produced by radioactive contamination of the materials constituting the detector itself. To minimize their rate, the use of copper for all the vessels is likely to be the best possible choice. The radioactive impurities can be reduced below 0.02 ppb in some copper samples which would bring the neutron contamination to below 1 event per year [99]. If we conservatively assume a 0.1 ppb contamination, one obtains a neutron production rate of 4.54×10^{-11} s^{-1}cm^{-3}. Being each cylinder 6 mm thick, its total volume amounts to 2217 cm^3. This means a total of one neutron per cylinder per year (we consider one year as 10^7 s).

The contamination induced by PMTs must be carefully evaluated as well. As we showed in chapter 4, typical contamination values for U and Th range from a few tens to several hundreds parts per billion. Among the wide variety of tubes available in the market, it is possible to find out some models specially designed for low background applications, where the measured uranium and thorium concentrations in quartz and metal components is of the order of ten or even less ppbs [75], giving a yearly production of less than one neutron per PMT. The phototube windows could be coated with TPB to shift the ultra-violet light to the maximum of the phototube spectral response without an increase on contamination (like in the ArDM experiment). If we assume a rate of 1 neutron per year per PMT and 8 PMTs (6 cm diameter) per cylinder, we expect a total emission of 8 neutrons per cylinder. In total, PMTs and the copper vessel contribute to 9 neutrons emitted per cylinder per year.

Although they will not be considered in the present study, there are several possibilities to reduce the rate of neutrons coming from PMTs. One is to set acrylic light-guides between photomultipliers and the active volume [75] which can reduce by a factor 2 the rate of neutrons. Another possibility is to substitute the PMTs on the top of the cylinder by charge readout devices, which can be constructed from low radioactivity materials, having a negligible neutron production rate.

We have studied the background rate due to detector components using a simulated sample that amounts to 50 years of data taking. The results shown in tables 5.1 and 5.2 are normalized to one year of operation. Table 5.1 corresponds to the configuration where LAr is used. Throughout this chapter, columns labeled as *Total* refer to the total number of neutrons per year, while columns labeled as *Not vetoed* refer to those neutrons not being absorbed in the Gd-doped water tank; likewise by E_{recoil} we mean the equivalent recoil energy inferred from the energy measured in the active target.

Neutrons	Total	Not vetoed
Produced in 1 year	900	20
30 keV $<$ E$_{recoil}$ $<$ 100 keV	19	0.3

Table 5.1: LAr target: Neutron background from detector components normalized to one year of data taking.

After a simple selection cut based on the nuclear recoil energy, we find a background of 0.3 neutrons per year for LAr detector with a fiducial mass of 0.4 tonnes. Considering as signal only

those neutrons interacting just once inside the active volume, we cant get rid of some additional background. However given the small dimensions of the targets, we expect a modest reduction factor from events with multiple interactions. It is important to note that when the active Gd-doped veto is used, the amount of background is reduced by roughly a factor fifty. The results using liquid xenon as target (fiducial mass 0.8 tonnes) are shown in table 5.2. The overall background, after the energy cut, amounts to 1 neutron per year. The reduction given by the active veto in this case is only a factor ten. The amount of background for xenon is larger than for argon. The reason comes from the fact that some xenon isotopes like ^{131}Xe and ^{129}Xe show a very high cross section for neutron absorption. For the case of a xenon-filled detector, the smaller the dimensions of the target cylinder the better to identify neutrons in the external active veto.

Neutrons	Total	Not vetoed
Produced in 1 year	900	64
15 keV $<$ E$_{recoil}$ $<$ 50 keV	12	1

Table 5.2: LXe target: Neutron background from detector components normalized to one year of data taking.

5.2.3 Neutrons and gamma rays from active veto components

Assuming the same contamination levels we used in section 5.2.2 to estimate the neutron flux due to copper walls, PMTs, voltage divider bases, etc., we obtain that the active veto system contributes with approximately 10^4 emitted neutrons per year. The flux of these neutrons is orders of magnitude smaller than the ones that reach the external walls of the detector, after being produced in the rock of the cavern by natural radioactivity (according to table 5.3 it amounts to O(10^7) rock-emitted neutrons per year). Therefore the contribution of the neutron-induced background from veto components is added to the contamination induced by the walls of the cavern and will be treated in section 5.2.4, but it represents a small fraction of the total expected background.

Another source of contamination is the gamma ray flux produced by the PMTs of the veto system. They mainly come from the decay of ^{208}Tl (thorium chain) and ^{214}Bi (uranium chain). The former produces a 2.6 MeV gamma and the latter emits 2.2 MeV and 2.4 MeV photons. As explained before, we can set a threshold of 3 MeV for the veto system without a significant loss of efficiency. In these conditions, the majority of those gamma rays will fall below threshold. Those reaching the targets can be rejected using the criteria discussed in section 5.2.1, and therefore their contribution to the total background will be significantly smaller than the one expected from neutrons.

5.2.4 Neutrons from surrounding rock

Neutrons coming from the rock have two possible origins: (1) underground production by cosmic muons (called hereafter "muon–induced neutrons") and (2) neutrons induced by spontaneous fission and (α, n) reactions due to uranium and thorium present in the rock (generically called from now on "radioactive"). As we previously mentioned in chapter 4, the latter have a very soft spectrum (typically energies of few MeV) while energy spectrum from muon–induced neutrons is harder. They may come from larger distances and produce recoils with energies well above threshold [75]. The active external water veto will efficiently tag crossing muons by Cherenkov light detection.

Neutrons	40 cm of water		60 cm of water	
	Total	Not vetoed	Total	Not vetoed
Produced in 1 year	4.2×10^7	1.6×10^7	4.2×10^7	1.6×10^7
30 keV$<E_{recoil}<$100 keV	175	3	9	< 0.1

Table 5.3: Neutron background from rock radioactivity. We assume a LAr target with a fiducial mass of 0.4 tonnes and one year of data taking. Results are shown for two different configurations of the active water veto.

Neutrons	Total	Not vetoed
Produced in 1 year	4.2×10^7	1.6×10^7
15 keV$<E_{recoil}<$50 keV	5	0.7

Table 5.4: Neutron background from rock radioactivity. A LXe target (0.8 tonnes fiducial mass) has been considered together with an active water veto 60 cm thick. Results are shown for one year of data taking

Neutron signals occurring in the noble liquid target in coincidence with water PMT signals will be rejected. A source of more serious concern are neutrons produced by muon-induced spallation reactions in the walls of the experimental hall, since they will not be efficiently moderated by the water shielding.

Neutrons from radioactivity:

In chapter 4 we described this sort of neutron background. Natural radioactivity can produce neutrons either directly from spontaneous fissions or by means of emitted alphas through (α, n) reactions. To compute the spectrum and the rate of those neutrons, the program SOURCES-4C [73] has been used (see chapter 4 for details). We remind that the computed rates for neutron production amount to 8.44×10^{-8} s^{-1}cm^{-3} from (α, n) reactions and to 7.38×10^{-8} s^{-1}cm^{-3} from spontaneous fission. Again, to get the final number of neutrons impinging in the detector outer walls and their energy, we have simulated a cavern of $15 \times 12 \times 40$ m^3, similar in dimensions to the experimental main hall at Canfranc underground laboratory, and neutrons have been propagated inside the cavern and through the detector in our GEANT simulation code. Table 5.3 shows the number of neutrons that reach the liquid argon tanks and those that produce energy deposits in the same range than WIMP interactions. Normalized to one year of data taking, we show the level of expected background for two different distances between the external vessel wall and the first active cylinder a neutron will encounter. With a 60 cm thick water active veto, the number of interactions inside the liquid argon volume is well below 1 per year.

The study has been repeated considering a liquid xenon target and 60 cm thick water veto. For this configuration, the expected background from rock radioactivity amounts to nearly one event per year (see table 5.4). In accordance with the results got while studying the contamination due to neutrons from detector components, once more the larger cross section for neutron absorption is responsible for having a bigger expected background when xenon is considered as detector target.

Neutrons	Total		Not vetoed	
Produced in 1 year	$2.4 \cdot 10^5$		$1.9 \cdot 10^5$	
No lead				
30 keV<E_{recoil}<100 keV	145		22	
Muon veto	15		2	
Lead block (bottom)				
	30 cm	60 cm	30 cm	60 cm
30 keV<E_{recoil}<100 keV	149	149	8	11
Muon veto	15	15	0.7	1
Lead block (top)				
	30 cm	60 cm	30 cm	60 cm
30 keV<E_{recoil}<100 keV	34	9	4	0.3
Muon veto	3	1	0.4	< 0.1

Table 5.5: Background events coming from cosmic muon-induced neutrons for different LAr detector configuration: a) no additional passive veto; b) an additional passive veto, located either on top or at the bottom of the detector, made of a 30 (60) cm thick lead block.We assume one year of data taking.

Muon-induced neutrons:

Fast neutrons from cosmic ray muon interactions represent an important background for dark matter searches. Unlike charged particles, they can not be tagged by veto systems, and unlike lower energy neutrons from rock radioactivity, they can not be stopped by a passive shielding. However, as proposed in [86], it is possible to place close to the detector some material in which these fast neutrons produce secondary low energy neutrons that can be detected by the proposed veto system when absorbed by Gd.

The expressions used to compute the total muon-induced neutron flux ϕ_n as a function of the depth for a site with a flat rock overburden, the neutron energy spectrum, the muon energy spectrum and the angular neutron distribution were all described in chapter 4 (see equations from 4.7 to 4.10). With these assumptions, we obtain that the total neutron flux is 7.52×10^{-9} cm^{-2} s^{-1} for the Canfranc underground laboratory (2500 m.w.e.).

In order to simulate the fast neutron background, we consider a 10×10 m^2 surface on the detector from which we simulate neutrons with the specified angular and energy distributions. Together with the detector itself, we simulate a lead block in which neutrons will create secondary particles. We have considered two different configurations (lead block on the top or at the bottom of the detector) and two different thicknesses for the passive lead veto.

According to table 5.5, out of the four configurations studied, the best one corresponds to the case where a 60 cm thick lead block is placed on top of the detector. With this passive veto alone, the background is less than one event per year, provided the lead is 60 cm thick. When combined with the Gd-doped water veto, the background drops to a negligible level. The simulations have been repeated considering liquid xenon as the target material. Results are shown in table 5.6. Again, the expected background coming from muon-induced neutrons is $\sim$1 event per year for the whole detector. However, further reduction can be achieved when water itself is considered as an active veto (as shown in tables 5.5 and 5.6, where we refer to it as Muon veto). It has been demonstrated that by rejecting events in coincidence with a muon, the contamination level decreases by a factor 10 [75]. In our case, this means the overall background would be well below

Neutrons	Total	Not vetoed
Produced in 1 year	$2.4 \cdot 10^5$	$1.9 \cdot 10^5$
15 keV$<E_{recoil}<$50 keV	8	0.7
Muon veto	0.8	< 0.1

Table 5.6: Background events coming from cosmic muon-induced neutrons using LXe as target material for a data taking period of one year. We assume that a 60 cm thick lead block is installed on top of the detector.

Background	LAr target (exposure: 1 tonne × year)	LXe target (exposure: 1 tonne × year)
Detector components	0.9	1.2
Rock radioactivity	<0.1	0.9
Muon-induced	0.1	0.1
Total	**1.0**	**2.2**

Table 5.7: Total expected backgrounds for two different target configurations. They have been normalized to an exposure of one tonne per year.

1 event per year per tonne of target material.

5.3 Discussion & Summary of the physics performance

As a result of our study, we have seen that the combination of a noble liquid (used as sensitive target) and a Gd-doped active water veto efficiently reduces neutron background. For idealized data taking conditions, if we take as reference value an exposure of one tonne × year, the total neutron-induced contamination for the case of an argon-filled detector is one event, while two events are expected for the case of xenon (see table 5.7). As shown in figure 5.3, in case no statistically significant signal is observed, we can reach sensitivities [79] for the WIMP-nucleon spin-independent cross section close to 10^{-10} pb. To compute these limits we have assumed a standard dark matter galatic halo [13], an energy resolution that amounts to 25% for the energy range of interest and 50% nuclear recoil acceptance. This represents at least two orders of magnitude improvement with respect to current best upper limit that exclude (at 90% C.L.) cross sections above $4.5(4.6) \times 10^{-8}$ pb for a WIMP mass of 30(60) GeV/c^2 [19, 100]. We also note that in the case of using LXe as target, the expected limit is about one order of magnitude better than the one expected by ArDM experiment (see chapter 4). In case we use LAr, we improve the expected ArDM limit by a factor 3.

In conclusion this experimental setup we have assessed enhances the probability for neutron capture and its identification, thus providing a much improved rejection tool against this kind of background. Among other virtues, this technique is scalable, therefore allowing the construction of large detectors with fiducial masses in the tonne range or bigger.

We have observed that the use of a Gd-doped veto reduces by about a factor fifty the neutron contamination in case the target is filled with argon and up to a factor ten in case xenon is used.

In case a positive WIMP signal is observed with sufficient statistical power, we can confirm, with a single experiment, that the event rate and the recoil spectral shape follow the expected dependence on A^2, since the independent target units can be filled with different noble liquids.

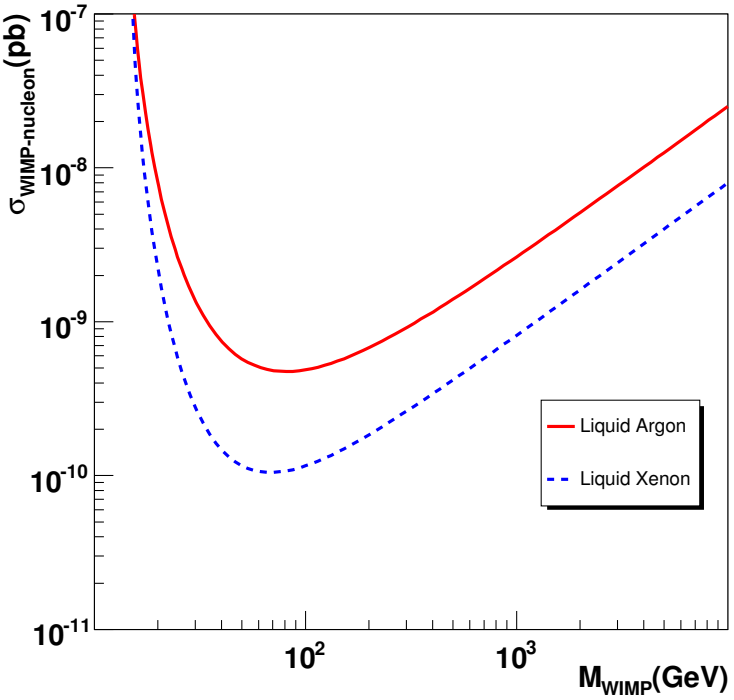

Figure 5.3: Achievable sensitivities for the case sensitive targets are filled either with LAr or LXe. The curves have been computed assuming an exposure of one tonne × year, 50% nuclear recoil acceptance. The tool from reference [80] has been used.

A simulation of the potential background sources has shown that for an exposure of one tonne × year, we expect a contamination of about one event. If no WIMP signal is observed, our calculation shows that, for idealized data taking conditions, this exposure will suffice to exclude spin-independent WIMP-nucleon cross sections in the range $10^{-9} - 10^{-10}$ pb.

Chapter 6

Possible observation of coherent neutrino-nucleus elastic scattering at a beta beam with a double phase noble gas detector

We have previously described the physics performance of two different ton-scale detectors used for direct searches of dark matter (see chapters 4 and 5). These kind of detectors, which have liquid noble gases as active target, can be used in experiments aiming to discover yet unobserved reactions in other fields such a neutrino physics.

In the last decades, neutrino physics has had a great impact on particle physics and cosmology [101]. An impressive series of experiments has allowed us to have a deeper understanding of neutrino properties, in particular about neutrino masses and oscillations [102, 103]. Despite this truly outstanding progress, there are still many open questions about the neutrino nature and its interactions. One such example is that of coherent elastic neutral-current neutrino-nucleus scattering.

In the literature, there are suggestions to look for coherent neutrino-nucleus scattering at several neutrinos sources (Sun, supernovae, reactors, stopped-pion beams, Earth interior and spallation sources) using different detection techniques [104, 105, 106, 107, 108]. In this chapter, we propose to look for this reaction at a low-energy beta beam [109, 110] using a near detector whose active target consists of a noble liquid (either xenon or argon), similar to those used in dark matter searches. This kind of detectors offer unique detection capabilities in the field of neutrino physics [24] and have demonstrated their ability to detect very low energy signals in the context of dark matter searches [98, 111, 112]. The new concept of a spherical TPC, filled with high pressure xenon, has also been proposed as a device able to detect low energy neutrinos as those coming from a galactic supernova and in particular it will be able to observe coherent neutrino-nucleus scattering [113].

In the following sections, we describe the proposed experimental setup and the expected signal rates. Likewise, we perform a careful evaluation of all potential background sources affecting this kind of search.

6.1 Coherent neutrino-nucleus elastic scattering

Coherent elastic neutral current neutrino-nucleus scattering is still an open question. This process, which is flavour-blind, has never been observed. However, the idea of having a sharp coherent forward peak for elastic neutrino-nucleus scattering was already developed in connection with the discovery of weak neutral currents [114, 115]. In the reaction under discussion, the neutrino scatters elastically from the nucleus (a composite system) and due to the superposition principle, the nucleon wave-function amplitudes (which are in phase) add coherently [116]. The condition of coherence holds for momentum transfers Q smaller than the inverse of the target size, $Q \ll (1/R)$ where R is the radius of the nucleus. The differential cross section for coherent neutrino-nucleus elastic scattering is [104]:

$$\frac{d\sigma}{d\Omega} = \frac{G_F^2}{4\pi^2}\frac{Q_w^2}{4}k^2(1+\cos\theta)F(Q^2)^2, \tag{6.1}$$

where we assume an incident neutrino of energy equal to k that scatters through an angle θ. G_F is the Fermi constant and Q_w the weak charge of a nucleus with N neutrons and Z protons:

$$Q_w = N - (1 - 4\sin^2\theta_W)Z \tag{6.2}$$

being θ_W the weak mixing angle. $F(Q^2)$ stands for the elastic form factor; it is a function of the momentum transfer squared:

$$Q^2 = 2k^2(1-\cos\theta), \tag{6.3}$$

In our calculations, the parameterization we use for $F(Q^2)$ is that of reference [117].

The condition of coherence is satisfied for neutrinos with energies of $O(10$ MeV) and therefore the cross section is directly proportional to the total number of nucleons (A) squared. In this range of energies, the elastic neutrino-nucleus cross section is larger than cross sections for elastic neutrino-electron scattering or inverse beta decay. Despite its larger cross section, the expected signals are very small and therefore very difficult to observe. Note that the maximum recoil energy ($\sim 2k^2/M$ where M is the mass of the nucleus) for a 50 MeV neutrino is few tens of KeV for a typical target (water, scintillator or noble liquids).

6.2 Experimental setup

In this section, we describe the proposed experimental setup for the storage ring for the low-energy beta beam and the noble liquid detector.

6.2.1 Low-energy beta beam

The *beta beam* concept was first introduced by Zucchelli [109], like an original method to produce neutrino beams. In contrast with the neutrino factory concept implying the production, collection and storage of muons to obtain muon and electron neutrino beams, the novel method consists in accelerating radiative ions decaying through a beta process in the straight section of a storage ring, resulting in a very intense neutrino beam. An important feature of such beta beam is that the boost factor of the accelerated ions can be varied, allowing one to explore various neutrino energy ranges. At present, the best candidates are the following ions [109]:

- ^{6}He, to produce a pure electron anti-neutrino beam.
- ^{18}Ne, to produce a pure electron neutrino beam.

The resulting neutrino beam has three novel features:

- Single neutrino flavour (electron neutrino or anti-neutrino).
- Well known energy spectrum and intensity.
- Strong collimation.

Another important advantage is that the beta beam scheme relies on existing technology [118, 119]. Therefore, we propose to use a beta beam to produce intense, collimated an pure neutrino beams of low energy. Here, low energy means a few tens of MeV, like those neutrinos involved in nucleosynthesis and in supernova explosions, up to about a hundred MeV.

Throughout our calculations, we have assumed a storage ring similar to that used in reference [120]. Its total length is L = 1885 m with two straight sections of 678 m each. The detector is located at 10 m from the ring. In steady conditions of operation, the mean number of nuclei in the ring is given by $\gamma\tau g$, where γ is the boost factor, τ is the lifetime of the parent nuclei and g is the number of injected nuclei per second. We have assumed that the stored nuclei will be accelerated at $\gamma = 7$ and $\gamma = 14$. The calculations have been performed considering an antineutrino run (coming from the decay of ^{6}He ions) and a neutrino one (where ^{18}Ne ions are stored). Following the discussion in reference [120], we have assumed that $g = 2.7 \times 10^{12}$ ions/s for ^{6}He and $g = 0.5 \times 10^{11}$ ions/s for ^{18}Ne.

6.2.2 Noble liquid detector

We have carried out a full simulation of the detector using GEANT4 [88] (see figure 6.1). The active target is a cylinder 50 cm high and 114 cm in diameter that can be filled with a noble liquid (either argon or xenon). To reduce the background contamination, rates have been computed considering a fiducial volume of 340 liters (diameter = 104 cm, height = 40 cm). The fiducial mass amounts up to 1 tonne in case the detector is filled with liquid xenon and 0.475 tonnes in case liquid argon is used. Our device can detect simultaneously the ionization charge and the scintillation light resulting from the scattering of incoming particles off xenon or argon nuclei. Light is read by means of PMTs placed at the detector bottom and at the lateral walls (as a reference we have simulated the geometry of PMTs specially designed for low background applications, see section 6.4). With this layout, we detect on average more than 50% of the scintillation photons resulting from the interactions that occur inside the fiducial volume. Ionization electrons are drifted to the liquid surface where they are read out by charge amplification devices (i.e., GEM, LEM, Micromegas [89, 90, 91]).

The active target is immersed inside a water tank, made of stainless steel, serving as an active veto shield against background. The two volumes are optically separated. The tank is a parallelepiped which spreads over 150 cm from the active volume outer surface. PMTs located at the water-tank walls are used to reject particles penetrating from outside (like neutrons) or coming out from the active target. Albeit not contemplated in our simulations, we expect similar results in case other materials are used as the main component of the external veto system.

6.3 Neutrino signal

In order to estimate the total neutrino flux, we have to take into account that, given the proximity of the detector to the neutrino source, this cannot be considered as a point source and therefore the calculation is more complex. We compute the total neutrino flux following the prescriptions given in reference [121]. The decay rate of a nucleus in the rest (cm) frame is:

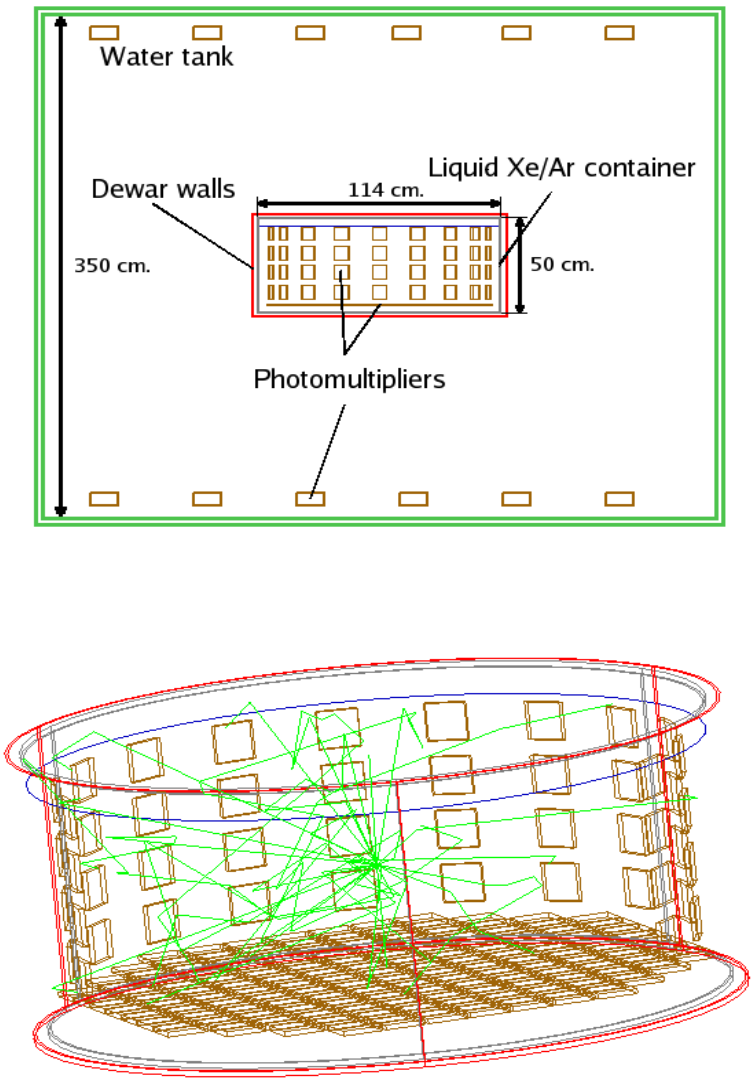

Figure 6.1: (Top) Artist's view of experimental setup (not to scale). (Bottom) GEANT4 simulation of the noble liquid container. Tracks correspond to an interaction occurring in the target. The squares represent the PMT.

$$\left.\frac{dW}{dt}\right|_{\rm cm} = \Phi_{\rm cm}(k)\, dk\, \frac{d^2\Omega}{4\pi}, \tag{6.4}$$

where k and Ω denote respectively the energy and the solid angle of the emitted neutrino, and where the neutrino flux $\Phi_{\rm cm}(k)$ is given by the formula [122]:

$$\Phi_{\rm cm}(k) = b\,k^2\,E_e\,\sqrt{E_e^2 - m_e^2}\,F(Z,E_e)\,\Theta(E_e - m_e). \tag{6.5}$$

where the constant $b = \ln 2/m_e^5 ft_{1/2}$, with m_e the electron mass and $ft_{1/2}$ the ft-value. The quantities appearing in the above expression are the energy of the emitted lepton $E_e = Q - k$, the Q-value of the reaction (Q), and the Fermi function $F(Z,E_e)$. The numerical evaluation of the Fermi function that accounts for the Coulomb modification of the spectrum and which is needed to compute the nuclei decay rate has been taken from reference [123]. The Fermi distribution function $F(Z,E_e)$ is given by the following expression:

$$F(Z,E_e) \approx F_N(Z,E_e)\left[\frac{(1+E_e^2)(1+4\zeta^2)-1}{4}\right]^S \tag{6.6}$$

where

$$S = (1-\zeta^2)^{\frac{1}{2}} - 1,$$

$$\zeta = \begin{cases} +Z\alpha = +Z/137 & \text{for } \beta^-\text{-emission} \\ -Z\alpha = -Z/137 & \text{for } \beta^+\text{-emission} \end{cases},$$

$$F_N(Z,E_e) \equiv E_e^2 \frac{2\pi y}{1-e^{-2\pi y}},$$

with $y = \zeta(1+E_e^2)^{\frac{1}{2}}/E_e$.

In the laboratory frame, where the boosted nucleus has a velocity $v = \beta c$, the decay rate reads:

$$\left.\frac{dW}{dt}\right|_{\rm lab} = \frac{1}{\gamma}\Phi_{\rm lab}(k,\theta)\,dk\,\frac{d^2\Omega}{4\pi}, \tag{6.7}$$

where $\gamma = 1/\sqrt{1-\beta^2}$ is the time dilation factor and k and $\Omega \equiv (\theta,\varphi)$ now denote the energy and solid angle of the emitted neutrino in the laboratory (lab) frame, θ being the angle of emission with respect to the beam axis. The boosted flux $\Phi_{\rm lab}(k,\theta)$ is given by:

$$\Phi_{\rm lab}(k,\theta) = \frac{\Phi_{\rm cm}(k\gamma[1-\beta\cos\theta])}{\gamma[1-\beta\cos\theta]}. \tag{6.8}$$

We consider a storage ring of total length L with straight sections of length D (see section 6.2.1 for dimensions). The total number of neutrinos emitted per unit time from a portion dl of the decay ring is:

$$\frac{dN_\nu}{dt} = \gamma\tau g \times \left.\frac{dW}{dt}\right|_{\rm lab} \times \frac{dl}{L}. \tag{6.9}$$

The expected number of neutrino interactions (N_{el}) per unit time is:

$$\frac{dN_{el}}{dt} = N_t \int_0^\infty dk\ \Phi_{\rm tot}(k)\ \sigma(k) \tag{6.10}$$

where N_t is the total number of target atoms, $\Phi_{\rm tot}(k)$ the incoming neutrino flux (see equation 6.11) and $\sigma(k)$ the total cross section (obtained integrating over the solid angle equation 6.1). The incoming neutrino flux, for a cylindrical detector of radius R and depth h, which is placed at a distance d from the storage ring (see section 6.2 for detector dimensions) is:

$$\Phi(k)_{\rm tot} = \int_0^D \frac{dl}{L} \int_0^h \frac{dz}{h} \int_0^{\bar{\theta}(l,z)} \frac{\sin\theta d\theta}{2} \; \Phi_{\rm lab}(k,\theta), \tag{6.11}$$

with

$$\tan\bar{\theta}(l,z) = \frac{R}{d+l+z}. \tag{6.12}$$

Figures 6.2 (neutrino run) and 6.3 (antineutrino run) show, for the two considered targets, the number of expected events above true recoil energy threshold ($E_{rec} = Q^2/2M$) per tonne per year (we assume 1 year = 10^7 seconds). Since the total cross section grows as A^2 (the mass number squared), at low recoil energies xenon rates are much larger than argon ones. However as the momentum transfer increases, the form factor for xenon decreases more rapidly than for argon, and thus, for higher E_{rec}, we expect larger signal rates in the argon target. Hence, the most appropriate choice for the target material crucially depends on the expected detection thresholds. We will see in the next section that it will also depend on the level of background contamination coming from radioactive isotopes.

In table 6.1, we show, for our simulated detector geometry, the expected number of signal events above a threshold of 5, 10, 15 and 20 KeV in E_{rec}. We see the dramatic increase of the rates as a function of the rising γ. For the case where $\gamma = 14$, the expected number of events for both liquid targets is in the range $10^2 - 10^3$. These rates might lead us to think that prospects to discover coherent elastic neutrino-nucleus scattering at a low-energy beta beam with a 1 tonne noble liquid detector are very promising. However before drawing any conclusions, we must carefully evaluate all possible sources of background.

Running Mode	Target	$E_{rec} > 5$ KeV	$E_{rec} > 10$ KeV	$E_{rec} > 15$ KeV	$E_{rec} > 20$ KeV
Neutrino	Xe	794 (42)	469 (13)	277 (4)	163 (1)
(^{18}Ne decays)	Ar	137 (10)	121 (7)	108 (5)	96 (4)
Antineutrino	Xe	5309 (153)	2717 (22)	1390 (2)	705 (0.1)
(^{6}He decays)	Ar	946 (55)	801 (33)	680 (20)	579 (12)

Table 6.1: Estimated number of neutrino-nucleus coherent interactions for a low-energy beta beam. Two sorts of ions are boosted at $\gamma = 14$ and $\gamma = 7$ (numbers in parenthesis). We have assumed one year of operation (10^7 seconds). Rates are given for a detector configuration where the considered fiducial volume (340 liters) is filled either with xenon (1 tonne of total mass) or argon (0.47 tonnes of total mass). E_{rec} stands for the true recoil energy.

6.4 Background estimation

Background events are computed for the detector layout described in section 6.2.2. In what follows, we cautiously assume that, due to instrumental limitations and in order to guarantee very high detection efficiencies, we cannot detect signals below 15 KeV of true recoil energy. The estimation of the overall background event rate in the fiducial volume must take into account both internal and external sources of gamma rays and neutrons. Among the external ones, we assume that beam-induced background, being mostly composed of low-energy particles, is efficiently reduced by the external water veto. Hence the most important background sources to study are:

- Contamination from radioactive nuclei and xenon or argon isotopes.

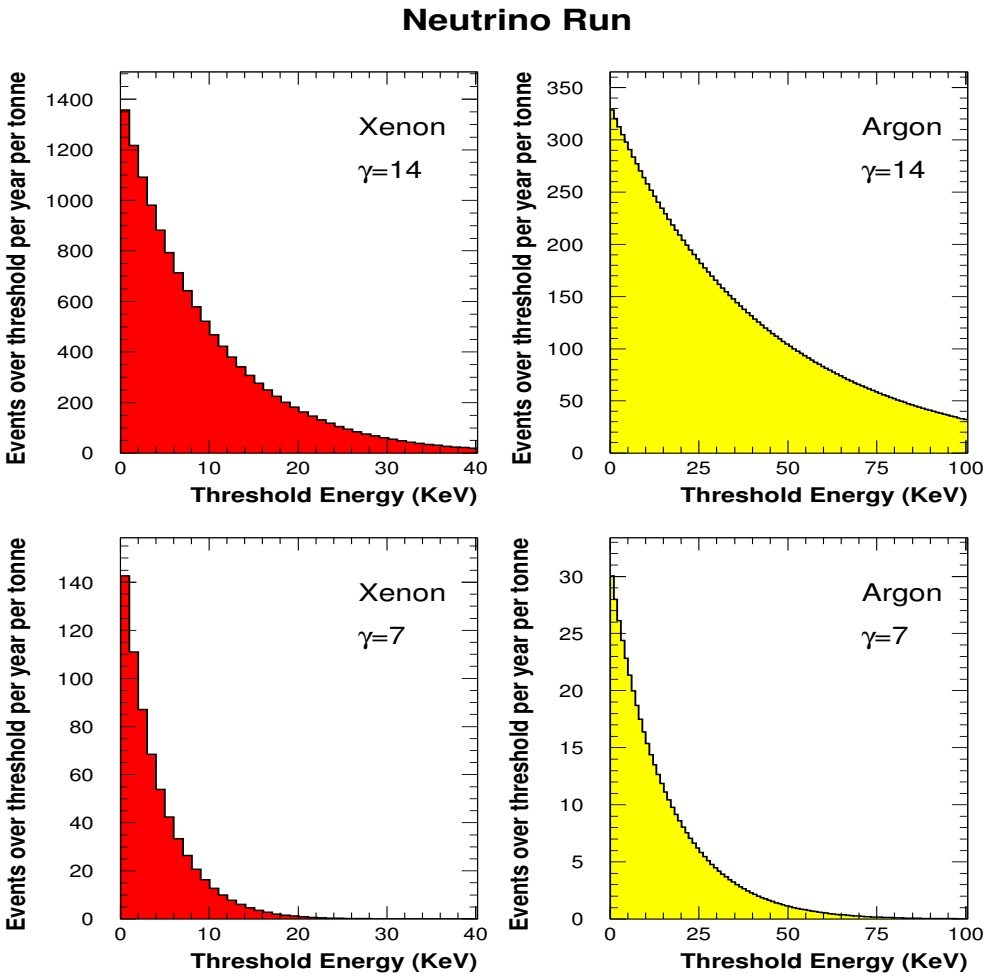

Figure 6.2: Number of coherent neutrino-nucleus interactions above true recoil energy threshold per tonne per year for two different boost factors and target materials. Neutrinos come from the decay of ^{18}Ne stored in the ring.

- Neutrons from detector components.
- Neutrons from surrounding rocks.

These background sources are described in the following sections.

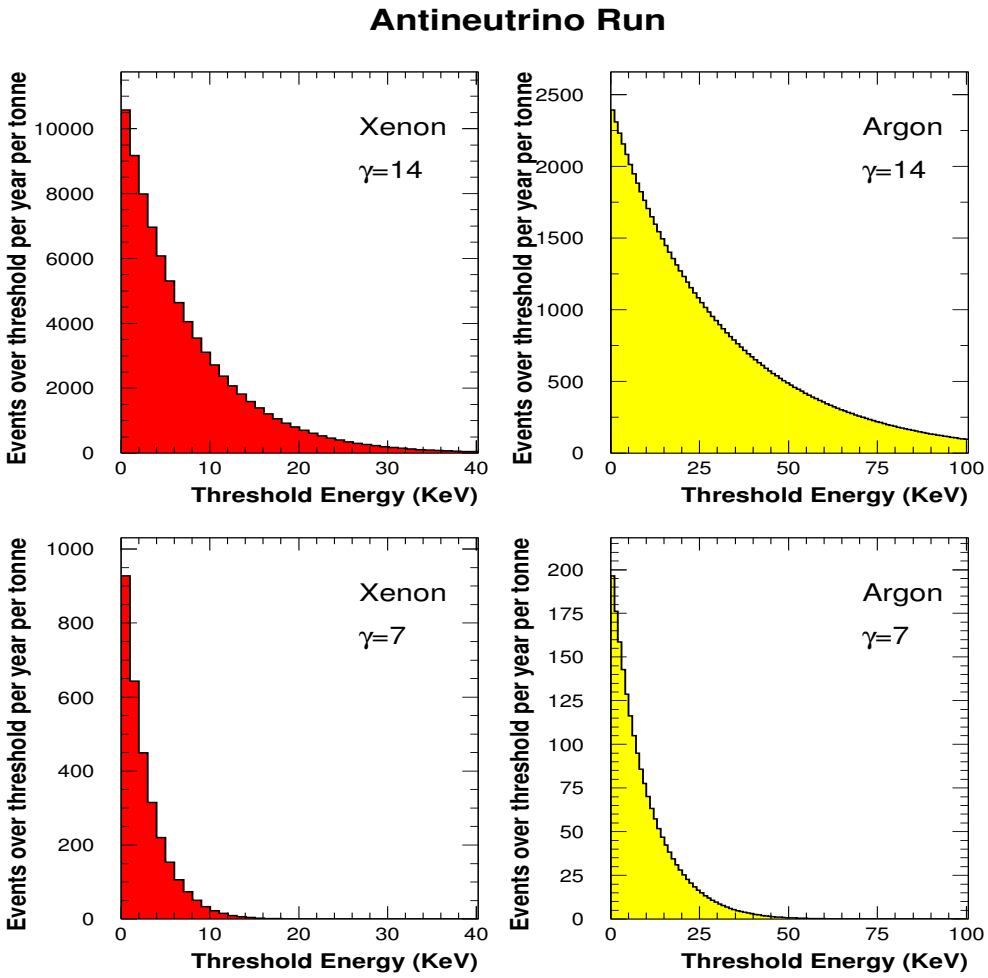

Figure 6.3: Number of coherent neutrino-nucleus interactions above true recoil energy threshold per tonne per year for two different boost factors and target materials. Antineutrinos come from the decay of ^{6}He stored in the ring.

6.4.1 Contamination from radioactive nuclei and xenon or argon isotopes

As we previously mentioned in chapters 4 and 5, for a detector made of argon, an important source of background comes from the presence of radioactive ^{39}Ar. We have shown that this background can be reduced to a tolerable level, therefore we will focus our interest in the case of a xenon target.

Among radioactive xenon isotopes, ^{136}Xe is the most important one. It decays through a double beta decay and therefore, given the small probability of the process, the resulting count rate, in

the energy band of interest, is negligible compared to other sources of background, even before any rejection cut is applied.

Krypton and radon are two radioactive nuclides present in commercially available xenon gas at the level of tens of ppb. Purities of Kr in Xe well below 1 ppb can be reached by distillation, using charcoal column separation technology as developed by the XENON collaboration [98]. These methods will also effectively remove radon contamination with gas re-circulation and cold traps. The highest contamination comes from ^{85}Kr, which β–decays with an endpoint energy of 678 KeV. With the mentioned purity level, the expected background for the assumed mass and detector rejection power is 150 events/year.

6.4.2 Neutrons from detector components

Another important source of background can come from neutrons produced by radioactive contamination of the materials constituting the detector itself, mostly from the stainless steel dewar, PMTs and charge read-out devices.

Concerning the main dewar, if we assume a total stainless steel (304L) mass of 1000 kg and a mean contamination of 0.7 ppb of Uranium and Thorium, the predicted residual rate of neutron induced recoils in the inner volume is 500 evts/year [75]. Out of them, only 10 % survive the analysis cuts (single recoils with $E_{rec} > 15$ keV).

The use of a copper vessel remains also a valid option. The radioactive impurities can be reduced below 0.02 ppb in some copper samples which would bring the neutron rate to below 1 event per year [75].

If we assume a LEM as the charge readout device, its glass part (Vetronite) is the main source of background. Made of epoxy resin (∼50 %) and alumino-boro-silicate glass fibres (∼50 %) the concentration of both, U and Th is about 1000 ppb. For a 1 kg flat LEM disk, this translates into 860 evts/year.

Finally, the background contribution from the PMTs must be evaluated. As we discussed in chapter 4, typical contamination values for U and Th range from a few tens to several hundreds parts per billion per kg. Among the wide variety of tubes available in the market, it is possible to find out some models specially designed for low background applications like the 2–inch ETL type 9266. According to reference [37], the measured Uranium and Thorium concentrations in Quartz and metal components for this model is as low as 8 ppb. The PMT windows could be coated with TPB to shift the VUV light from xenon (peak emission at 174 nm) to the maximum of the PMT spectral response without an increase in contamination. In order to cover the desired surface with this PMT model, the detector should be equipped with a total of 417 units. The total GEANT4 estimated number of single recoils in the interesting energy range amounts to 120 evts/year.

6.4.3 Neutrons from surrounding rock

We have already described this neutron background in chapters 4 and 5. Neutrons coming from the rock can have two origins:

- Neutrons produced underground by cosmic muons ("muon–induced neutrons").
- Neutrons induced by spontaneous fission of ^{238}U and via (α,n) reactions due to Uranium and Thorium present in the rock ("radioactive").

The latter have a very soft spectrum [124] (typically energies of few MeV) and according to our simulations the water veto efficiently reduces this type of background to a negligible level.

The energy spectrum from muon–induced neutrons is harder. They can come from larger distances and produce recoils with energies well above threshold [75]. The active external water veto will efficiently tag crossing muons by Cherenkov light detection. Neutron signals occurring in the fiducial volume in coincidence with water PMT signals will be rejected. More dangerous are neutrons produced by muon-induced spallation reactions in the walls of the experimental hall. We have observed that by asking a single elastic interaction inside the fiducial volume with energy deposition in excess of 15 KeV and no activity detected in the veto, only neutrons about 100 MeV constitute a background. Assuming the experiment will be located at shallow depth (50 to 100 m of standard rock), we have considered a total flux of 50 muons per m^2 per second [125]. This translates into a total muon–induced neutron background of 130 evts/year.

6.5 Discussion & Summary of the physics performance

Background source	Events/year
Xenon	150
Surrounding rock	130
Internal detector components	1030
Total	1310
Total (including beam pulsed structure)	5

Table 6.2: Xenon target: Estimated number of background events from different sources.

The total estimated number of background events amounts to 1310 per year (see table 6.2). Let's note that, in real experimental conditions, this steady-state background can be accurately predicted with data taken in periods where the ion beam is off. The final estimation of the background should include the fact that the beam has a pulsed structure (neutrinos show the time stamp of the circulating ions). Assuming that the ion bunches are 5.2 ns (^{6}He) and 4.5 ns (^{18}Ne) long and that there are twenty bunches (within 2 μs) recirculating every 23.35 μs, the duty factor of the decay ring is 4.5×10^{-3} (for ^{6}He) and 3.9×10^{-3} (for ^{18}Ne) [119]. Taking into account this additional rejection factor, the final background rate is ~ 5 evts/year for true recoil energies in excess of 15 KeV. For this energy interval, the expected number of neutrino events in the case of a xenon target is 1390 (277) for a antineutrino (neutrino) run where ions are accelerated up to $\gamma = 14$. Such a significant statistical excess would allow, not only to observe coherent neutrino-nucleus elastic scattering, but to carry out an important physics programme to constrain non-standard neutrino interactions (see [108] and references therein) or to measure intrinsic electromagnetic properties of the neutrino like its effective charge radius (NECR) [126]. The NECR produces a shift in the value of the effective weak mixing angle of approximately 5%. Assuming that the flux composition is known at 2% [127] and backgrounds can be precisely measured in beam-off conditions and therefore contribute to less than 1% to the total error, we estimate that, for an energy threshold of 15 KeV, after three or four years of data taking in the anti-neutrino mode (statistical error $\sim 1\%$) we will be able to observe the effects due to this intrinsic electromagnetic property of the neutrino.

In conclusion, we have observed that bi-phase noble gas detectors are promising devices, not only for a direct dark matter detection, but also show the unquestionable potential of acting as relevant tools to improve our knowledge about neutrino properties and their interactions.

Conclusions

In the last years, the overwhelming evidence for the existence of dark matter indicates that the Standard Model of particle physics is incomplete. However, the identity of dark matter remains a mystery. Hence, at present, there is a flourishing activity in developing new experiments aiming to detect dark matter candidates.

Direct dark matter search experiments look for an excess of signals in an underground, low background environment. As shown in this thesis, massive detectors (one tonne) using liquified noble gases as target have an enormous potential and versatility to make outstanding contributions in these kind of searches. They have the capability to detect small energy depositions ($1-100$ keV) through measuring charge and light simultaneously. This allows an enhanced signal to background discrimination. In this framework, the physics performance of the liquid argon ArDM detector has been described in detail. In addition, this kind of detector can be used in experiments aiming to discover yet unobserved reactions, such as the coherent neutrino-nucleus elastic scattering at a beta beam. The main results of this thesis can be summarized as follows:

- **The ArDM experiment**
  - **We have developed a detailed Monte Carlo simulation of the experimental setup**. This simulation is key in order to study the light collection and the background rejection power. We have discuss the experimental measurements taken in gas argon at 300 K and 88 K during a test period at CERN. This first set of measurements has allowed us to test the light collection system. It performed well. Our Monte Carlo simulation reliably reproduces the data. **We obtain a light yield of 0.27 pe/keV in cold gas argon and we predict a light yield of 0.7 pe/keV for operation in LAr**.
  - **The Slow Control system, composed of level meters, temperature and pressure sensors, has been built, successfully tested and installed inside the ArDM detector**. This system is intended to monitor the detector performance during critical periods and the data taking phase. All the sensors have been calibrated and they reach a precision good enough to fulfill our experimental requirements. In particular, we have shown that:
    - **Temperature sensors (Pt10K resistors) reach a precision better than 0.5 K**.
    - **Level meters (four plane capacitors) have a sensitivity to liquid argon level changes of about 1.0 pF/mm. Their precision is about 0.2 mm**.
  - We have carried out a careful simulation of potential background sources, namely internal ^{39}Ar contamination and neutron backgrounds.

  - ∗ According to our simulations, **we are able to reach the factor 3.5×10^{-8} needed to suppress the contamination due to ^{39}Ar**.
  - ∗ **For an exposure of one tonne × year, we can reach sensitivities for spin-independent WIMP-nucleon cross section of 3.3 (1.2) × 10^{-9} pb for a WIMP mass of 30 (100) GeV/c^2**.

- We have shown that the combination of a noble liquid modular detector and a Gd-doped active water veto efficiently reduces the neutron background. Indeed, background rates close to 1 (2) events per year per tonne can be reached in liquid argon (xenon).This means that **after one year of operation, if no WIMP signal is found, we can exclude spin-independent WIMP-nucleon cross sections in the interval $10^{-9} - 10^{-10}$ pb**.

- We have observed that a **bi-phase noble gas detector is a promising device not only for direct dark matter detection, but also show unquestionable potential to detect coherent neutrino-nucleus elastic scattering at a low-energy beta beam**.

List of Figures

List of Tables

Bibliography

[1] **The ArDM** Collaboration, Amsler, C. , Carmona, M. C. *et al.*, *Design, construction and tests of the ArDM detector*, *article in preparation*.

[2] Bueno, A., Carmona, M. C. and Melgarejo, A. J., *Direct WIMP identification: physics performance of a segmented noble liquid target immersed in a Gd-doped water veto*, *JCAP* **0808** (2008) 019.

[3] Bueno, A., Carmona, M. C., Lozano, J. and Navas, S., *Observation of coherent neutrino-nucleus elastic scattering at a beta beam*, *Phys. Rev.* **D74** (2006) 033010.

[4] Gaitskell, R. J., *Direct detection of dark matter*, *Ann. Rev. Nucl. Part. Sci.* **54** (2004) 315–359.

[5] Bertone, G. and Merritt, D., *Dark matter dynamics and indirect detection*, *Mod. Phys. Lett.* **A20** (2005) 1021.

[6] **WMAP** Collaboration, Komatsu, E. *et al.*, *Five-Year Wilkinson Microwave Anisotropy Probe WMAP Observations:Cosmological Interpretation*, *Astrophys. J. Suppl.* **180** (2009) 330–376.

[7] Clowe, D. *et al.*, *A direct empirical proof of the existence of dark matter*, *Astrophys. J.* **648** (2006) L109–L113.

[8] Bradac, M. *et al.*, *Strong and weak lensing united III: Measuring the mass distribution of the merging galaxy cluster 1E0657-56*, *Astrophys. J.* **652** (2006) 937–947.

[9] Sanders, R. H. and McGaugh, S. S., *Modified Newtonian Dynamics as an Alternative to Dark Matter*, *Ann. Rev. Astron. Astrophys.* **40** (2002) 263–317.

[10] Bertone, G., Hooper, D. and Silk, J., *Particle dark matter: Evidence, candidates and constraints*, *Phys. Rept.* **405** (2005) 279–390.

[11] **Super-Kamiokande** Collaboration, Fukuda, Y. *et al.*, *Evidence for oscillation of atmospheric neutrinos*, *Phys. Rev. Lett.* **81** (1998) 1562–1567.

[12] **Particle Data Group** Collaboration, Amsler, C. *et al.*, *Review of particle physics*, *Phys. Lett.* **B667** (2008) 1. Available on the PDG WWW pages http://pdg.lbl.gov/2008/reviews/rpp2008-rev-dark-matter.pdf.

[13] Lewin, J. D. and Smith, P. F., *Review of mathematics, numerical factors, and corrections for dark matter experiments based on elastic nuclear recoil*, *Astropart. Phys.* **6** (1996) 87–112.

[14] **DAMA** Collaboration, Bernabei, R. *et al.*, *First results from DAMA/LIBRA and the combined results with DAMA/NaI*, *Eur. Phys. J.* **C56** (2008) 333–355.

[15] **CDMS** Collaboration, Akerib, D. S. *et al.*, *First results from the cryogenic dark matter search in the Soudan Underground Lab*, *Phys. Rev. Lett.* **93** (2004) 211301.

[16] **EDELWEISS** Collaboration, Chardin, G. *et al.*, *Latest results from the EDELWEISS WIMP search*, *Nucl. Instrum. Meth.* **A520** (2004) 101–104.

[17] Ahmed, B. *et al.*, *The NAIAD experiment for WIMP searches at Boulby mine and recent results*, *Astropart. Phys.* **19** (2003) 691–702.

[18] **WARP** Collaboration, Benetti, P. *et al.*, *First results from a dark matter search with liquid argon at 87-K in the Gran Sasso underground laboratory*, *Astropart. Phys.* **28** (2008) 495–507.

[19] **XENON** Collaboration, Angle, J. *et al.*, *First Results from the XENON10 Dark Matter Experiment at the Gran Sasso National Laboratory*, *Phys. Rev. Lett.* **100** (2008) 021303.

[20] Griest, K. and Kamionkowski, M., *Supersymmetric dark matter*, *Phys. Rept.* **333** (2000) 167–182.

[21] Gaitskell, R. J., *Noble Travails: Noble Liquid Dark Matter Detectors*, *Talk given at Aspen winter school* (2006).

[22] Melgarejo, A. J., *Liquid Argon Detectors for Rare Event Searches*, *Ph.D. Thesis* (2008).

[23] McKinsey, D., *Mini-CLEAN and DEAP/CLEAN Detectors*, *Talk given at University of Minnesota* (2007).

[24] **ICARUS** Collaboration, Amerio, S. *et al.*, *Design, construction and tests of the ICARUS T600 detector*, *Nucl. Instr. Meth.* **A527** (2004) 329–410.

[25] Rubbia, C., *The Liquid-Argon Time Projection Chamber: A New Concept For Neutrino Detector*, *CERN-EP/77-08* (1977).

[26] Walkowiak, W., *Drift velocity of free electrons in liquid argon*, *Nucl. Instrum. Meth.* **A449** (2000) 288–294.

[27] **ICARUS** Collaboration, Amoruso, S. *et al.*, *Analysis of the liquid argon purity in the ICARUS T600 TPC*, *Nucl. Instrum. Meth.* **A516** (2004) 68–79.

[28] **Liquid Argon Back End Electronics** Collaboration, Bazan, A. *et al.*, *ATLAS liquid argon calorimeter back end electronics*, *JINST* **2** (2007) P06002.

[29] **The ArDM** Collaboration, Boccone, V., Carmona, M. C. *et al.*, *Development of wavelength shifter coated reflectors for the ArDM argon dark matter detector*, `physics.ins-det/0904.0246`. Accepted for publication in JINST.

[30] Rubbia, A., *ArDM: A ton-scale liquid argon experiment for direct detection of dark matter in the universe*, *J. Phys. Conf. Ser.* **39** (2006) 129–132.

[31] Hitachi, A. *et al.*, *Scintillation and ionization yield for α particles and fission fragments in liquid argon*, *Phys. Rev.* **A35** (1987) 3956–3958.

[32] Badertscher, A. *et al.*, *Construction and operation of a Double Phase LAr Large Electron Multiplier Time Projection Chamber*, `physics.ins-det/0811.3384`.

[33] **GEANT4** Collaboration, Agostinelli, S. *et al.*, *GEANT4: A simulation toolkit*, *Nucl. Instrum. Meth.* **A506** (2003) 250–303.

[34] Kubota, S., Hishida, M. and Raun, J., *Evidence for a triplet state of the self-trapped exciton states in liquid argon, krypton and xenon*, *J. Phys. C* **11** (1978) 2645.

[35] Burton, W. M. and Powell, B. A., *Fluorescence of Tetraphenyl-Butadiene in the Vacuun Ultraviolet*, *Applied Optics* **12** (1973), no. 1 87–89.

[36] **WARP** Collaboration, Brunetti, R. *et al.*, *WARP liquid Argon detector for dark matter survey*, *New Astron. Review* **49** (2005) 265–269.

[37] "Electron tubes enterprises limited, http://www.electrontubes.com; http://www.electron-tubes.co.uk/pdf/rp092colour.pdf."

[38] "Hamamatsu photonics k.k., http://www.hamamatsu.com."

[39] Brice, S. J. *et al.*, *Photomultiplier tubes in the MiniBooNE experiment*, *Nucl. Instrum. Meth.* **A562** (2006) 97–109.

[40] Bueno, A. *et al.*, *Characterization of large area photomultipliers and its application to dark matter search with noble liquid detectors*, *JINST* **3** (2008) P01006.

[41] *Photomultiplier Tubes: Basics and Application.* Hamamatsu Photonics K.K., 3rd ed., 2007.

[42] Seidel, G. M. and Lanou, R. E. and Yao, W., *Rayleigh scattering in rare gas liquids*, *Nucl. Instrum. Meth.* **A489** (2002) 189–194.

[43] Bideau-Mehu, A. *et al.*, *Measurement of refractive indices of Neon, Argon, Krypton and Xenon in the 253.7-140.4 nm wavelenght range. Dispersion relations and estimated oscillator strengths of the resonance lines*, *J. Quant. Spectrosc. Radiat. Transfer* **25** (1981) 395–402.

[44] Saito, K. *et al.*, *Absolute number of scintillation photons emitted by alpha- particles in rare gases*, *IEEE Trans. Nucl. Sci.* **49** (2002), no. 4 1674–1680.

[45] Chandrasekharan, R., Messina, M. and Rubbia, A., *Detection of noble gas scintillation light with large area avalanche photodiodes (LAAPDs)*, *Nucl. Instrum. Meth.* **A546** (2005) 426–437.

[46] Benetti, P. *et al.*, *Detection of the VUV liquid argon scintillation light by means of glass-window photomultiplier tubes*, *Nucl. Instrum. Meth.* **A505** (2003) 89–92.

[47] Koller, L. R., *Ultraviolet Radiation.* John Wiley & Sons, 1965.

[48] Grandi, L., *WARP: an argon double phase technique for Dark Matter search*, *Ph.D. Thesis* (2005).

[49] Laffranchi, M., *Test of a Liquid Argon Time Projection Chamber in a Magnetic Field*, *Ph.D. Thesis* (2005).

[50] "Ist ag innovative sensor technology, http://www.ist-ag.com."

[51] "Caburn-mdc europe, http://www.caburn.co.uk."

[52] "Metcal, http://www.metcal.com."

[53] "Measurement computing, http://www.measurementcomputing.com."

[54] "Labview, http://www.ni.com/labview."

[55] "Fluke electronics, http://www.fluke.com."

[56] "Keller ag, http://www.keller-druck.com."

[57] Loosli, H. H., *A dating method with ^{39}Ar*, *Earth and Planetary Science Letters* **63** (1983) 51–62.

[58] **WARP** Collaboration, Benetti, P. *et al.*, *Measurement of the specific activity of Ar-39 in natural argon*, *Nucl. Instrum. Meth.* **A574** (2007) 83–88.

[59] Lindhard, J. *et al.*, *Integral equations governing radiation effects*, *Mat. Fys. Medd. Dan. Vid. Selsk* **33** (1963), no. 10 1.

[60] Lindhard, J. *et al.*, *Range concepts and heavy ion ranges*, *Mat. Fys. Medd. Dan. Vid. Selsk* **33** (1963), no. 14 1.

[61] Bennetti, P. *et al.*, *The ICARUS R&D program and results*, *Nucl. Instr. Meth.* **A327** (1993) 173–177.

[62] Boulay, M. G. and Hime, A., *Technique for direct detection of weakly interacting massive particles using scintillation time discrimination in liquid argon*, *Astropart. Phys.* **25** (2006) 179–182.

[63] Galbiati, C. *et al.*, *Discovery of underground argon with low level of radioactive 39Ar and possible applications to WIMP dark matter detectors*, *J. Phys. Conf. Ser.* **120** (2008) 042015.

[64] Thomas, J. and Imel, D. A., *Recombination of electron-ion pairs in liquid argon and liquid xenon*, *Phys. Rev.* **A36** (1987) 614–616.

[65] Thomas, J., Imel, D. A. and Biller, S., *Statistics of charge collection in liquid argon and liquid xenon*, *Phys. Rev.* **A38** (1988) 5793–5800.

[66] **WARP** Collaboration, Brunetti, R. *et al. WIMP Argon Programme - Experimental Proposal* (2004). http://warp.pv.infn.it.

[67] Lippincott, W. H. *et al.*, *Scintillation time dependence and pulse shape discrimination in liquid argon*, *Phys. Rev.* **C78** (2008) 035801.

[68] Hitachi, A. *et al.*, *Effect of ionization density on the time dependence of luminescence from liquid argon and xenon*, *Phys. Rev.* **B27** (1983) 5279–5285.

[69] Nikkel, J. *et al.*, *Scintillation of liquid neon from electronic and nuclear recoils*, *Astropart. Phys.* **29** (2008) 161–166.

[70] Canfranc Underground Laboratory site, "http://ezpc00.unizar.es/lsc/index2.html."

[71] Mei, D. and Hime, A., *Muon-induced background study for underground laboratories*, *Phys. Rev.* **D73** (2006) 053004.

[72] Wang, Y. F. *et al.*, *Predicting neutron production from cosmic-ray muons*, *Phys. Rev.* **D64** (2001) 013012.

[73] Wilson, W. B. *et al.*, *SOURCES-4A, Technical Report LA-13639-MS, Los Alamos* (1999).

[74] Amare, J. *et al.*, *Neutrons from rock radioactivity in the new Canfranc underground laboratory*, *J. Phys. Conf. Ser.* **39** (2006) 151–153.

[75] Carson, M. J. *et al.*, *Neutron background in large-scale xenon detectors for dark matter searches*, *Astropart. Phys.* **21** (2004) 667–687.

[76] Kaufmann, L. and Rubbia, A., *Background studies for a ton-scale argon dark matter detector (ArDM)*, `hep-ph/0612056`.

[77] **MACRO** Collaboration, Ambrosio, M. *et al.*, *Limits on dark matter WIMPs using upward-going muons in the MACRO detector*, *Phys. Rev.* **D60** (1999) 082002.

[78] **Super-Kamiokande** Collaboration, Desai, S. *et al.*, *Search for dark matter WIMPs using upward through-going muons in Super-Kamiokande*, *Phys. Rev.* **D70** (2004) 083523.

[79] Feldman, G. J. and Cousins, R. D., *A Unified approach to the classical statistical analysis of small signals*, *Phys. Rev.* **D57** (1998) 3873–3889.

[80] "http://pisrv0.pit.physik.uni-tuebingen.de/darkmatter/limits/index.php."

[81] Belli, P. *et al.*, *Detecting dark matter using a liquid xenon scintillation detector*, *Nuovo Cim.* **A103** (1990), no. 5 767–771.

[82] Bennetti, P. *et al.*, *Detection of energy deposition down to the keV region using liquid xenon scintillation*, *Nucl. Instr. Meth.* **A327** (1993) 203–206.

[83] Davies, G. J. *et al.*, *Liquid xenon as a dark matter detector: Prospects for nuclear recoil discrimination by photon timing*, *Phys. Lett.* **B320** (1994) 395–399.

[84] Rubbia, A., *ArDM: A ton-scale liquid argon experiment for direct detection of dark matter in the universe*, *J. Phys. Conf. Ser.* **39** (2006) 129–132.

[85] Bungau, C. *et al.*, *Monte Carlo studies of combined shielding and veto techniques for neutron background reduction in underground dark matter experiments based on liquid noble gas targets*, *Astropart. Phys.* **23** (2005) 97–115.

[86] Hennings-Yeomans, R. and Akerib, D. S., *A Neutron Multiplicity Meter for Deep Underground Muon- Induced High Energy Neutron Measurements*, *Nucl. Instrum. Meth.* **A574** (2007) 89–97.

[87] Beacom, J. F. and Vagins, M. R., *GADZOOKS! Antineutrino spectroscopy with large water Cherenkov detectors*, *Phys. Rev. Lett.* **93** (2004) 171101.

[88] Allison, J. *et al.*, *Geant4 developments and applications*, *IEEE Trans. Nucl. Sci.* **53** (2006) 270.

[89] Sauli, F., *GEM: A new concept for electron amplification in gas detectors*, *Nucl. Instrum. Meth.* **A386** (1997) 531–534.

[90] Jeanneret, P. *et al.*, *Performance of a new Micromegas detector, with woven wire mesh, in CF-4*, *Nucl. Instrum. Meth.* **A500** (2003) 133–143.

[91] Giomataris, Y. *et al.*, *MICROMEGAS: A high-granularity position-sensitive gaseous detector for high particle-flux environments*, *Nucl. Instrum. Meth.* **A376** (1996) 29–35.

[92] **Pierre Auger** Collaboration, Abraham, J. *et al.*, *Properties and performance of the prototype instrument for the Pierre Auger Observatory*, *Nucl. Instrum. Meth.* **A523** (2004) 50–95.

[93] Gichaba, J. O., *Measurement of Tyvek Reflectivity for the Pierre Auger Project*, *Master's Thesis* (1998).

[94] Hargrove, C. K. *et al.*, *Use of Gd in gas counters as neutron detectors in SNO*, *Nucl. Instrum. Meth.* **A357** (1995) 157–169.

[95] **Super-Kamkiokande** Collaboration, Hosaka, J. *et al.*, *Solar neutrino measurements in Super-Kamiokande-I*, *Phys. Rev.* **D73** (2006) 112001.

[96] Monroe, J. and Fisher, P., *Neutrino Backgrounds to Dark Matter Searches*, *Phys. Rev.* **D76** (2007) 033007.

[97] **UK Dark Matter** Collaboration, Alner, G. J. *et al.*, *First limits on nuclear recoil events from the ZEPLIN I galactic dark matter detector*, *Astropart. Phys.* **23** (2005) 444–462.

[98] Aprile, E. *et al.*, *The XENON dark matter search experiment*, *New Astron. Rev.* **49** (2005) 289–295.

[99] ILIAS database on radiopurity materials, "http://radiopurity.in2p3.fr/."

[100] **CDMS** Collaboration, Ahmed, Z. *et al.*, *Search for Weakly Interacting Massive Particles with the First Five-Tower Data from the Cryogenic Dark Matter Search at the Soudan Underground Laboratory*, *Phys. Rev. Lett.* **102** (2009) 011301.

[101] Adams, J. *et al.*, *Proceedings of the XXIII International Conference on Neutrino Physics and Astrophysics (Neutrino 2008)*, *J. Phys. Conf. Ser.* **136** (2008).

[102] McDonald, A. B., *Evidence for neutrino oscillations. I: Solar and reactor neutrinos*, *Nucl. Phys.* **A751** (2005) 53–66.

[103] Nakamura, K., *Evidence for neutrino oscillations. II: Atmospheric and accelerator neutrinos*, *Nucl. Phys.* **A751** (2005) 67–86.

[104] Drukier, A. and Stodolsky, L., *Principles and Applications of a Neutral Current Detector for Neutrino Physics and Astronomy*, *Phys. Rev.* **D30** (1984) 2295.

[105] Barbeau, P. *et al.*, *Towards coherent neutrino detection using low-background micropattern gas detectors*, *IEEE Trans. Nucl. Sci.* **50** (2003) 1285–1289.

[106] Horowitz, C. J. *et al.*, *Supernova observation via neutrino nucleus elastic scattering in the CLEAN detector*, *Phys. Rev.* **D68** (2003) 023005.

[107] Hagmann, C. and Bernstein, A., *Two-phase emission detector for measuring coherent neutrino nucleus scattering*, *IEEE Trans. Nucl. Sci.* **51** (2004) 2151–2155.

[108] Scholberg, K., *Prospects for measuring coherent neutrino nucleus elastic scattering at a stopped-pion neutrino source*, *Phys. Rev.* **D73** (2006) 033005.

[109] Zucchelli, P., *A novel concept for a anti-ν_e/ν_e neutrino factory: The beta beam*, *Phys. Lett.* **B532** (2002) 166–172.

[110] Volpe, C., *Topical review on 'beta-beams'*, *J. Phys.* **G34** (2007) R1–R44.

[111] **UKDMC** Collaboration, Sumner, T., *Direct dark matter searches: DRIFT and ZEPLIN*, *PoS* **HEP2005** (2006) 003.

[112] Calligarich, E. *et al.*, *WARP: A double phase argon programme for dark matter detection*, *PoS* **HEP2005** (2006) 007.

[113] Aune, S. *et al.*, *Progress on a spherical TPC for low energy neutrino detection*, *J. Phys. Conf. Ser.* **39** (2006) 281–283.

[114] Bernabeu, J., *Neutral currents in semi-leptonic processes delta-t=0*, *Lett. Nuovo Cim.* **10** (1974), no. 8 329–332.

[115] Freedman, D. Z., *Coherent neutrino nucleus scattering as a probe of the weak neutral current*, *Phys. Rev.* **D9** (1974) 1389–1392.

[116] Freedman, D. Z., Schramm, D. N. and Tubbs, D. L., *The Weak Neutral Current and Its Effects in Stellar Collapse*, *Ann. Rev. Nucl. Part. Sci.* **27** (1977) 167–207.

[117] Engel, J., *Nuclear form-factors for the scattering of weakly interacting massive particles*, *Phys. Lett.* **B264** (1991) 114–119.

[118] Autin, B. *et al.*, *The acceleration and storage of radioactive ions for a neutrino factory*, *J. Phys.* **G29** (2003) 1785–1796.

[119] "http://beta-beam.web.cern.ch/beta-beam/."

[120] Balantekin, A. B., de Jesus, J. H. and Volpe, C., *Electroweak tests at beta-beams*, *Phys. Lett.* **B634** (2006) 180–184.

[121] Serreau, J. and Volpe, C., *Neutrino nucleus interaction rates at a low-energy beta- beam facility*, *Phys. Rev.* **C70** (2004) 055502.

[122] Krane, K. S., *Introductory Nuclear Physics*. John Wiley & Sons, 1998.

[123] Feister, I., *Numerical evaluation of the Fermi beta-distribution function*, *Phys. Rev.* **78** (1950) 375–377.

[124] Formaggio, J. A. and Martoff, C. J., *Backgrounds to sensitive experiments underground*, *Ann. Rev. Nucl. Part. Sci.* **54** (2004) 361–412.

[125] Bogdanova, L. N. *et al.*, *Cosmic muon flux at shallow depths underground*, *Phys. Atom. Nucl.* **69** (2006) 1293–1298.

[126] Papavassiliou, J., Bernabeu, J. and Passera, M., *Neutrino nuclear coherent scattering and the effective neutrino charge radius*, *PoS* **HEP2005** (2006) 192.

[127] Mezzetto, M., *Physics reach of the beta beam*, *J. Phys.* **G29** (2003) 1771–1776.